THULIUM DOPED MICROSPHERE LASER AND FIBER LASER

by

Jianfeng Wu

A Dissertation Submitted to the Faculty of the

COLLEGE OF OPTICAL SCIENCES

In Partial Fulfillment of the Requirements

For the Degree of

DOCTOR OF PHILOSOPHY

In the Graduate College

THE UNIVERSITY OF ARIZONA

2005

THE UNIVERSITY OF ARIZONA
GRADUATE COLLEGE

As members of the Dissertation Committee, we certify that we have read the dissertation prepared by Jianfeng Wu

entitled Thulium doped microsphere laser and fiber laser

and recommend that it be accepted as fulfilling the dissertation requirement for the Degree of Doctor of Philosophy

_____ Date: 11/15/2005
Nasser Peyghambarian

_____ Date: 11/15/2005
Alan Kost

_____ Date: 11/15/2005
Shibin Jiang

Final approval and acceptance of this dissertation is contingent upon the candidate's submission of the final copies of the dissertation to the Graduate College.

I hereby certify that I have read this dissertation prepared under my direction and recommend that it be accepted as fulfilling the dissertation requirement.

_____ Date: 11/15/2005
Dissertation Director: Nasser Peyghambarian

STATEMENT BY AUTHOR

This dissertation has been submitted in partial fulfillment of requirements for an advanced degree at the University of Arizona and is deposited in the University Library to be made available to borrowers under rules of the Library.

SIGNED: Jianfeng Wu

ACKNOWLEDGMENTS

The completion of this dissertation was made possible through the support and cooperation of many individuals. Thanks to my advisors, Dr. Nasser Peyghambarian, who provided the opportunity to conduct such an interesting research for this dissertation. I would also like to thank Dr. Shibin Jian for thoughtful guidance and encouragement through what seemed to be a never-ending process. Thanks also to Tao Luo, Jihong Geng, Jiafu Wang, Zidong Yao, and Jie Zong, for their support, suggestions, and criticisms. I'm grateful to Dr. Alan Kost and Seppo Honkanen for participating my defense and their thoughtful advices.

Finally, thanks to those who graciously participated in this study from the college of optical sciences, University of Arizona and NP Photonics Inc.

Most importantly, I want to thank my loving wife, Yi Wang, who has been my greatest support and constant inspiration.

Dedication

To my parents and my wife,

whose love and support bring me where I am.

TABLE OF CONTENTS

TABLE OF CONTENTS --- Continued

LIST OF FIGURES

LIST OF FIGURES --- *Continued*

LIST OF FIGURES --- *Continued*

LIST OF TABLES

ABSTRACT

In this dissertation, the spectroscopic properties of thulium doped tellurite and thulium doped germanate glass are characterized. Absorption and emission spectra, lifetime, Fourier Transform Infrared Spectroscopy (FTIR), and thermo-gravimetric analysis are utilized to characterize the thulium doped tellurite bulk glass samples. Judd-Oflet theory, Fuchtbauer-ladenburg theory, Kushida's model, Burshtein's hopping model, Miyakawa's non-resonant energy transfer model are employed in ab-initio calculation of cross relaxation energy transfer. The fundamental mechanism of cross relaxation energy transfer is examined through ab-initio calculation and self-calibrating spectroscopy.

Thulium doped tellurite glass microspheres are fabricated by spin casting technique. Single mode 2-μm laser is demonstrated from tellurite microsphere with high thulium doping concentration. General laser condition for self-terminating transition is discussed and concluded. Demonstration of 1.5-μm laser is achieved from a self-terminating transition of thulium doped in tellurite microsphere through a cooperative lasing technique.

Highly efficient 1.9 micron fiber laser is demonstrated in thulium doped germanate fiber laser. The slope efficiency of the fiber laser is 58%, which indicates a quantum efficiency of 1.79. Single frequency laser operation at 1.9 micron has been successfully accomplished. A fiber based Fabry-Perot interferometer is utilized as a scanning filter to examine the single frequency operation. 4 W laser output has been achieved from a 40 cm long Tm-doped germanate double cladding fiber laser.

CHAPTER 1 INTRODUCTION

1.1 Motivation

Optics is a science that deals with the genesis and propagation of light, the changes that it undergoes and produces, and other phenomena closely associated with it [1.1]. Since Euclid publish his work: Katoptrik, several research works have brought a new revolution to optics research, such as Newton's "Opticks", Huygens's work on wavelet, Maxwell's equations, and Planc's theory of light quanta. But the birth of Laser (**L**ight **A**mplification by **S**timulated **E**mission of **R**adiation) triggered the biggest explosion of activities in optics. It also opened several entirely new fields for scientists, such as non-linear optics, fiber optics, and opto-electronics, because of its ability to generate an intense and very narrow beam of light of a single wavelength**.** Numerous researches, patents, and businesses have been established upon the applications of Lasers. Today instead of as a branch of fundamental physics, laser researches have been involved in lots of other fields such as information technology, medicine treatment, biological study, and entertainment.

The idea of laser originates from Albert Einstein's theroy on " Stimulated emission" in which, when it encounters a photon, matter may lose energy by emitting an exaclty same phonton. As a result the amplification of light is achievable under condition of population inversion. In addition to the gain media, another essential device is optical cavity (resonantor) in which the light can circulate and get amplified. As long as the gain is larger than the losses, the power of the light in the laser cavity quickly rises.

Significant power output is thus achieved only above the so-called laser threshold that is the power where the small-signal gain is just sufficient to compensate the cavity loss.

The first laser action is demonstrated by Theodore H. Maiman in 1960 at Hughes Research Laboratories in Malibu, California [1.2]. It was a flash lamp pumped ruby rod laser lasing at 694 nm. Since then laser physics has always been driven by a genuinely scientific quest to extend existing limits such as higher power, shorter pulse, narrower linewidth and new wavelength. Over the last almost fifty years, developments in the laser field have occurred at a rapid pace. Many new lasers have been discovered, each with its own special properties and applications, and their cost, performance, and practicality have all shown dramatic improvement.

Recently a great deal of researches on 2-micron laser have been conducted in both solid-state laser and fiber laser field because of its wide applications in medicine, remote sensing, lidar, range finder, and molecular spectroscopy [1.3-6]. The strong absorption by water and the weak absorption by human tissues at 2 μm also nominate it as an ideal wavelength for biological and medical applications including laser angioplasty in the coronary arteries, ophthalmic procedures, arthroscopy, laparoscopic cholecystectomy and refractive surgeries. In addition, other features of 2 μm laser such as the lower atmospheric absorption, smaller scattering and “eye-safe” property make the wavelength desirable for material processing, ranging, low altitude wind shear and remote sensing, which includes Doppler lidar wind sensing and water vapor profiling by differential absorption lidar (DIAL). Such wavelength is also an ideal pump source for mid-infrared optical material.

1.2 Reviews in related areas

1.2.1 Rare earth material

The top one of the two rows of elements below periodical table makes up a group called rare earth elements. The term “rare earths” was suggested by Johann Gadolin in 1794: "rare" because when the first of the rare earth elements were discovered they were thought to be present in the earth's crust only in small amounts, and "earths" because as oxides they have an earthy appearance. The discovery of the rare earth elements provide a long history of almost two hundred years of trial and error in the claims of element discovery due to the fact that the similarity in the chemical properties of the rare earth elements make them especially difficult to be chemically isolated.

The first application of rare earths was invented in the late 19th century. That was the Welsbach gas mantle: fabric impregnated with rare-earth salts, which when heated by a gas flame, gave off an intense white light. Nowadays, rare earths play more and more important roles in the field of optics, such as trichromatic fluorescent lamps, solid-state lasers, magnetic device, fiber amplifier and lasers.

Trivalent rare earths, which have been mostly used as activators, have special electronic configurations ($[\mathrm{Xe}]4f^{N-1}5S^2 5p^6 6s^0$) that distinguish them from other optically active ions such as transition metals. Its N-1inner electrons of $4f$ shell are shielded from the external electro-magnetic field by the outmost shell 5s and 5d. Since the optically active electrons in rare earths are well shielded from the local Coulombic environment, the energy levels remain fairly constant when comparing the levels in

different hosts. Professor Dieke's research group at Johns Hopkins (1960's) compiled a table of energy levels for the trivalent rare earths in crystals. (See Fig. 1.1) The shield effect also makes the $4f$ -> $4f$ transitions of rare earths possess sharp lines, strong absorption band, and less sensibility to host. Such features make rare earths the most desirable candidates as laser material.

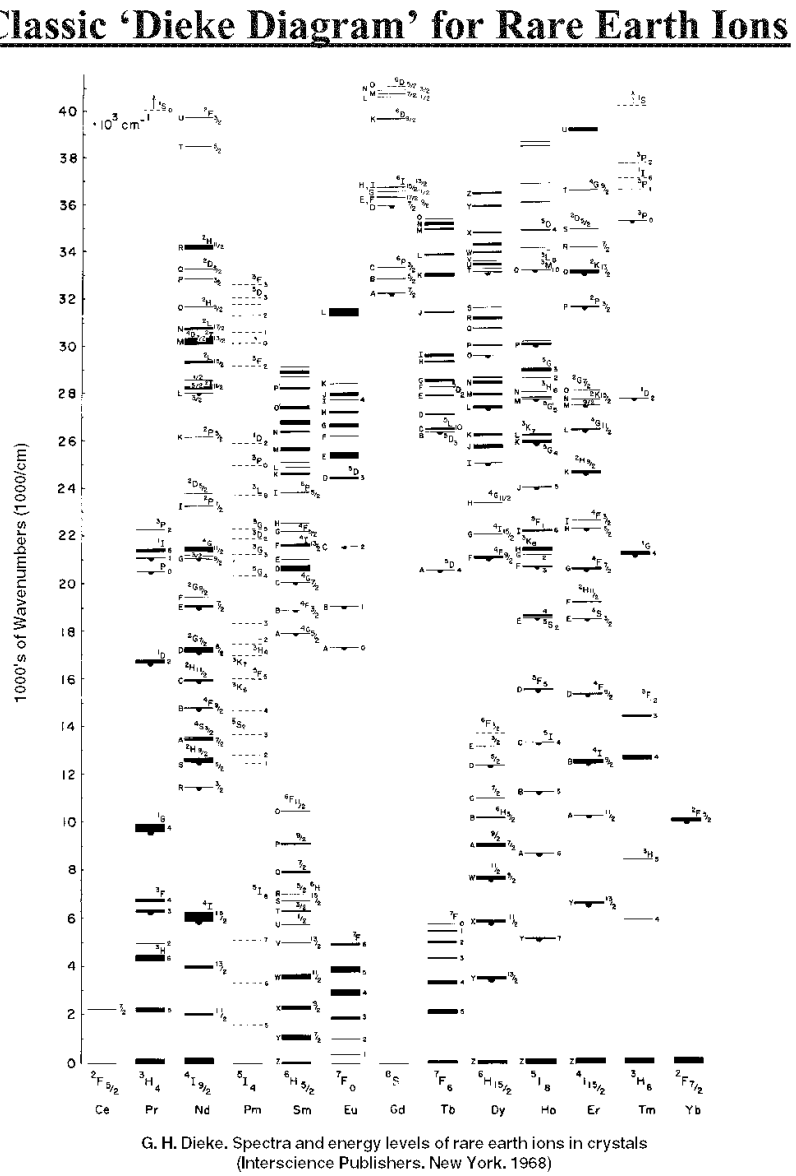

Fig. 1.1

The electrical transition ($^3F_4 \rightarrow {}^3H_6$) of thulium ions is a well-known transition used as 2 μm light source. Thulium, the atomic number is 69,was discovered by Per Theodor Cleve, a Swedish chemist, in 1879, while looking for impurities in erbia, the oxide of erbium (Er_2O_3). Cleve named the oxide thulia and its element thulium after Thule, an ancient Roman name for a mythical country in the far north, perhaps Scandinavia. The energy level diagram of Tm^{3+} is shown in Fig. 1.2. Tm^{3+} has a strong absorption band around 790 nm, for which the high-powered and commercially available GaAlAs laser diode can be used as an efficient and inexpensive pumping source. The broad emission spectrum (over 200 nm) at 2 μm of Tm^{3+} also makes it favorable as tunable laser source. Another feature brought by broad emission band is the possibility of building a quasi-three-level laser system that is more efficient than the normal three-level system.

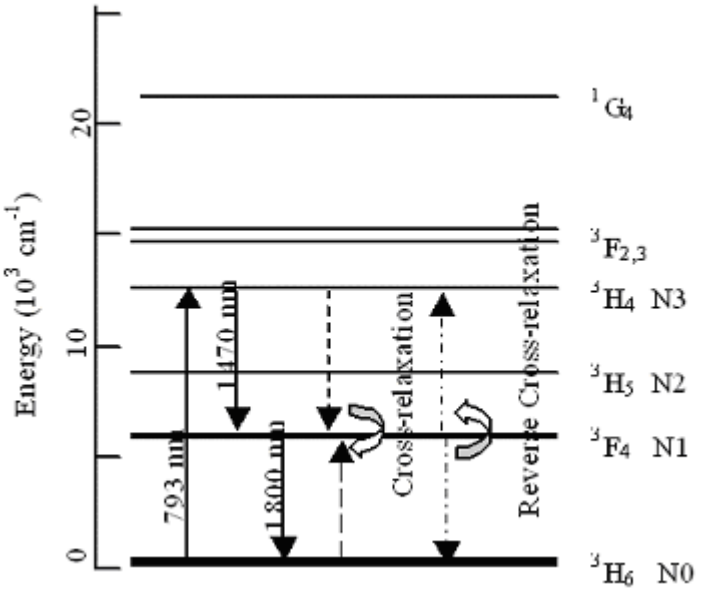

Fig. 1.2 Energy diagram of $Tm3^+$

One attractive pumping mechanism of Tm^{3+} is the cross-relaxation energy transfer between one excited and one ground state thulium ions. When two Tm^{3+} are close enough, the cross-relaxation energy transfer ($^3H_4$, $^3H_6 \rightarrow {}^3F_4$, $^3F_4$) will be triggered: One Tm^{3+} at ground state ($^3H_6$) gets excited to the upper laser level ($^3F_4$) by absorbing the energy released from another nearby excited Tm^{3+} which decays from $^3H_4$ state to the $^3F_4$ state during the cross relaxation energy transfer process. Under such mechanism, two Tm^{3+} ions at ground state get excited to the upper laser level ($^3F_4$) by absorbing only one pumping photon at 790 nm that overlaps the ground absorption band of $^3H_4$. Therefore, quantum efficiency of Tm^{3+} at 2 μm emission region larger than one is attainable under above condition. Quantum efficiency of Tm^{3+} that was larger than one has been reported[1.7]. Such high quantum efficiency leads to little heat generation which is a serious issue when rare earth doped lasers works at high power region.

1.2.2 Host material

The first rare earth laser action was achieved in 1961, one year after the birth of first laser, by L. F. Johnson and K. Nassau in Nd^{3+} : $CaWO_4$ [1.8]. Since then laser actions have been demonstrated from trivalent rare earth (Nd^{3+}, Er^{3+}, Tm^{3+}, Ho^{3+}, Ce^{3+}, Pr^{3+}, Gd^{3+}, Eu^{3+}, Yb^{3+}) in various hosts (crystal and glass) and constructions (rod, microchip, microcavity, disk, waveguide, and fiber). The most common hosts for rare earth doped laser are crystal and glass.

A crystal is a solid in which the constituent atoms, molecules, or ions are packed in a regularly ordered and repeating pattern extending in all three spatial dimensions. In a

crystal laser the active medium is composed of ionic species supported in a crystalline host. The first laser in the world employed a ruby rod as host in which chromium ions as the active medium were supported in an aluminium oxide (sapphire) crystal. One of the most common crystal lasers involves neodymium atoms in a yttrium aluminium garnet host crystal (the YAG:Nd laser).

Glass is defined in ASTM as 'an inorganic product of fusion which has been cooled to a rigid condition without crystallization'. It forms an important host family for rare earth ions because of its good mechanical, thermal, and optical properties. Compared with crystal, glass is of significant low cost to fabricate. Rare earth ions can also be easily doped and uniformly distributed into the glass. The possibility of some glass to be drawn into fiber has opened plenty of opportunities, as well. In glass rare earths exhibit quite broad absorption and emission transitions, whose bandwidths range from tens of to hundreds of nanometer. Such a broad linewidth results from inhomogeneous broadening caused by the lack of regularity of structure in glass. The broad absorption band of glass material reduces the wavelength tolerance for pump source, while the broad emission band is favorable for a tunable laser source.

One common group of glass used for mid-infrared application is Fluoride glass discovered by Poulain and Lucas in 1975 at the University of Rennes [1.9]. But in general the typical fluoride glass has a low glass transition temperature; is considerably less stable; and has failure strains of only a few percent compared with silica's greater than 5%.

Oxide glass shows a superior refractory nature, thermal shock resistance, and high chemical durability. The heavy metal oxide glasses have found ample applications in opto-electronics and photonics because of their optical properties, such as refractive indices, optical non-linearities and infrared transmittance up to 8 μm providing the possibility to develop more efficient lasers and fiber optic amplifiers at longer wavelengths than what's available from other oxide glasses. The broad infrared transmission is a consequence of the small field strengths and relatively large masses of the components of these glasses. Inasmuch as the emission quantum efficiency from given level depends strongly on the phonon energy of the glass hosts, and the high refractive index can enhance radiative transitions in rare-earth ion [1.10].

1.2.3 Laser cavity

In addition to the gain material, most lasers require a laser cavity (or laser resonator), in which light can get amplified by oscillating and passing the gain media. Laser resonators can be classified as stable or unstable. Both types are capable of generating stable optical beams of high quality. For stable resonator, the optical phase of light inside of cavity ramains the same after a roundtrip then a constructive interference can be built up and achieve high cavity intensities. The unstable resonator is first proposed by Siegman A.E. for the cavity used for high-power or high-energy application [1.11]. They have large mode volume which means that they can develop high power without concerning the damage of the gain and cavity.

Microcavity resonators have received considerable attention in both fundamental and application field. Cavity that has a high quality (Q) value and a geometric dimension comparable to the wavelength of light is called microcavity. Microcavities made of various materials have been reported, such as liquid droplet, glass microsphere, semiconductor microdisk, polymer microring, and asymmetric fiber. Microsphere is one of the microcavities that has the highest Q value and is characteristic of the optical WGM supported within the cavity [1.12]. Light can propagate around microsphere with almost no loss, the propagation mode is called whispering gallery mode. The WGMs propagate around the sphere equator by total internal reflection, remaining confined in a thin layer beneath the surface of the sphere. As a result, microsphere can be used as high Q cavity for laser applications.

Although the first fiber laser was built in 1961 only one year after the first laser, it was not until the late 1980s that fiber lasers drew serious attentions, following the development of the Erbium Doped Fiber Amplier (EDFA). Now it becomes the hottest research topic in laser area. In a fiber laser, the laser light is channeled in fiber core due to its confining waveguide structure. Such confinement increases the pump density and the laser efficiency. As a result lots of laser of 3-level system of high inversion threshold can be demonstrated. The fiber waveguiding also alleviates the mechanism alignment and provide the environmental stability. Compared with bulk solid state laser, fiber laser has the advantages of thermal management, diffraction limited beam quality, high efficient, compact package, and low cost. According to many in the laser industry, fiber

lasers are now a serious alternative to solid-state and carbon dioxide lasers for both industrial applications and fundamental researches.

The first Tm-doped fiber laser, demonstrated by Southampton in 1988 [1.13]. Tm_2O_3 was doped into a single mode silica fiber with a doping concentration of 884 ppm ($6.5*10^8$). A Nd:YAG solid state laser at 1064 nm was used as pumping source. In the following 10 years, various glasses, such as ZBLAN [1.14] and lead-germanate glasses [1.15], were investigated as the host material for thulium doped fiber laser. The motivation is to find a material with low phonon energy that helps to increase the quantum efficiency by reducing the multi-phonon decay rate of the laser transition. During that time, all kinds of pumping sources, such as Ti:sapphire laser at 793 nm [1.16], Er-doped fiber laser at 1.57 mm [1.17], InGaAs/InP at 1.6 mm [1.18], GaAs laser dide at 790 nm [1.15], and NaCl color-center laser at 1.58 mm [1.19] have been explored. Different pumping scheme have also been studied, such as in band pump, two-photon pump, and direct $^3H_4$ state pump. After year of 2000, with the development of semiconductor and telecom, research interests have been focused onto thulium doped silica fiber laser pumped by high power AlGaAs laser diode. Silica is chosen as the host because of its excellent chemical durability, thermal and mechanic properties, and mature technique for mass production.

Recently with the competition of high power fiber laser development, more and more people realized the importance of the laser efficiency. Thulium has shown its unsurpassed advantage in terms of laser efficiency due to the unique cross relaxation energy transfer process. According to the theory of cross relaxation energy transfer, the

increase of thulium doping concentration is a natural step to further improve the laser efficiency. The highest thulium doping concentration ever reported in fiber laser is 2.2 wt% in silica fiber. New host glass needs to be studied to improve the doping concentration of thulium without cluster effects.

1.3 This dissertation

In this dissertation, the spectroscopic properties of thulium doped tellurite and thulium doped germanate glass are characterized. The fundamental mechanism of cross relaxation energy transfer is examined through ab-initio calculation. Both 1.9 micron and 1.5 micron laser actions in thulium doped tellurite glass microsphere are presented. Highly efficient and single frequency lasers at 1.9 micron is demonstrated in thulium doped germanate fiber laser.

Chapter 1. Introduction. Research motivation is provided in this chapter. Brief reviews on the related research topics, such as rare earths material, solid state host material, and different laser cavities are presented as well.

Chapter 2. SPECTROSCOPY STUDY OF THULIUM DOPED GLASS. The detailed process of thulium doped tellurite glass preparation is laid out. Absorption and emission spectra, lifetime, Fourier Transform Infrared Spectroscopy (FTIR), and thermo-gravimetric analysis are utilized to characterize the thulium doped tellurite bulk glass samples. Judd-Oflet theory, Fuchtbauer-ladenburg theory, Kushida's model, Burshtein's hopping model, Miyakawa's non-resonant energy transfer model are employed in ab-initio calculation of cross relaxation energy transfer. Rate equations are used in simulation to analyze the cross relaxation energy transfer involved in fluorescence measurement. Dipole-quadrupole interaction is considered to be the most dominant

mechanism of energy transfer based on the comparison between experimental results and theoretical simulations.

Chapter 3. Thulium Doped Tellurite Glass Microsphere Laser. The techniques for fabrication of thulium doped tellurite glass microsphere and fiber taper are described. A tapered fiber is used to couple the pump light into and signal light out of the microsphere. Whispering-gallery-modes of microsphere at 2 μm region are observed. Single mode 2-μm laser is demonstrated from tellurite microsphere with high thulium doping concentration. General laser condition for self-terminating transition is discussed and concluded. Demonstration of 1.5-μm laser is achieved from a self-terminating transition of thulium doped in tellurite microsphere with a low doping concentration.

Chapter 4 Thulium doped Germanate Fiber Laser. Spectroscopic characterizations of thulium doped germanate glass have been examined. Continues wave 1.9-μm fiber lasers have been realized in a short highly thulium doped germanate fiber. The slope efficiency of the fiber laser is 58%, which indicates a quantum efficiency of 1.79. Thermal tuning method is used to characterize fiber bragg gratings, such as linewidth and reflectivity. Single frequency laser operation at 1.9 micron has been successfully accomplished. A fiber based Fabry-Perot interferometer is utilized as a scanning filter to examine the single frequency operation.

CHAPTER 2 SPECTROSCOPY STUDY OF THULIUM DOPED GLASS

2.1 Introduction

The spectroscopy of rare earth doped material is the backbone in material design and fundamental science research. All the photonics device performances such as, gain of amplifier, slope efficiency of laser, lasing wavelength, optimal pump wavelength and saturation power, can be traced back to the spectroscopic properties of the material. A comprehensive investigation on material spectroscopy can provide the strengths in the design of device.

It is well known that material used as active resource for laser operation must possess sharp fluorescent lines, strong absorption bands, and reasonably high quantum efficiency for the fluorescent transition of interest. Therefore our study on Tm-doped glass material will be focused on those features through both theoretical and experimental approaches. The object is to provide comprehensive knowledge and review of several optical processes involved in Tm-doped tellurite glass, such as radiative decay, multiphonon decay, energy migration, cross relaxation, and fluorescence decay.

2.2 Glass preparation

In the family of thulium doped glass, tellurite glass is one favorable host because of its low phonon energy that can reduce the probability of multiphonon decay which is a serious problem for host materials used as infrared emission sources. Other advantages of tellurite glass include its low melting temperature [2.1], good infrared transmissivity [2.2], larger nonlinear susceptibility [2.3], and high solubility to rare earth elements [2.4]. Tellurite glasses also offer an opportunity to enhance the emission and absorption cross-sections of rare earths due to the high refractive index of the host, which is larger than 1.95 [2.5-6].

Tm^{3+} doped tungsten tellurite glass with the Tm_2O_3 doping concentration of 0.2 wt%, 0.5 wt%, 1 wt%, 2 wt%, 5 wt% were prepared by melt-casting technique in University of Arizona. The composition of glass is $0.6TeO_2$-$0.25WO_3$-$0.075K_2O$-$0.075Li_2O$. The process of glass fabrication, as shown in Fig.2.1, is based on the fusion of crystalline raw materials into a viscous liquid followed by forming it into a shape and quenching to a glass. A Nitrogen flow is used during the chemical melting process. The thermo-gravimetric analysis is used to study the transition temperature (T_g) of the glass. Fig. 2.2 shows that the transition temperature (T_g) of tellurite glass is 340 °C. Annealing temperature is set a little higher than glass' T_g.

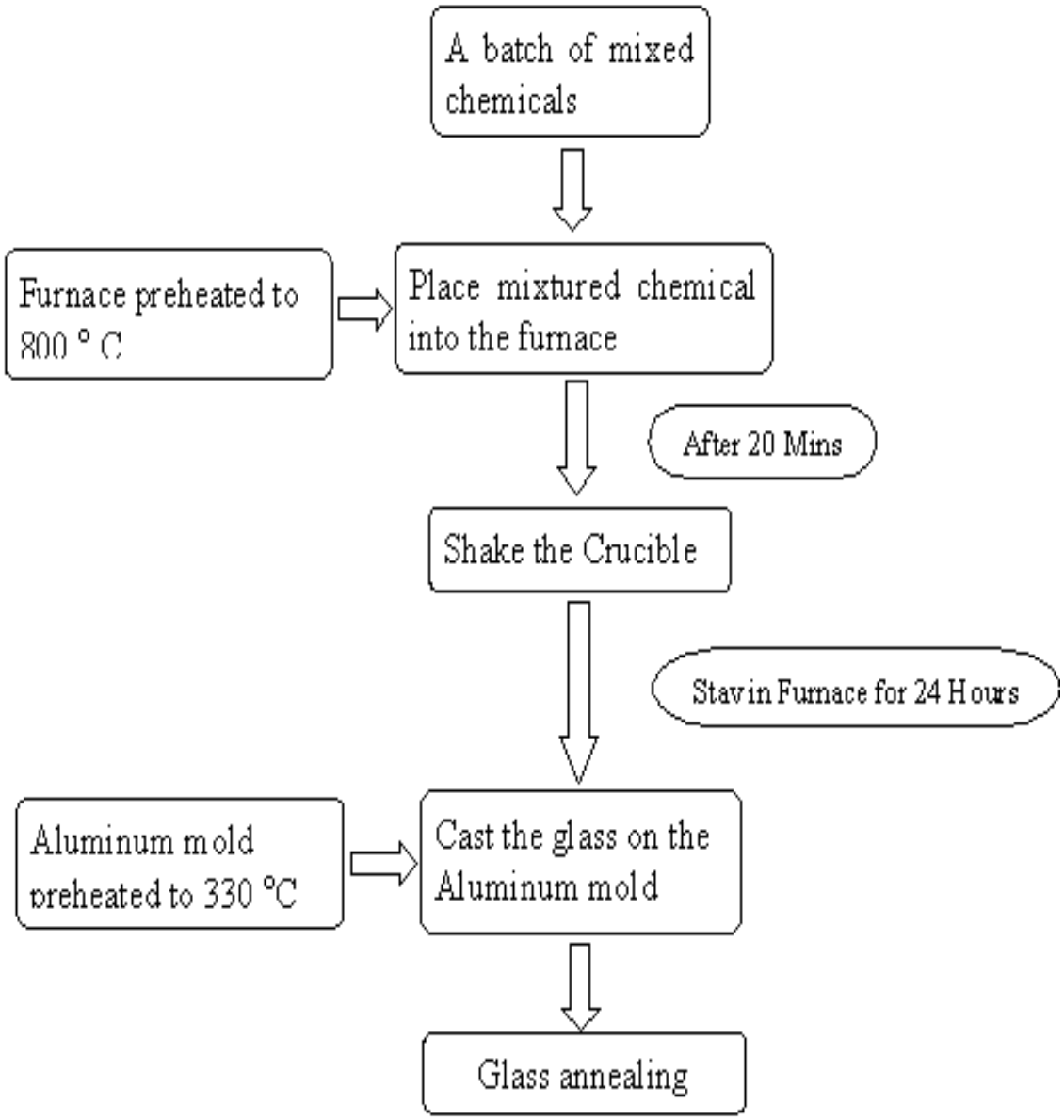

Fig. 2.1 Procedure of thulium doped tellurite fabrication

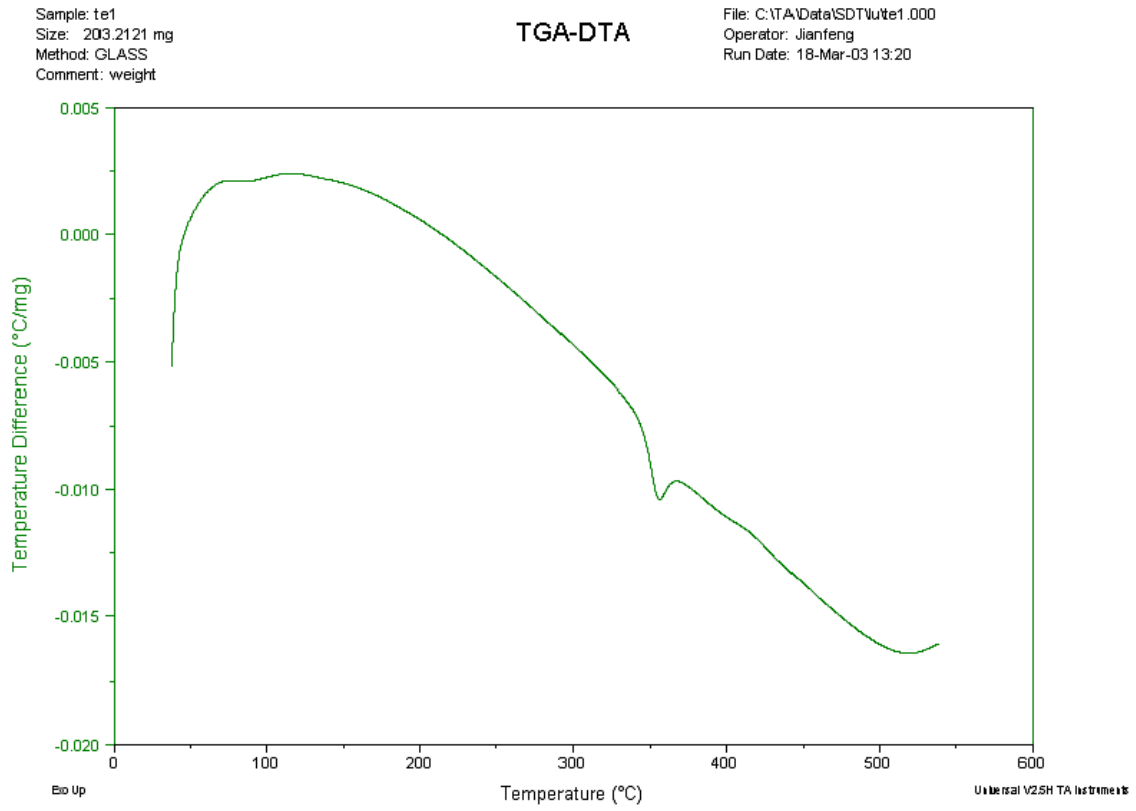

Fig. 2.2 Transition temperature of tellurite glass

The refractive indexes of the glass samples are measured by prism-coupling method at three different wavelengths. The refractive indexes are 2.033, 2.006, and 1.978 at 633 nm , 830 nm and 1550 nm respectively. Then Cauchy's formula,

$$n = 1 + A(1 + \frac{B}{\lambda^2}), \qquad (2.1)$$

is used to simulate the refractive index at different wavelengths, which can be used in the theoretical simulation. The refractive indices versus different wavelengths are plotted in Fig. 2.3.

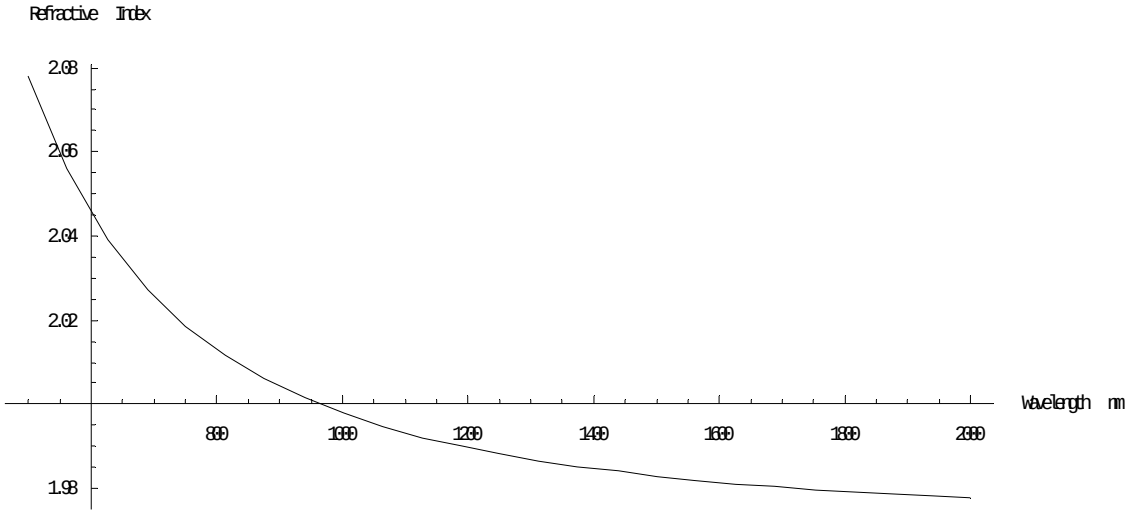

Fig. 2.3 Refractive index of tellurite Vs different wavelength

2.3 Absorption spectrum

The absorption spectra of bulk glass samples with different doping concentrations in VIS-NIR range are taken at room temperature. Fig. 2.4 presents the absorption cross-section of thulium that is calculated from the absorption spectrum of 5 wt% Tm_2O_3 doped tellurite glass sample. Six well-resolved peaks at 1730nm, 1212nm, 793nm, 688nm, 662nm and 473nm are shown in the figure, corresponding to the ground state absorption of $^3F_4$, $^3H_5$, $^3H_4$, $^3F_3$, $^3F_2$ and $^1G_4$ states respectively. There are two distinguished peaks at 473nm band (see the inset of Fig. 2.4), which is unseen in silica glass. It indicates that tellurite-WO_3 glass has a well-defined local environment around Tm ions. Absorption cross-section spectra of glass samples with different doping concentrations are measured and compared as well. There is no absorption-broaden has been observed.

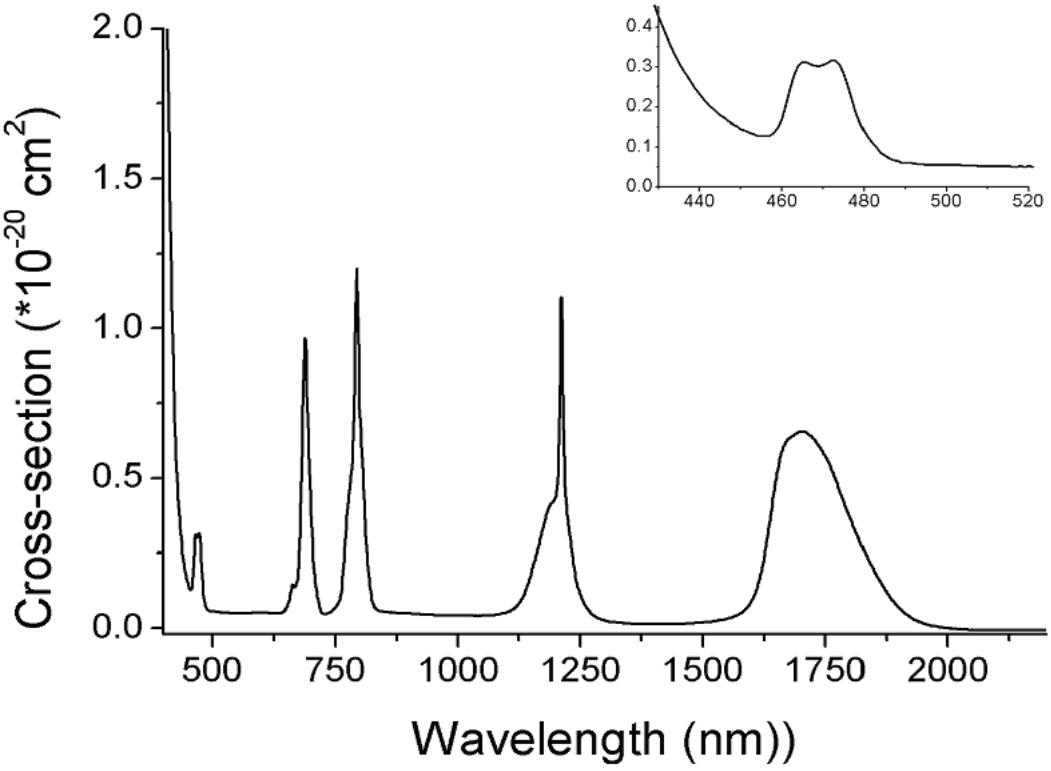

Fig. 2.4 Absorption cross section of Tm3+ doped in tellurite glass

Fourier transform infrared spectroscopy (FTIR) is used primarily for qualitative and quantitative analysis of organic compounds, and also for determining the chemical structure of many inorganics. In this dissertation, FTIR is used to measure the phonon energy of the glass sample. The absorption spectrum is shown in Fig. 2.5. The cut-off phonon frequency of the glass is measured 929 cm^{-1}, which is associated with the WO^{3-} group in the glass matrix.

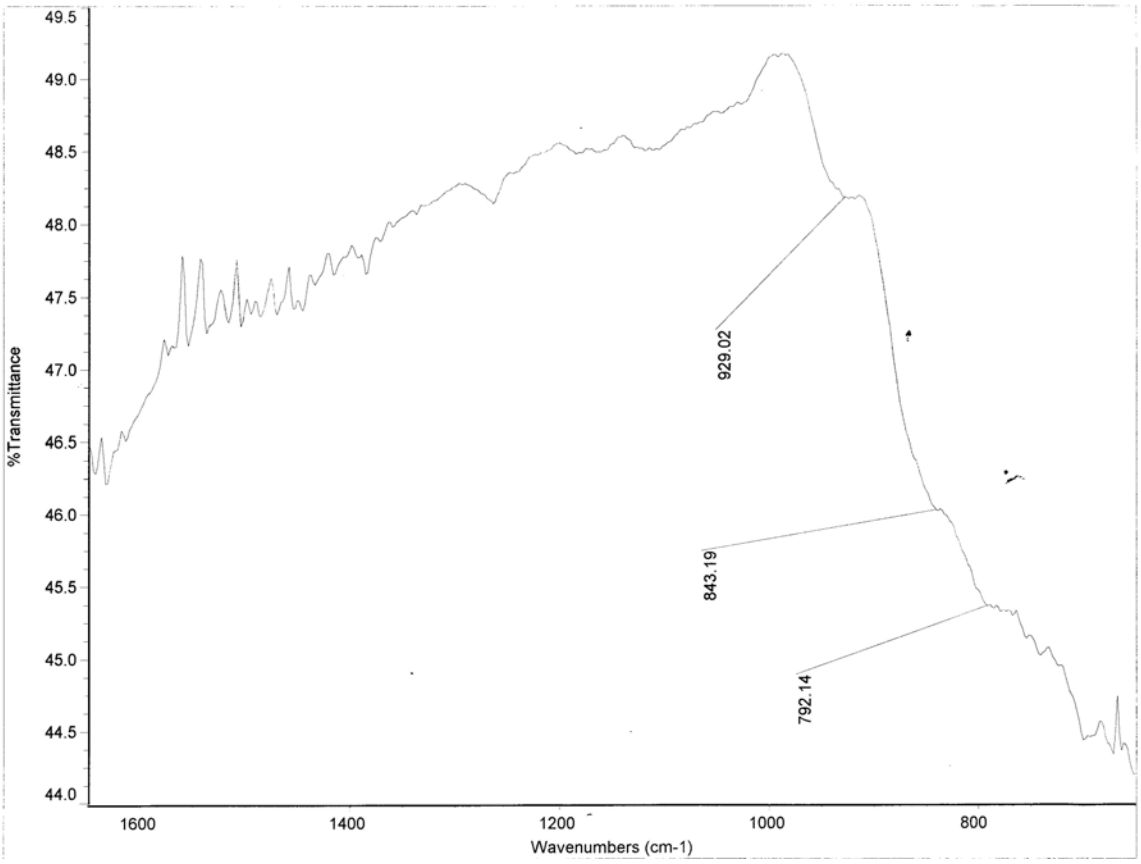

Fig. 2.5 FTIR spectrum of Tm-doped tellurite glass

2.4 Emission Spectrum

The emission spectra of glass samples with different doping concentrations are measured under room temperature. The set-up for fluorescence measurement is shown in Fig. 2.6. A Ti:Sapphire (Tsunami) continuous wave laser tuned to 793 nm is used to excite ground state Tm^{3+} ions to $^3H_4$ state for the luminance measurement. The fluorescence from the glass sample is collected at 90 degree to the pumping laser to avoid the stimulated emission and re-absorption from ground state Tm^{3+} ions. The emission

fluorescence of transitions $^3H_4 \rightarrow {}^3F_4$ (1.5 μm) and $^3F_4 \rightarrow {}^3H_6$ (1.8 μm) are dispersed by a 1/4m monochrometer, detected by a cooled InAs detector, and amplified by a lock-in amplifier. The emission measurement system is calibrated for the relative intensity of different wavelengths.

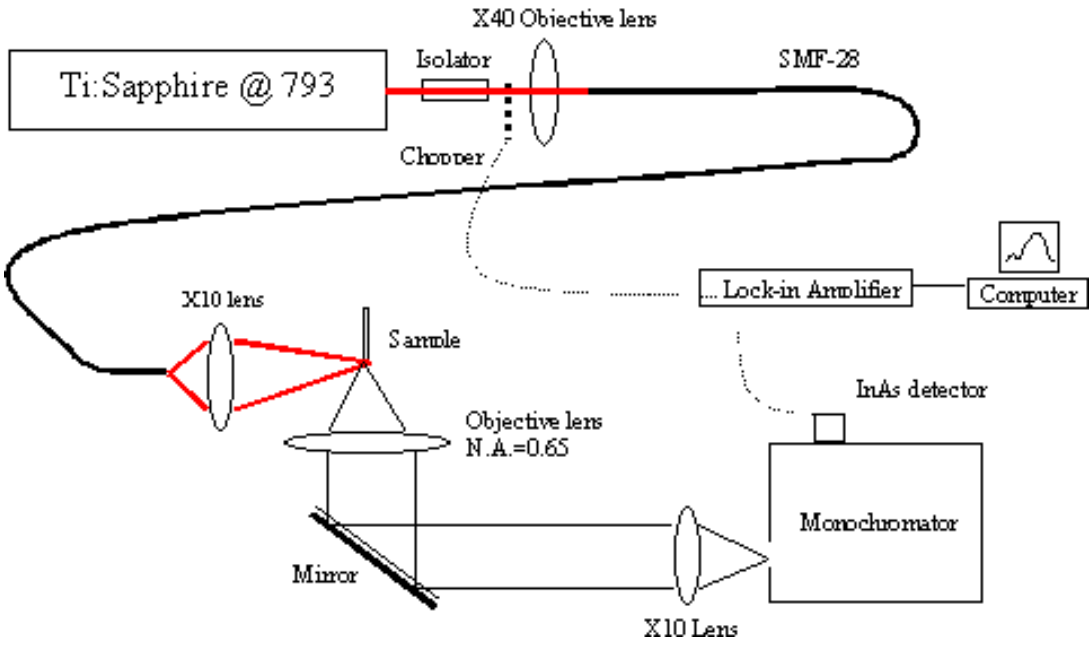

Fig. 2.6 Bulk glass emission spectrum setup

Fig. 2.7 illustrates the emission spectra of Tm-doped tellurite glass samples with different doping concentrations. It shows that the fluorescence intensity of 1.5-mm transition band declines with the increase of Tm^{3+} ions doping concentration. The reduction of 1.5-mm fluorescence intensity originates from the cross relaxation energy transfer (see section 2.7). According to the theory of multi-polar interaction, the closer Tm^{3+} ions are, the higher transfer rate they get. Therefore, when the doping

concentration increases, the cross relaxation energy transfer rate becomes so large that most Tm^{3+} ions at $^3H_4$ state would nonradiatively decay to $^3F_4$ state through cross relaxation energy transfer rather than radiatively decay to $^3H_4$ state by emitting 1.5 μm photons.

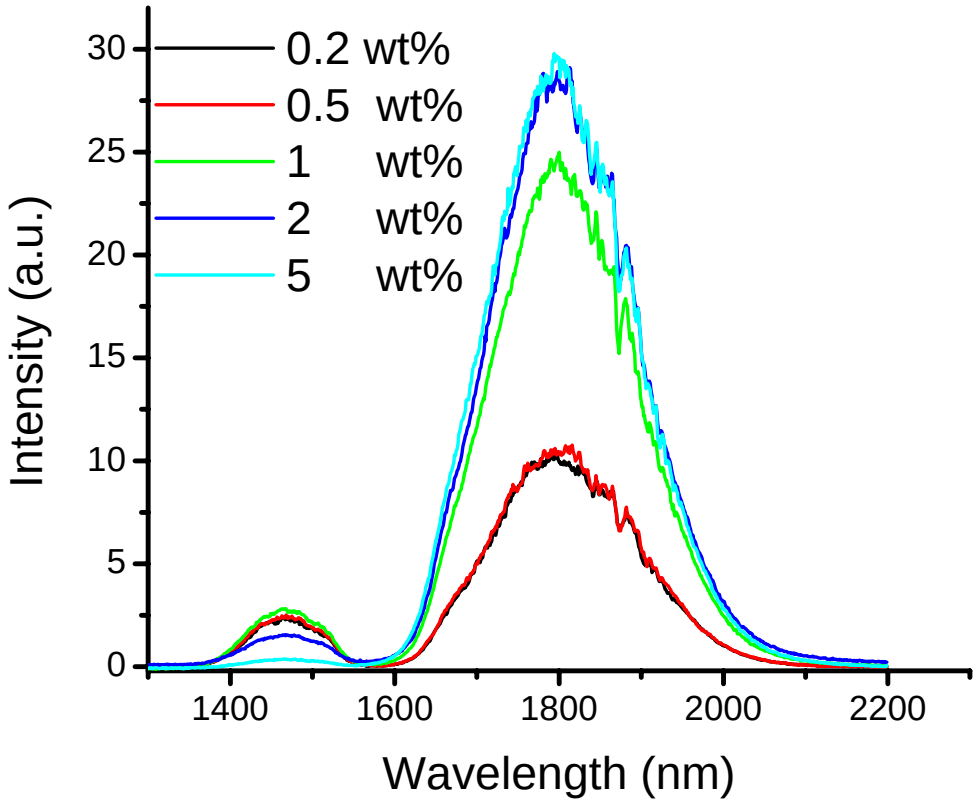

Fig. 2.7 Emission spectrum of glass sample with different doping concentrations

The Fuchtbauer-ladenburg equation is utilized to determine the emission cross section of Tm^{3+} [2.7]. The F-L method has been commonly used for rare earth elements and is

grounded in the fundamental of the Einstein A and B coefficients. The equation is expressed as,

$$\sigma_e = \frac{\lambda^4 A_R}{8\pi c n^2} f(\lambda) \tag{2.2}$$

where $f(\lambda)$ is the normalized line shape of the emission spectrum, n is the refractive index of the material, and A_R is the spontaneous emission rate of the transition calculated by Judd-Oflet theory (See section 2.5). The emission cross section of transition ($^3F_4 \rightarrow {}^3H_6$) of Tm^{3+} doped in tellurite glass is shown in Fig. 2.8.

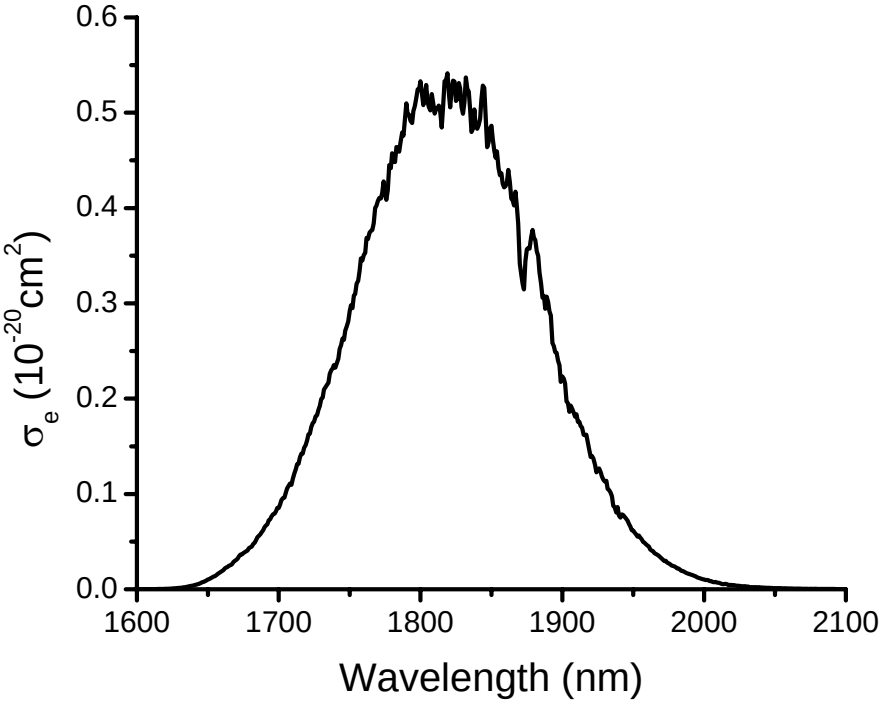

Fig. 2.8 Emission cross section of Tm3+ in tellurite glass

2.5 Judd-Oflet Theory

As mentioned in Chapter 1 that the 4*f* electron configuration of the rare earth ions is insensitive to the local environment, because of the shield effect from the outmost shell 5s and 5d. But the transition probabilities between 4*f* states are very sensitive to the local ions and hosts. Laporte's rule in quantum mechanism forbids transitions between 4f electrons because of the no change of parity between the states involved. In the case of glass, the slight field-induced mixture between 4f and other wave functions creates a little probability of transition between $4f^n$ electrons. Compared with electric quadrupole and magnetic dipole transition, electric dipole transition dominates in most $4f^n$ transitions in rare earth materials [2.8,2.9].

One of the important properties for the evaluation of the host glasses is the spontaneous emission probability for the 4f–4f transitions of the rare-earth ions doped in glasses. It is directly related to the stimulated emission cross-section, radiative quantum efficiency, and fluorescence branching ratio. The transition probability associated with different pairs of energy level can be calculated by Judd-Oflet theory.

According to Judd-Oflet theory, the oscillator strength S_{ed} of an electric dipole transition between states $|\Psi_i\rangle$ ($^{2s+1}L_J$) and $|\Psi_f\rangle$ ($^{2s'+1}L'_{J'}$) is given by

$$S_{ed} = \frac{1}{e^2}\left|\left\langle \Psi_f \left| H_{ed} \right| \Psi_i \right\rangle\right|^2 = \sum_{k=2,4,6} \Omega_k \left|\left\langle f^N \gamma S' L' J' \left| \mathrm{H}_{ed} \right| f^N \gamma S L J \right\rangle\right|^2 \tag{2.3}$$

where H_{ed} is the electric dipole Hamiltonian, J-O parameters Ω_k (k=2,4,6) are the coefficients of different crystal field, and $U^{(t)}$ (t=2,4,6) are reduced tensor operator components including the spin-orbit mixing of the LS terms. Usually the reduced matrix

of electric transition of 4f electrons are host independent due to the screen effect caused by the external shell of 5s and 5p of rare-earth ions and have been tabulated for most rare earth material. Eq (2.3) shows that the sum of the products of Ω_k and doubly reduced matrix $U^{(t)}$ (t=2,4,6) can be used to identify the radiative process of the doping rare-earth ions. We use the calculated $U^{(t)}$ (t=2,4,6) values, listed in Table I, from *crystalline lasers* for our calculation. The corresponding spontaneous emission rate of the transition from (S' L' J') to (S L J) can be described by,

$$A^{ed}_{S'L'J',SLJ} = \frac{64\pi^4 e^2 n}{3h < \lambda >^3} \frac{\chi_{ed}}{2J'+1} S_{ed} \tag{2.4}$$

$$\chi_{ed} = \frac{(n^2+2)^2}{9} \tag{2.5}$$

where χ_{ed} is the local field correction.

For the magnetic dipole transition, the oscillator strength S_{md} is given by,

$$S_{md} = \frac{e\hbar}{2m_e c} \left| \left\langle f^N \gamma S'L'J' \middle| (\hat{L} + 2\hat{S}) \middle| f^N \gamma SLJ \right\rangle \right|^2 \tag{2.6}$$

where L+2S is the MD operator. It's spontaneous emission rate can be described by,

$$A^{md}_{S'L'J',SLJ} = \frac{64\pi}{3 < \lambda >^3} \frac{\chi_{md}}{2J'+1} S_{md} \tag{2.7}$$
$$\chi_{md} = n^3$$

where χ_{md} is the local field correction for MD transition.

The experimental oscillator strengths S_{exp} of the transitions can be obtained by integrating absorbance for each band,

$$S_{\exp} = \frac{3hcn}{8\pi^3 e^2 < \lambda >} \frac{2J+1}{\chi_{ed}} \int_{band} \sigma_a(\lambda) d\lambda \tag{2.8}$$

where, σ_a is the absorption cross-section, calculated by

$$\sigma = \alpha / \rho \tag{2.9}$$

α is the absorption coefficient of the material, and ρ is the doping concentration.

Table I. Doubly reduced matrix $U^{(t)}$ of Tm^{3+}

Transitions	U2	U4	U6
$^3H_6$ --> $^3F_4$	0.527	0.718	0.228
$^3H_6$ --> $^3H_5$	0.107	0.231	0.638
$^3H_6$ --> $^3H_4$	0.249	0.118	0.608
$^3H_6$ --> $^3F_3$	0	0.316	0.841
$^3H_6$ --> $^3F_2$	0	0.0005	0.258
$^3H_6$ --> $^1G_4$	0.0481	0.0752	0.0119
$^3H_4$ --> $^3H_5$	0.089	0.125	0.905
$^3H_4$ --> $^3F_4$	0.129	0.133	0.213

J-O parameters Ω_k are considered as phenomenological coefficients that reflect host material influences on the $4f$ - $4f$ radiative transitions of rare earth elements. They can be derived by comparing the experimental oscillator strength with theoretical value through least square fitting. Four absorption transitions ($^3H_6 \rightarrow {}^3F_4$, $^3H_6 \rightarrow {}^3H_5$, $^3H_6 \rightarrow {}^3H_4$, $^3H_6 \rightarrow {}^3F_3$) presented in Fig. 2.4 are used to determine the J-O parameters for the thulium doped tellurite glass. The absorption band of $^3H_6 \rightarrow {}^3F_3$ was distinguished from that of

$^3H_6 \rightarrow {}^3F_2$ by fitting two Gaussian peaks into the two overlapping absorption spectrum. The transition of $^3H_6 \rightarrow {}^3F_2$ is ignored because of its small value of reduced matrix element, which would increase the error of the least square fitting. The reduced matrix elements for different transitions of thulium ions are listed in Table II.

The J-O parameters, the calculated spontaneous emission rate, the calculated lifetime, and branch ratio β of different energy levels were calculated and listed in Table II. The radiative lifetimes and branch ratios β of different energy levels are calculated by

$$\tau_R = \frac{1}{\sum_{J'} A(J, J')} \tag{2.10}$$

$$\beta_{J,J'} = A(J, J') / \sum_{J'} A(J, J') \tag{2.11}$$

Table II. Spectrum parameters of Tm3+ doped in tellurite glass

Ω_2	$5.96 \mu 10^{-24}$ m^2
Ω_4	$2.35 \mu 10^{-24}$ m^2
Ω_6	$1.22 \mu 10^{-24}$ m^2
A_{10}	540 s^{-1}
A_{30}	2863.5 s^{-1}
A_{32}	98 s^{-1}
A_{31}	260.5 s^{-1}
τ_{r1}	1.78 ms
τ_{r3}	0.18 ms
A_{32nr}	2302 s^{-1}
α	0.0039
$\hbar\omega$	929 cm^{-1}

W_{etdd}	$3.19\mu10^{-38}$
W_{etdq}	$1..43\mu10^{-51}$
W_{etqq}	$7.96\mu10^{-64}$

The J-O parameters in our glass are also compared with those of different glass hosts and listed in Table III. It shows that tellurite glass had large value of Ω_2. Previous studies revealed that the Ω_2 parameter is indicative of the amount of the covalency of Tm-O bond and is sensitive to the local environments of Tm^{3+} ion sites. Ω_2 parameters related to the rigidity of host or the overlap integrals of the 4*f* and 5*d* orbits, which lead to the big Stark splitting and the broad emission bandwidth.

Table III. J-O parameters of different glass

Glass	Ω_2	Ω_4	Ω_6
Our Glass	5.96	2.35	1.22
BZYT (Fluoride) [2.10]	1.14	1.57	1.13
TGLN (Tellurite) [2.11]	3.37	1.03	8.51
NPBW (fluorophosphate) [2.12]	5.28	2.32	1.16

2.6 Lifetime and multiphonon decay

In addition to the radiative process, excited ions also decays to lower energy level via nonradiative processes such as multiphonon decay, quenching and energy transfer. Therefore the total decay rate can be expressed as,

$$A = A_R + W_{nR} \tag{2.12}$$

$$W_{nR} = W_{multiphonon} + W_{energytransfer} + W_{quench} \tag{2.13}$$

Fluorescence lifetime of a state, which is defined as the average time an excited ion spends on the state, usually is determined by the combination of both radiative and nonradiative processes. Therefore the nonradiative decay rate of a level can be derived by,

$$W_{nr} = \frac{1}{\tau_f} - A_r \,. \tag{2.14}$$

where A_r is the radiative decay rate evaluated from Judd-Ofelt theory, τ_f is the fluorescence lifetime, obtained from fluorescence decay measurement.

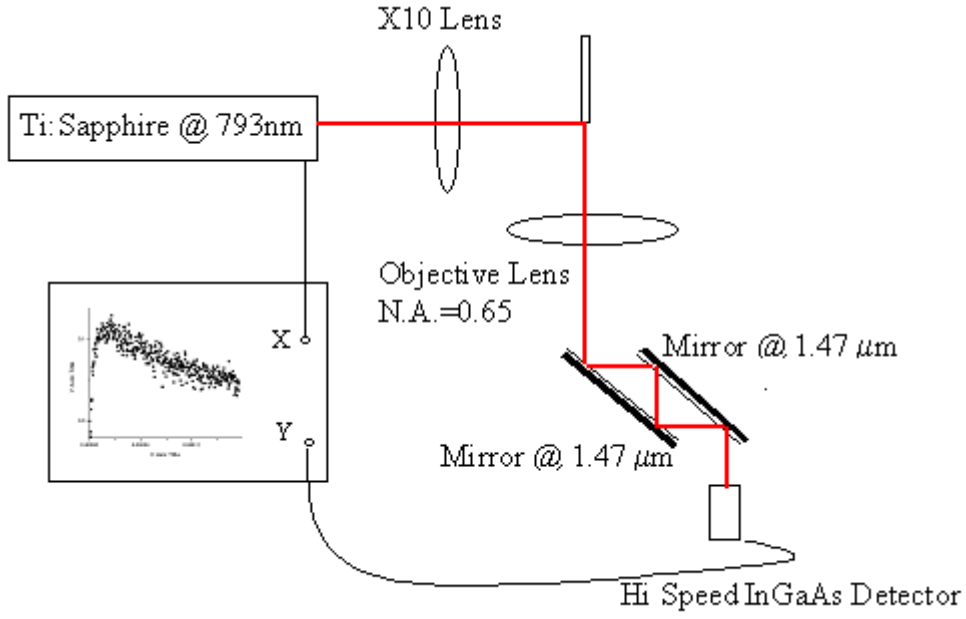

Fig. 2.9 Fluorescence decay of $^3H_4$ level at 1.47 mm

Fluorescence lifetimes of two different energy levels ($^3F_4$, $^3H_4$) are measured to evaluate the nonradiative processes involved in thulium doped tellurite glass. The fluorescence decay of $^3H_4$ state measurement is shown in Fig. 2.9. Because the lifetime of $^3H_4$ state is very short, a 793nm 150 fs pulsed laser beam from Ti-sapphire laser was chosen to directly pump the ground Tm^{3+} to the $^3H_4$ level. The fluorescence decay of 1470 nm from the transition of $^3H_4 \rightarrow {}^3F_4$ was measured by a fast speed InGaAs detector and recorded by a digital oscilloscope. Two mirrors with high reflection at 1.47 mm are used to filter the emission of $^3F_4 \rightarrow {}^3H_6$ transition at 1.8 mm. The lifetime τ is defined as when the intensity of fluorescence decrease to the 1/e of the beginning value.

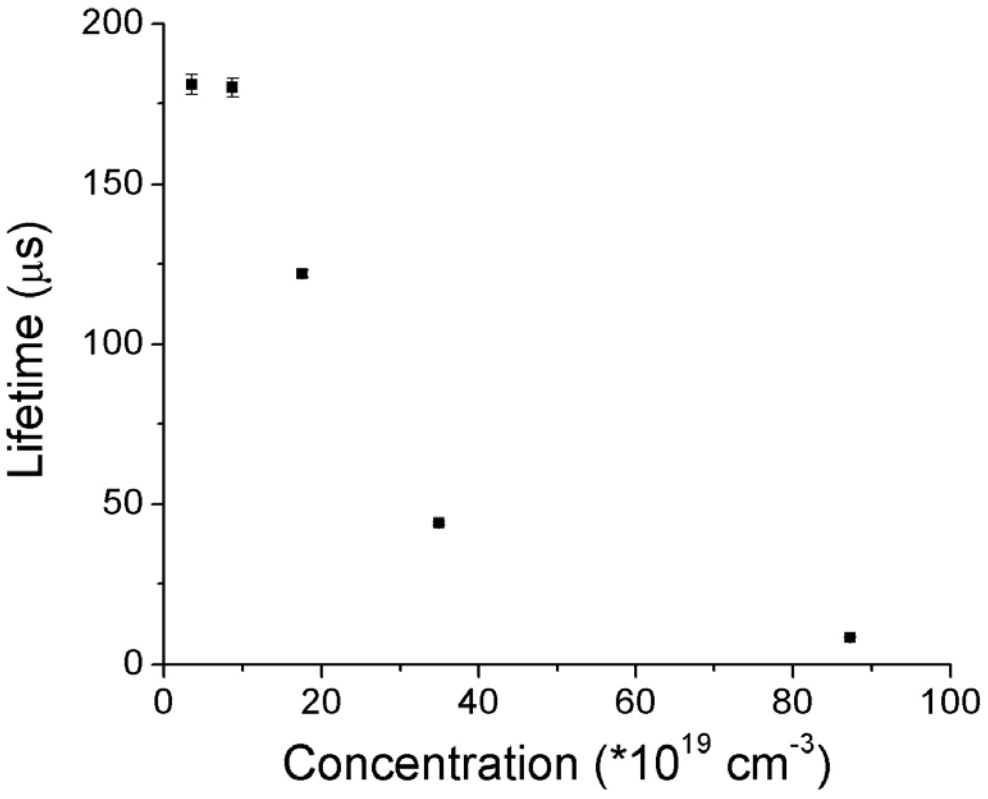

Fig. 2.10 Lifetime of $^3H_4$ level of Tm^{3+} with different doping concentrations

Fig. 2.10 illustrates the measured lifetimes of $^3H_4$ state of thulium ion versus different doping concentrations. It clearly shows that when doping concentration is higher than 0.5 wt% (8.7×10^{19} cm^{-3}), the lifetime of $^3H_4$ level will dramatically drop. One reason is that high concentration brings Tm^{3+} ions close enough to make the cross-relaxation energy transfer ($^3H_4$, $^3H_6 \rightarrow {}^3F_4$, $^3F_4$) occur, which decreases the population of $^3H_4$ state quickly by transferring energy to nearby ground-state ions. According to Fig. 2.10, it is reasonable to assume that there is no cross relaxation energy transfer when the doping concentration is lower than 0.5%, since the lifetime doesn't change when the doping concentration increased from 0.2 % to 0.5 %. Therefore, the decay of $^3H_4$ state of glass samples with low doping concentration (0.2 wt% and 0.5 wt%) is comprised of two processes: spontaneous emission and multi-phonon relaxation, assuming there is no concentration quench in low concentration glass samples. By comparing the measured lifetime of the sample with the lowest concentration with the radiative decay rate calculated by J-O theory, we obtain the multiphonon decay rate of $^3H_4$ level by Eq. (2.14).

The lifetime of $^3F_4$ state measurement is shown in Fig. 2.11. An 808nm AlGaAs laser diode, which is modulated by a function generator, is used to excite Tm^{3+} ions to $^3H_4$ state. The fluorescence decay of 1.8 mm from the transition of $^3F_4 \rightarrow {}^3H_6$ is dispersed by monochrometer (oriel MS 257) and measured by an InAs detector and recorded by a digital oscilloscope. In order to avoid the delay of the lifetime due to reabsorption from unexcited thulium ions, the fluorescence of 1.8 μm is collected at 90 degree from the

incident pumping laser, detected by an InAs detector and recorded by a digital oscilloscope.

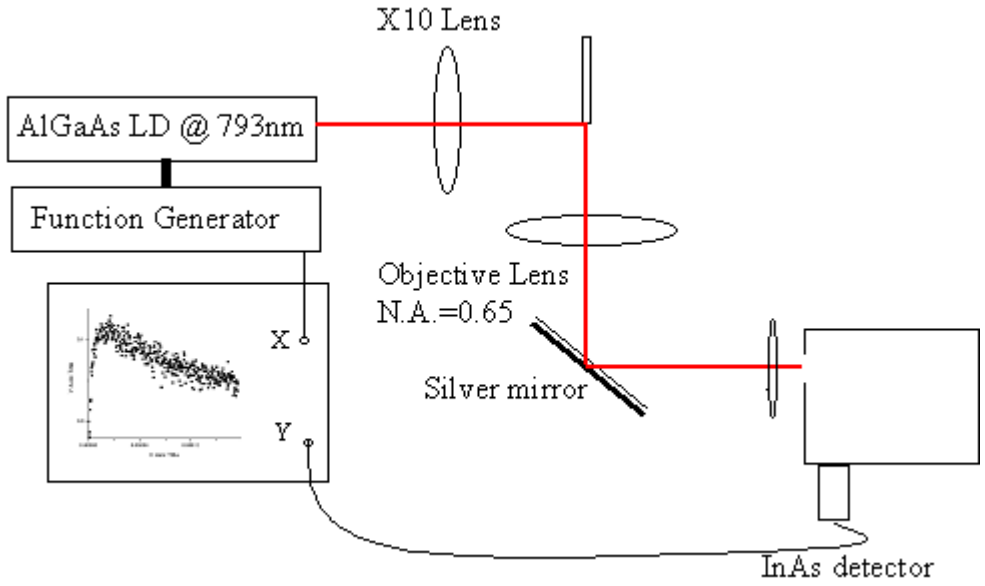

Fig. 2.11 Setup for measurement of fluorescence decay $^3F_4$ state

Fluorescence decay curves of transition $^3F_4 \rightarrow {}^3H_6$ in glass samples with different thulium oxide doping concentrations are shown in Fig. 2.12. The lifetime τ is defined as when the fluorescence decrease to the 1/e of the beginning intensity. It shows that lifetime of $^3F_4$ state drops when the doping concentration is increased. Unlike the reduction of lifetime of $^3H_4$ state, the decline of lifetime in $^3F_4$ results from concentration quenching. In Tm-doped glass, concentration of $^-$OH radical has great impact on the lifetime of $^3F_4$ state due to the overlap between absorption band of $^-$OH radical and emission band of transition of $^3F_4$ -> $^3H_6$. The increase of doping concentration enhances the probability of one excited Tm^{3+} ion meeting a quenching center, such as OH radical,

through a nonradiative energy migration process between Tm^{3+} ions. The nonradiative decay rates of Tm3+ at 3F4 states in different glass samples are also calculated by Eq. (2.14)

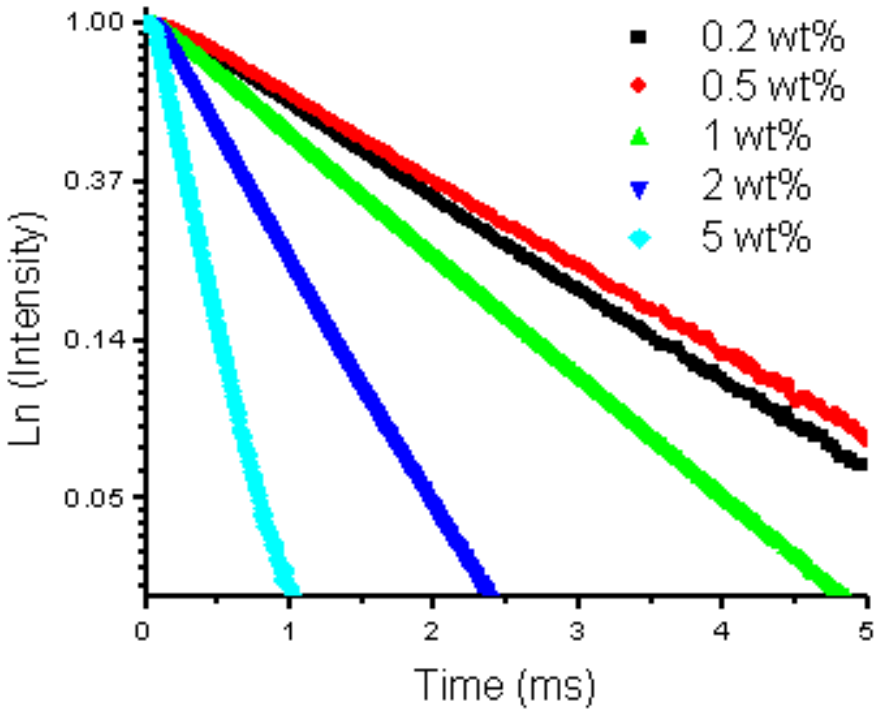

Fig. 2.12 Fluorescence decays of $^3F_4 \rightarrow {}^3H_6$ transition.

According to the model of multi-phonon decay, the non-radiative decay rate can be described as [2.13],

$$A_{nr} = C \times \left[1 + \frac{1}{Exp(\hbar\omega / kT) - 1} \right]^{\Delta E / \hbar\omega} \times e^{-\Delta E \times \alpha} \qquad (2.15)$$

where C and α is host –dependent parameters, $\hbar\omega$ is the phonon frequency, ΔE is the energy gap of the transition, k is the Boltzman constant and T is the temperature of the material. $1/(\exp(\hbar\omega/k_B T)-1)$ is the Bose-Einstein occupation number or mean population of the phonon mode. $\Delta E/\hbar\omega$ is the number of phonon involved. In our model α is calculated by solving the equation of,

$$\frac{A_{31}^{nr}}{A_{10}^{nr}} = [1+\frac{1}{Exp(\hbar\omega/kT)-1}]^{(\Delta E_{31}-\Delta E_{10})/\hbar\omega} \times e^{-(\Delta E_{31}-\Delta E_{10})\alpha} \quad (2.16)$$

where A_{31}^{nr} and A_{10}^{nr} are the multiphonon decay rates of transition $^3H_4 \rightarrow {}^3F_4$ and $^3F_4 \rightarrow {}^3H_6$. They are obtained by applying Eq. (2.14) onto the lifetime results of glass with 0.2 wt% doping concentration, in order to eliminate the effect of cross relaxation and concentration quenching. By submitting α back into the Eq. (2.15), we can get the value of host dependent parameter C (5.7×10^{10}), which is quite close to the reported value of C (6.3×10^{10}).

2.7 Cross relaxation energy transfer

2.7.1 Mechanism of cross relaxation

Previous study only concerns the transition of an isolated ion. Another major contributor to the non-radiative decay is energy transfer that occurs between ions. There are several kinds of energy transfers, such as cross relaxation, up-conversion and concentration quenching. Cross relaxation is a process in which an excited ion transfers part of its energy to a neighboring ion. Fig. 2.13 illustrate the cross relaxation processes

in thulium doped material. One ground state Tm^{3+} gets excited to $^3F_4$ state; then relaxes to $^3H_4$ state by transferring the energy to a neighboring ground state Tm^{3+} that gets excited to $^3F_4$ level as well.

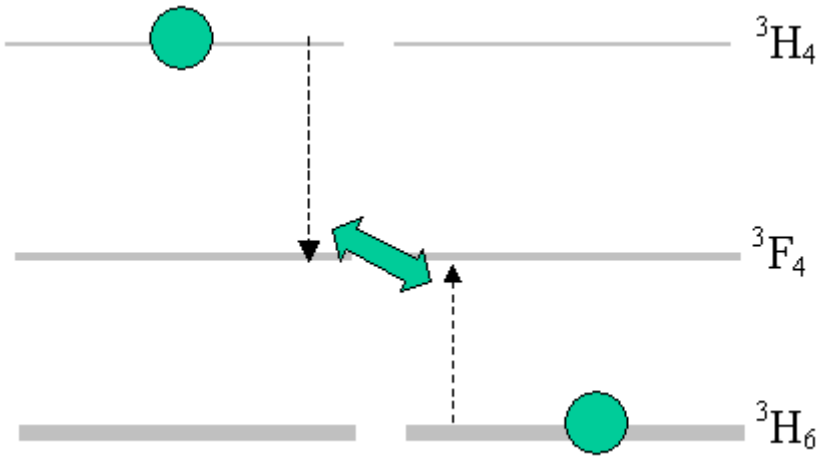

Fig. 2.13 Cross relaxation energy transfer between two nearby trivalent thulium

The dominant mechanism of the energy transfer between rare-earth ions in solid materials, especially that of Tm^{3+}, needs to be well understood in order to develop more efficient laser and amplifier material. Dexter [2.14] and Forster [2.15] first developed the theory of energy transfer in solid state based on ion-ion interaction produced by electric multi-polar interaction rather than emission and reabsorption of fluorescence, although the latter can be significant over longer distances. Most studies of Tm^{3+}: Tm^{3+} energy transfers were based on the dipole-dipole interaction. Some papers considered the high order multi-polar interactions as the main mechanisms of the cross-relaxation energy transfers of Tm^{3+} [2.16,2.17]. Few papers claimed that dipole-quadrupole interaction

played the most important role in the cross-relaxation energy transfer [2.18,2.19]. Because one feature of Tm-doped glass laser is its unique pumping mechanism which can dramatically improve the overall efficiency of the laser at mid-infrared range, to study the fundamental physics of the energy transfer becomes a key to maximize the advantage of cross relaxation of Tm^{3+}.

Dexter first established the theory of sensitized luminescence in solid material. In Dexter's model the overlapping of the "near zone" electric fields instead of the wave function is used to explain the transfer mechanics, because the f-orbital of rare-earth ions are well located by out shell. Kushida then developed a model that used a tensor operator method to take into account the individual characters of the energy levels involved in the transition [2.20]. In Kushida's Model the crystal-field splitting was assumed so small that all the stark components had the same population. The transition probabilities of different multi-polar interaction were expressed as,

$$P_{D-A}^{dd} = \frac{1}{(2J_D+1)(2J_A+1)}\left(\frac{2}{3}\right)\left(\frac{2\pi}{\hbar}\right)\left(\frac{e^2}{R^3}\right)^2 \left[\sum \Omega_{D\lambda} < J_D \| U^{(\lambda)} \| J_D' >^2\right] \times \left[\sum \Omega_{A\lambda} < J_A \| U^{(\lambda)} \| J_A' >^2\right] S, \tag{2.17}$$

$$P_{D-A}^{dq} = \frac{1}{(2J_D+1)(2J_A+1)}\left(\frac{2\pi}{\hbar}\right)\left(\frac{e^2}{R^4}\right)^2 \left[\sum \Omega_{D\lambda} < J_D \| U^{(\lambda)} \| J_D' >^2\right] \times < 4f | r_A^2 | 4f >^2 < f \| C^{(2)} \| f >^2 < J_A \| U^{(2)} \| J_A' >^2 S, \tag{2.18}$$

$$P_{D-A}^{qq} = \frac{1}{(2J_D+1)(2J_A+1)}\left(\frac{14}{5}\right)\left(\frac{2\pi}{\hbar}\right)\left(\frac{e^2}{R^5}\right)^2 < 4f | r_D^2 | 4f >^2 < 4f | r_A^2 | 4f >^2 \times < f \| C^{(2)} \| f >^4 < J_D \| U^{(2)} \| J_D' >^2 < J_A \| U^{(2)} \| J_A' >^2 S, \tag{2.19}$$

where the superscript *dq* and *qq* stand for dipole- quadrupole and quadrupole- quadrupole interactions respectively. J_A, J_D and J'_A, J'_D are the initial and final state of the acceptor

and donor ions. Ω_λ (λ=2,4,6) are the J-O parameters that are used to describe the effect of the crystal field and electronic wave-functions. $U^{(\lambda)}$ are the doubly reduced tensors which represent the coupling effects between rare-earth ions and host material. $C^{(2)}$ is a dimensionless factor depending on the orientation of coordinate axes. S is the integral of the overlap between the lineshapes of the absorption cross-section of acceptor ion and that of the emission cross-section of donor ion. $<4f|r^2|4f>$ is the average radius of the ions. R is the average distance between the doping ions, which is simply given as

$$R = \left(\frac{3}{4\pi N} \right)^{\frac{1}{3}}, \tag{2.20}$$

where N is the doping concentration.

2.7.2 Energy migration

Besides the donor-acceptor energy transfer, donor-donor energy transfer, which is also called energy migration, is another important process involved in the cross relaxation energy transfer of Tm^{3+} ions doped in tellurite glass. Energy migration ($^3H_4$, $^3F_4$ → $^3F_4$, $^3H_4$) would increase the cross relaxation rate because energy migration make the donor ($^3H_4$) have more chances to transfer energy to an acceptor ($^3H_6$). Energy migration model is also a bridge between the micro-parameter such as transfer probability and macro-parameter such as energy transfer rate that can be used in rate equations. Two different models of energy migration have been developed by Yokota [2.21] and Burshtein [2.22]. Tanimoto's model is called the diffusion limited transfer that assumes a strong donor-

acceptor (D-A) transfer. Burshtein's model is called the hopping model in which process the D-D transfer rate is much larger than the D-A transfer rate. In the case of cross relaxation of Tm^{3+} ions, Donor-Donor (D-D) transfer was a resonant energy transfer whose transfer rate was much higher than that of Donor-Acceptor (D-A) transfer that was a phonon-assisted energy transfer. Therefore, instead of diffusion mode, hopping model, which assumes a strong D-D transfer, is adopted in this case. For hopping model, macro transfer rate could be written as,

$$W_{ET}^{dd} = 13(C_{D-A}^{dd})^{1/2}(C_{D-D}^{dd})^{1/2} n_d , \tag{2.21}$$

$$W_{ET}^{dq} = 21(C_{D-A}^{dq})^{3/8}(C_{D-D}^{dq})^{5/8} n_d^{5/3} , \tag{2.22}$$

$$W_{ET}^{qq} = 42(C_{D-A}^{qq})^{3/10}(C_{D-D}^{qq})^{7/10} n_d^{7/3} , \tag{2.23}$$

W_{ET}^{dd}, W_{ET}^{dq}, W_{ET}^{qq} are the transfer rates of the dipole-dipole, dipole-quadrupole, and quadrupole-quadrupole interaction respectively. n_d is the doping concentration and C is the micro-parameters of the energy transfer, which is described as,

$$C_{D-D/A}^{dd} = P_{D-D/A}^{dd} \times R^6 , \tag{2.24}$$

$$C_{D-D/A}^{dq} = P_{D-D/A}^{dq} \times R^8 , \tag{2.25}$$

$$C_{D-D/A}^{qq} = P_{D-D/A}^{qq} \times R^{10} . \tag{2.26}$$

2.7.3 Non-resonant energy transfer

Previous discussion is focused on the resonant energy transfer. But the cross-relaxation energy transfer between Tm^{3+} ions is not exactly the resonant energy transfer as the Dexter and Kushida models described. For non-resonant energy transfer, effect of

phonons should be considered. In the cross relaxation energy transfer between Tm^{3+} irons, because the transitions of $^3H_4 \rightarrow {}^3F_4$ and $^3F_4 \rightarrow {}^3H_6$ require different energy, phonons are necessary to be generated or absorbed to bridge the energy gap between the two transitions (see Fig. 2.14).

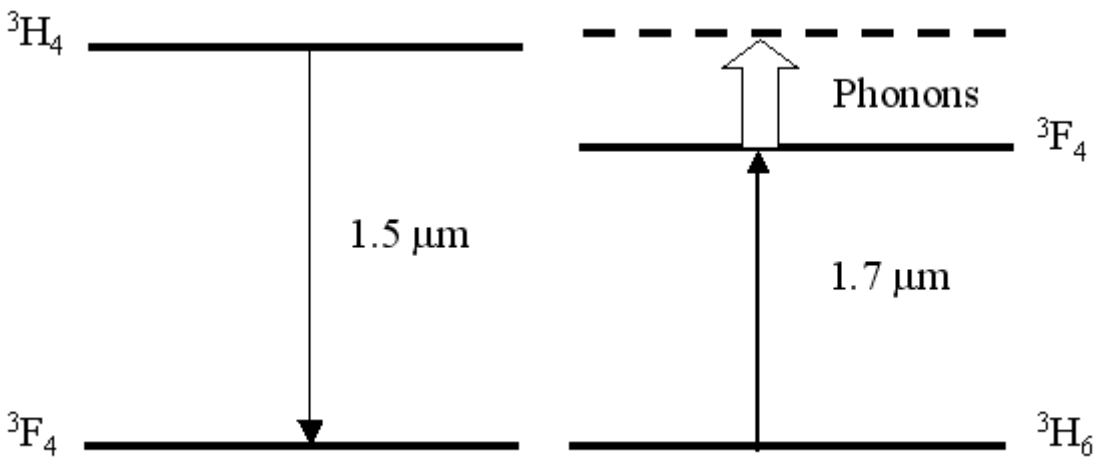

Fig. 2.14 Non-resonant cross relaxation energy transfer

Miyakawa and Dexter derived that phonon-assisted energy transfer rate had an exponential dependence on the energy gap of different transition [2.23]. It can be written as:

$$W_{PAET}(\Delta E) = W_{ET}(\Delta E = 0)e^{-\beta \Delta E}, \tag{2.27}$$

$$\beta = \alpha - \gamma, \tag{2.28}$$

$$\alpha = \frac{1}{\hbar\omega}\left\{\ln\left[\frac{N_i}{g_s(n+1)}\right] - 1\right\}, \tag{2.29}$$

$$\gamma = \frac{1}{\hbar\omega}\ln\left(1+\frac{g_s}{g_a}\right), \tag{2.30}$$

where W_{PAET} is the phonon assisted energy transfer rate, W_{ET} is the resonant energy transfer rate, $\hbar\omega$ is the phonon cut-off frequency of the host glass. Weber demonstrated that the highest-energy phonon in the glass host played the most important role in multi-phonon relaxation, because the relaxation rate was determined predominantly by the number of phonons involved in relaxation. N_i is the number of phonons involved in the phonon-assisted energy transfer. g_s and g_a is the electron-phonon coupling efficiency of sensitizer and accepter ions. n is the Bose-Einstein distribution of phonon occupation number,

$$n = \frac{1}{e^{\hbar\omega/kT}-1} \quad . \tag{2.31}$$

As discussed before, $(n+1)^{N_i}$ needs to be multiplied to relaxation rate equation to identify the multi-phonon process according to the perturbation theory. As a result, for phonon-emitting energy transfer,

$$W_{PAET} = W_{ET}(\Delta E = 0)e^{-\beta\Delta E}(n+1)^{N_i} \, . \tag{2.32}$$

For phonon-absorbed energy transfer,

$$W_{PAET} = W_{ET}(\Delta E = 0)e^{-\beta\Delta E}(n)^{N_i} \, . \tag{2.33}$$

Because room temperature leads to $(n+1)>>n$, phonon-emitting energy transfer dominates the phonon-assisted energy transfer. Therefore the reverse cross-relaxation energy transfer ($^3F_4$, $^3F_4 \rightarrow {}^3H_4$, $^3H_6$) is neglected in our model. However, its effect should be counted when the doping concentration is so high that the reverse energy transfer rate

is comparable with other transition rates, such as spontaneous emission rate and multi-phonon relaxation rate. As shown by equations (2.31, 2.32, 2.33), the ratio between reverse energy transfer and cross-relaxation energy transfer also increases with the raise of temperature.

In our study Kushida Model is used to calculate the transfer probabilities of donor-donor and donor-acceptor transfer. Dexter's phonon-assisted energy transfer model is applied to calculate the probability of donor-acceptor energy transfer. The cut-off phonon frequency of the glass is measured as 929 cm^{-1}, which is associated with the WO^{3-} group in the glass matrix. For donor-acceptor transfer, energy difference between the emission peak of $^3H_4 \rightarrow {}^3F_4$ transition and the absorption peak of $^3F_4 \rightarrow {}^3H_6$ transition is 920 cm^{-1}. Therefore, only one phonon needs to be generated to accomplish the phonon-assisted energy transfer ($^3H_4$, $^3H_6 \rightarrow {}^3F_4$, $^3F_4$). For energy migration of ($^3H_4$, $^3H_6 \rightarrow {}^3H_6$, $^3H_4$), which is a resonant energy transfer, only Kushida model is used to calculate the transfer probability of the donor-donor energy transfer. The micro-parameters calculated by the above models, are submitted into the hopping model to get the energy transfer rate W_{ET}, which is used in the macroscopic rate equations. All the micro-and macro-parameters of the energy transfer are also listed in Table II.

2.7.4 Rate equations

To explore the effects of multi-polar coupling on the cross-relaxation energy transfer, steady state rate equations are analyzed to determine the ratio of the fluorescence intensities of two different transition bands, which can be compared with the

experimental results. Because the energy gap between $^3H_5$ and $^3F_4$ of Tm^{3+} is so small, the nonradiative relaxation between those two levels becomes so dominant that most Tm^{3+} ions at $^3H_5$ rapidly decay to $^3F_4$ level by multi-phonon relaxation. To simplify the simulation and rate equations, a three level system, instead of a four levels system, is employed in our model. In the three level model assumption, all the Tm^{3+} ions at $^3H_5$ level decay to the $^3F_4$ state through multi-phonon relaxation immediately, leaving no Tm^{3+} ions at $^3H_5$ level. Following are the simplified stead state rate equations used for the simulation:

$$0 = -W_{03}n_0 + A_{30}n_3 + (A_{10} + A_{10nr})n_1 - W_{ET}n_3n_0 \quad (2.34)$$

$$0 = (A_{31}^* + A_{31nr})n_3 + 2W_{ET}n_3n_0 - A_{10}n_1 \quad (2.35)$$

$$0 = W_{03}n_0 - (A_{30} + A_{31}^* + A_{31nr})n_3 - W_{ET}n_3n_0 \quad (2.36)$$

$$A_{31}^* = A_{31} + A_{32} + A_{32nr} \quad (2.37)$$

$$n_{tot} = n_0 + n_1 + n_3 \quad (2.38)$$

where n_0, n_1, n_3 are the population densities of the ions at $^3H_6$, $^3F_4$ and $^3H_4$ states respectively under steady-state situation. A_{ij} is the radiative decay rate of transitions from level *i* to level *j*. A_{ijnr} is the nonradiative decay rate of transition from level *i* to level *j*. W_{03} is the pumping rate. W_{ET} is the energy transfer rate, calculated based on hopping model. All radiative decay rates are obtained by J-O theory and absorption spectrum. The non-radiative decay rates of $^3F_4$ state with different doping concentrations were calculated by equation (2.14) so as to include the quench effect of samples with different doping concentrations. Residual water in the glass is the major cause of the quenching of

$^3F_4$ whose absorption band happens to overlap with that of OH^- ion. Spontaneous emission rate of $^3H_4$ state is almost 6 times as high as that of $^3F_4$ state, which also means quenching has less impact on $^3H_4$ state than on $^3F_4$ state. Therefore, quenching caused by water is much more serious for $^3F_4$ than for $^3H_4$ state. For $^3H_4$ state, cross-relaxation energy transfer instead of concentration quenching is the main reason to make the lifetime of $^3H_4$ drop dramatically. So nonradiative decay rate of $^3H_4$ cannot be easily obtained from equation (2.14), especially for those samples with high doping concentrations. In our study, nonradiative decay rate of $^3H_4$ level with low doping concentration sample is used as the nonradiative decay rate for all samples with different doping concentrations.

Population densities of $^3H_4$ and $^3F_4$ in steady state condition were obtained by solving the above equations. Obviously that,

$$\eta = \frac{A_{10} \times n_1 \times h\nu_{10}}{A_{31} \times n_3 \times h\nu_{31}}, \tag{2.34}$$

shows the theoretical value of the ratio of the emission intensities of two different transition bands, where ν_{10} and ν_{31} are the frequencies of the transitions of $^3F_4 \rightarrow {}^3H_6$ and $^3H_4 \rightarrow {}^3F_4$ respectively; h is the Planck constant; n_i is the stead state population of level i.

2.7.5 Simulation and experiment results

Fig. 2.15 shows the normalized emission spectra of the tellurite glass with different doping concentrations. The spectra are normalized at the peak of 1.8 μm transition band. Fig. 2.16 shows the simulation results of η derived from different models, such as dipole-dipole interaction only (dd), dipole-dipole plus dipole-quadruple interactions (dd+dq), and dipole-dipole plus dipole-quadruple plus quadruple-quadruple interactions (dd+dq+qq). The intensities of emission transitions are determined by the integral of the whole emission spectrum band. The experiment results of η are also shown in the Fig. 2.16 for comparisons.

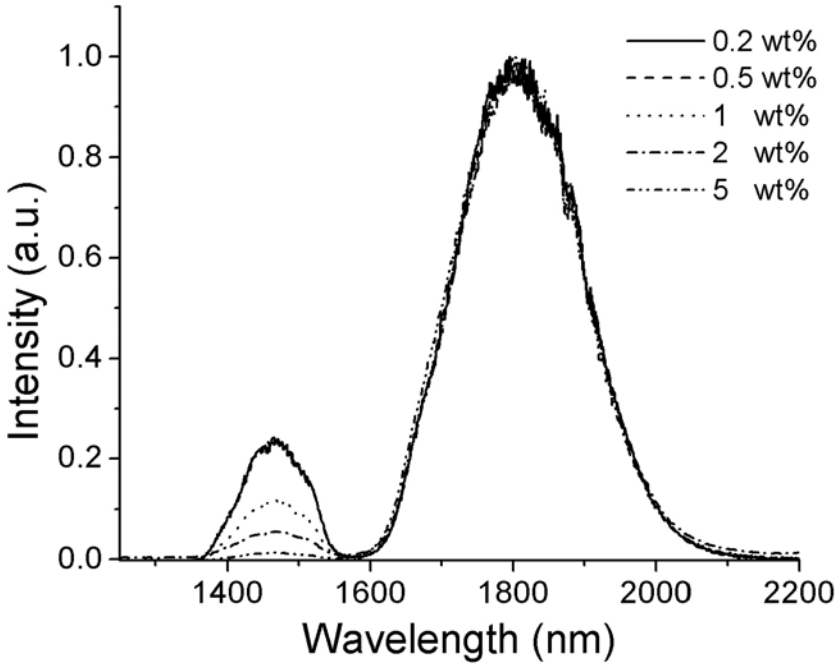

Fig. 2.15 emission spectrum of samples with different doping concentrations

We can see that only the dd+dq model provides the best match to the experimental results. For low concentration all the simulation results of 3 models have the same values, because the distance between Thulium ions is too far away to make energy transfer occur. At high concentration region, where the energy transfer occurs, the three models give different preditions. While dd+dq model fits the experiment results well, dd and dd+dq+qq models give either too smaller or too bigger values than the experimental data. It is worth noting that when the doping concentration is as high as 5%, the simulation result of dd+dq model is slightly higher than the experiment result. One reason is that we did not include the reverse energy transfer in the model of simulation. When the doping concentration is high enough, distance between excited Tm^{3+} at $^3F_4$ state is too close to avoid the reverse energy transfer ($^3F_4$, $^3F_4 \rightarrow {}^3H_4$, $^3H_6$), which makes two excited Tm^{3+} ions at $^3F_4$ state become one excited Tm^{3+} ion at $^3H_4$ state while another Tm^{3+} ion stay at ground state. When the reverse energy transfer rate becomes large enough to be comparable with other radiative and nonradiative rates, its effect will be seen from the experiments. This reverse energy transfer will decrease the pump efficiency.

experiments. This reverse energy transfer will decrease the pump efficiency.

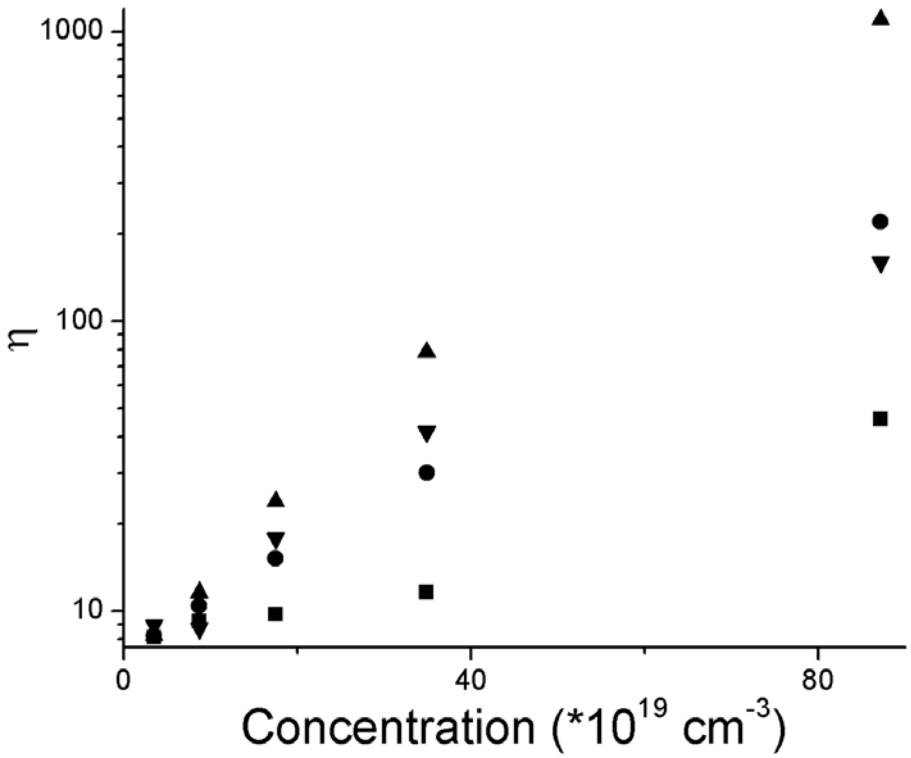

Fig. 2.16 η Vs ConcentrationDown triangle is the experiment value; up-triangle is the simulation value of dd+dq+qq model; round spot is the simulation value of the dd+dq model and square is the simulation results of the dd model.

Although high doping concentration can increase the pump efficiency by cross-relaxation energy transfer, it can also reduce the population of $^3F_4$ state by reverse energy transfer. In addition, the cluster-caused quenching results from high concentration will lead to unbleachable loss because of the high intra-cluster transfer rate. There will be an optimum concentration of Tm_2O_3 for different hosting materials and different applications. Since the ratio of cross-relaxation energy transfer and reverse energy

transfer is proportional to the value of (n+1)/n, cooling the glass host is another way to decrease the probability of the reverse energy transfer.

2.8 Summary

Thulium doped tungsten tellurite glass ($0.6TeO_2$-$0.25WO_3$-$0.075K_2O$-$0.075Li_2O$) has been fabricated. The Spectroscopy study of thulium doped tellurite glass and the theoretical discussion on cross relaxation energy transfer have been investigated. The results obtained are summarized as follows:

Absorption cross-section for ground state transitions of Tm^{3+} in the near infrared and visible region is obtained from absorption spectrum of bulk glass sample at room temperature. Judd-Ofelt theory is applied to absorption cross-section spectrum; the Judd-Ofelt intensity parameters are determined through least linear fitting. Compared with other glass samples, Tm-doped tellurite glass possess a large value of Ω_2, which usually leads to a big stark split. All the radiative transition probabilities and branch ration have been calculated upon J-O theory.

Emission spectra of glass samples in near infrared region have been measured under an excitation of Ti:sapphire laser at 793 nm. The decline of emission intensity of 1.5-μm transition is found with the increase of doping concentrations. The emission cross-section of the transition $^3F_4 \rightarrow {}^3H_6$ has been evaluated by Fuchtbauer-ladenburg equation. Fluorescence decays of both 1.5 mm and 1.8 mm transitions have been measured. The radiative lifetime of $^3H_4$ state drops from 181 ms to 9 ms when the doping concentration is

increased from 0.2 wt% to 5 wt%. Nonradiative decay rates of different states are obtained by comparing the radiative and nonradiative lifetime.

A self-calibrating fluorescence spectroscopy technique is used to study the cross-relaxation energy transfer and energy migration between the Tm^{3+} Ions doped in the tellurite glass. Ab-initio calculation is used to evaluate the energy transfer process. Fluorescence decay measurement, Judd-Oflet theory, Kushida model, phonon assisted energy transfer model and hopping model are employed to determine the micro and macro-parameters of the energy transfer and migration. Steady rate equation analysis is used to simulate intensity ratio of the two dominant emission bands. Simulation result of dipole-quadrupole models fits experiment results well. We find that the combination of dipole-quadrupole and dipole-dipole interaction is the dominant mechanism in the energy transfer of Thulium ions.

As a result, it can be concluded that highly Tm^{3+} doped TeO_2–WO_3 glasses are promising materials for 2 ㎛ lasers with a considerable high efficiency.

CHAPTER 3 TM-DOPED TELLURITE GLASS MICROSPHERE LASER

3.1 Introduction

Microcavity, with its unique spatial confinement and the capability of energy storage has found a variety of applications in chemical sensing [3.1], quantum electrodynamics [3.2], lasers [3.3] and nonlinear optics [3.4]. Microcavities made of various materials have been reported, such as liquid droplet [3.5], glass microsphere [3.6], semiconductor microdisk [3.7], polymer microring [3.8], and asymmetric fiber [3.9]. Among them, glass microsphere has shown a highest Q value due to the perfect spherical shape cast by surface tension of the glass during the melting process [3.10]; Q values of 10^{10} was reported in silica microspheres. Microspheres are easy for manufacture and handle, as well.

However, the high Q values of microspheres also lead to the difficulty of coupling light into and out of microspheres. Several methods have been developed and demonstrated to launch light into microspheres, such as focused free beam, prism coupling [3.11], fiber taper [3.12], and angle-polished fiber coupler [3.13]. Most of them use the evanescent wave coupling based on guided mode coupling theory.

Microsphere lasers emitting with various wavelengths have been demonstrated in different rare-earth doped microspheres. Thulium provides an emission band at 1470 nm which covers the s-band of optical-communication, and a broad emission band from 1800 to 2200 nm which could be used in sensing, lidar, military, and medical applications. As disscuessed in Chapter 2, tellurite glass is a good host material for Tm-doped solid-state

lasers. In addition, the high refractive index (1.98) of tellurite glass also helps to confine the light propagating inside the microsphere. In this chapter, we report Tm^{3+} doped tellurite glass microsphere laser emitting around 2 μm and 1.5 μm.

3.2 Microsphere preparation

A common method to fabricate microsphere is to melt the tip of a fiber with a high power (e.g. CO2) laser, or an oxygen-hydrogen torch. Then surface tension creates a spherical volume with usually rather low deformation. Such a technique requires an expensive set-up and produces a quite low yield.

In our lab, microspheres are produced by spin-molding method. As described in Chapter 2, Tm-doped tellurite glass was prepared in a nitrogen atmosphere to avoid inclusion of water, which was recognized as a major source of fluorescence quenching. Microspheres are fabricated by pouring the melted glass onto a spinning plate, as shown in Fig. 3.1. The fluid Tm-doped tellurite glass is broken into droplets by centrifugence and gets cooled in the air. Therefore microspheres are formed by surface tension. The diameter of the microsphere ranges from 10 μm to 100 μm. In our experiment the microsphere with a diameter around 20 μm shows a better circular surface with low deformation.

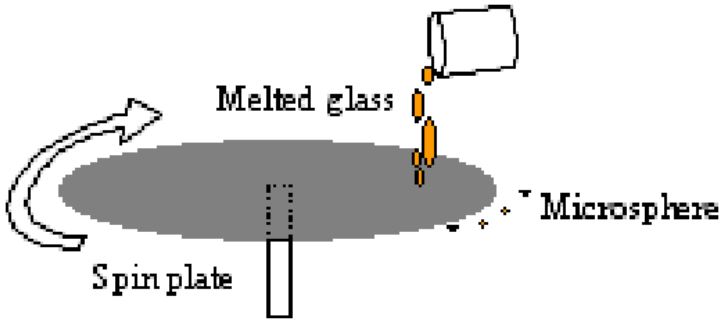

Fig. 3.1 Setup for fabrication of microsphere

3.3 Whispering gallery modes of microsphere

Whispering-gallery modes (WG modes) were first studied by Lord Rayleigh trying to understand the acoustic waves clinging to the dome of St. Paul's Cathedral, and the waves were shown to be trapped between the cylindrical boundaries.

In optics, Whispering gallery modes occur at particular resonant wavelengths of light for a given dielectric media of micro cavities. At these wavelengths, the light undergoes total internal reflection at the particle surface and becomes trapped within the particle for timescales of the order of nanoseconds.

In the point view of ray optics, WG modes are the modes of light that is trapped inside the dielectric sphere by continuous total internal reflections at the curved boundary of surface. WG modes occur at discrete frequencies that make the light remain the same phase after a round trip of the microsphere.

Three dimension vector Helmholtz equation has been used to analyze the modes of light propagating inside the microsphere. One approach to simplify the problem is to

assume that optical resonances may be approximated by the whispering gallery modes which are obtained by applying the boundary condition,

$$\Psi_{in}(\vec{r},\theta,\varphi) = \Psi_{in}(R,\theta,\varphi) = 0\,, \tag{3.1}$$

where R is the radius of the microsphere. Under this situation, WG modes are identified in terms of three mode numbers representing radial (n), azimuthal (l), and polar field dependency (m). The radial part of a WGM can be described by spherical Bessel functions, while the polar field dependency follows spherical harmonics. The azimuthal field variation is sinusoidal [3.14],

$$\vec{E}^{TE}_{n,l,m}(r,\theta,\varphi) = E_0 n j_l(nk_0 r)\vec{Y}^m_l(\theta,\varphi) \tag{3.2}$$

$$\vec{E}^{TM}_{n,l,m}(r,\theta,\varphi) = \frac{E_0}{n^2}\left(\frac{n}{k_0} j_l(nk_0 r)\vec{Y}^m_l(\theta,\varphi) + \sqrt{l(l+1)}\,\frac{n}{k_0 r}\vec{Y}^m_l(\theta,\varphi)\right. \tag{3.3}$$

Eq. (3.20) and (3.3) are for TE and Tm modes respectively. Mode number n is equal to the number of field maxima in the direction along the radius of the sphere. The value of l is close to the number of wavelengths that fit into the optical length of the equator. The value l - m + 1 is equal to the number of field maxima in the polar direction, ie. perpendicular to the equatorial plane. The fundamental mode is defined as n = 1 and m = l. The resonant wavelength is determined by the values of n and l.

3.4 Tapered-fiber

According to coupled mode theory [3.15], it is necessary to utilize overlapping of the evanescent field of the whispering gallery modes with the evanescent field of a phase-matched optical waveguide to couple the guided modes. Tapered fiber is one of the methods to get expanded evanescent wave.

Tapered fiber coupling method first reported by Ming Cai [3.12] in 2000. In our experiment, a pump delivery fiber was tapered down to a few micrometer using the typical heat-and-stretch method. The core-cladding structure vanishes at the thinnest part and the waveguide is similar to a glass rod in the air. As is known, Bessel function of the first kind describes the light filed inside a step-index circular waveguide. And the evanescent wave that outside of the fiber can be evaluated by a modified Bessel function of the second order,

$$K_\nu(\gamma r) \approx \frac{e^{-\gamma r}}{\sqrt{2\pi\gamma r}} \qquad [3.4]$$

$$\gamma^2 = \beta^2 - k_0^2 n_{air} \qquad [3.5]$$

where ν is the mode number, β is the propagation constant, n_{air} is the refractive index of air, r is the distance from the fiber. Thin fiber leads to small fundamental propagation constant that results in a small value of γ. Therefore, Equation (3.4) and (3.5) clearly show that the thinner the waist of fiber taper, the larger evanescent mode fields it can reach. In addition, the waist of fiber also needs to be small enough to only support fundemental mode due to the big refractive index difference between fiber and the air. The cutoff diameter of the fiber waist for single mode propagation of laser at 2 μm is 1.43

mm. The steep change of the fiber taper needs to be avoided in order to reduce the propagation loss. In out experiment the propagation loss of fiber taper can be controlled under 1.5 dB.

3.5 Microsphere laser setup and performance

As we discussed in Charpter 2, high doping concentration of thulium oxide in the glass helps to improve the pumping efficiency of laser transition of $^3F_4 \rightarrow {}^3H_6$ due to the cross relaxation energy transfer. The emission spectra and fluorescence decay measurement of Tm-doped tellurite glass samples with different doping concentrations also confirm that. In order to achieve high pump efficiency , 5 wt% Tm-doped tellurite glass is chosen to make glass microsphere for 2-mm laser demonstration.

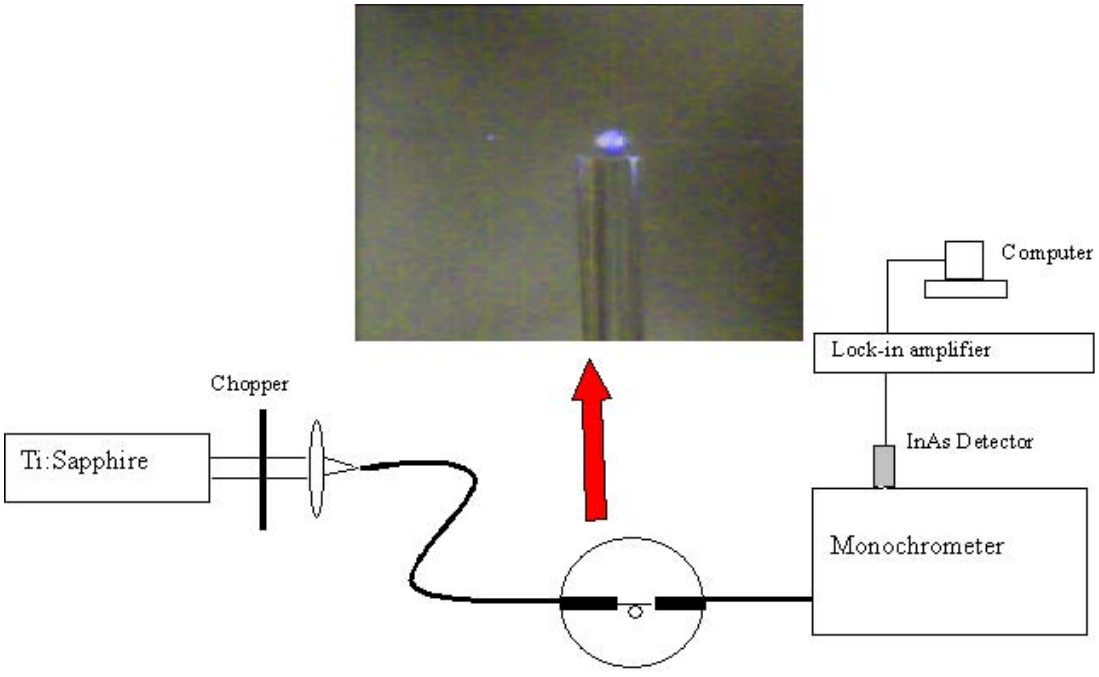

Fig. 3.2 Experiment setup for microsphere laser

The microsphere laser setup is shown in Fig 3.2. The tapered fiber is placed in touch with the equator of the microsphere. The optical field of the pump laser from the fiber tunnels into the microsphere through evanescent coupling. Another fiber is used to hold the microsphere and mounted on a 5-D stage. The holding fiber only touches the polar area of the microsphere to avoid disturbing the refractive index distribution of the modes at the coupling area around the equator. Because the pump delivery fiber used in experiment is a piece of Corning SMF-28 that is multimode fiber at the pumping wavelength (794 nm from a Ti-sapphire laser), a large portion of pump power leaks out of the tapered fiber at the thinnest part of the tape that only support the fundamental mode. By adjusting the relative positions and the distance between the microsphere and the fiber taper, spontaneous emission of thulium in whispering-gallery-modes at 2 μm region is observed from the 5 wt% Tm-doped tellurite glass microsphere. The whispering gallery modes is shown in Fig. 3.3 . Radius of microsphere can be estimated from the output spectra of the laser by,

$$R = \frac{\lambda^2}{2\pi n \Delta\lambda}, \tag{3.6}$$

where R is the radius of the microsphere, λ is the wavelength, n is the refractive index. Δλ is the free spectral range, which is measured as 21 nm. The diameter of the microsphere used in this letter is 25 μm, which is very close to the observed value under microscope.

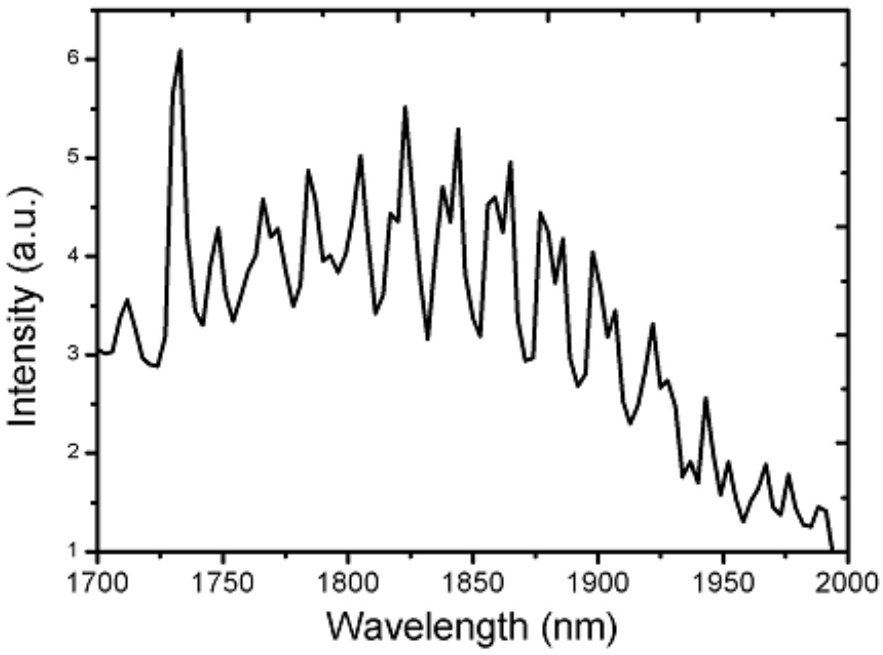

Fig. 3.3 Whispering gallery modes of Tm-doped tellurite glass microsphere

Microsphere laser at 2 μm is achieved when the pumping power is increased. The output power of the microsphere laser versus pumping power is shown in Fig. 3.4. The pump power was estimated at the center of fiber taper. A scanning Fabry-Perot cavity is employed to measure the laser full width half maximum (FWHM) Δν that is 115MHz.

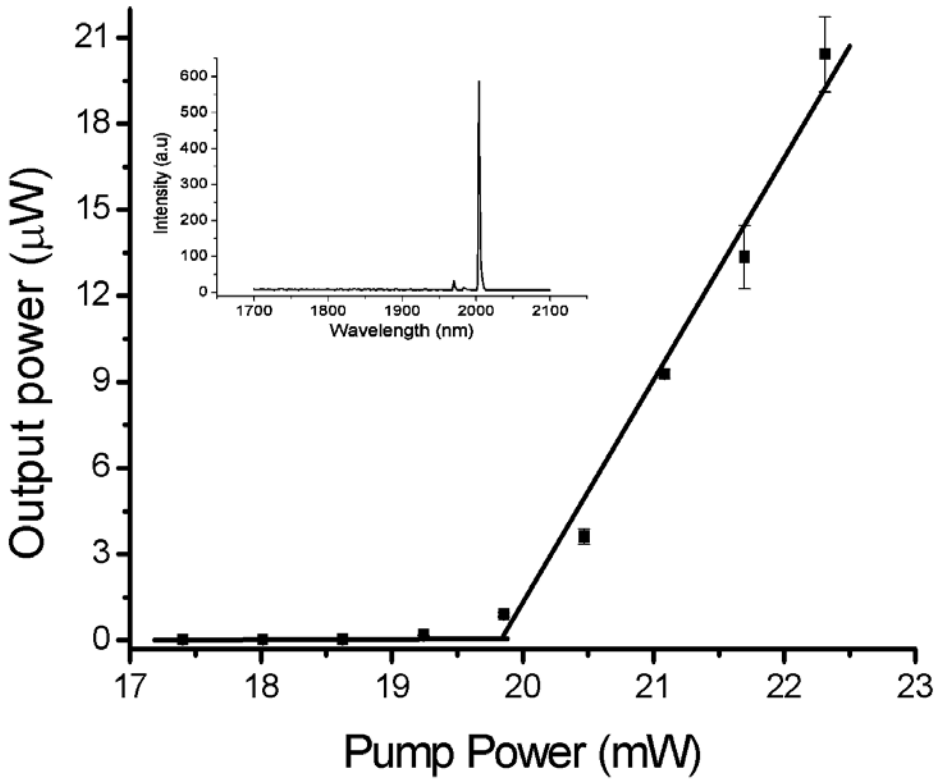

Fig. 3.4 The power curve of the laser output. Inset is the spectrum of the thulium doped tellurite glass microsphere.

The laser spectrum with emission spectrum of laser transition is shown in Fig. 3.5. The lasing wavelength of the microsphere is at 2 μm that is shifted by 200 nm from the emission peak at 1800 nm of the transition ($^3F_4$->$^3H_6$). The red shift of microsphere laser wavelength is caused by the reabsorption from ground state thulium. The 2-mm laser transition of thulium is a 3-level system, in which the re-absorption of the un-pumped ions in the laser propagation area forces the laser spectrum to shift to longer wavelengths.

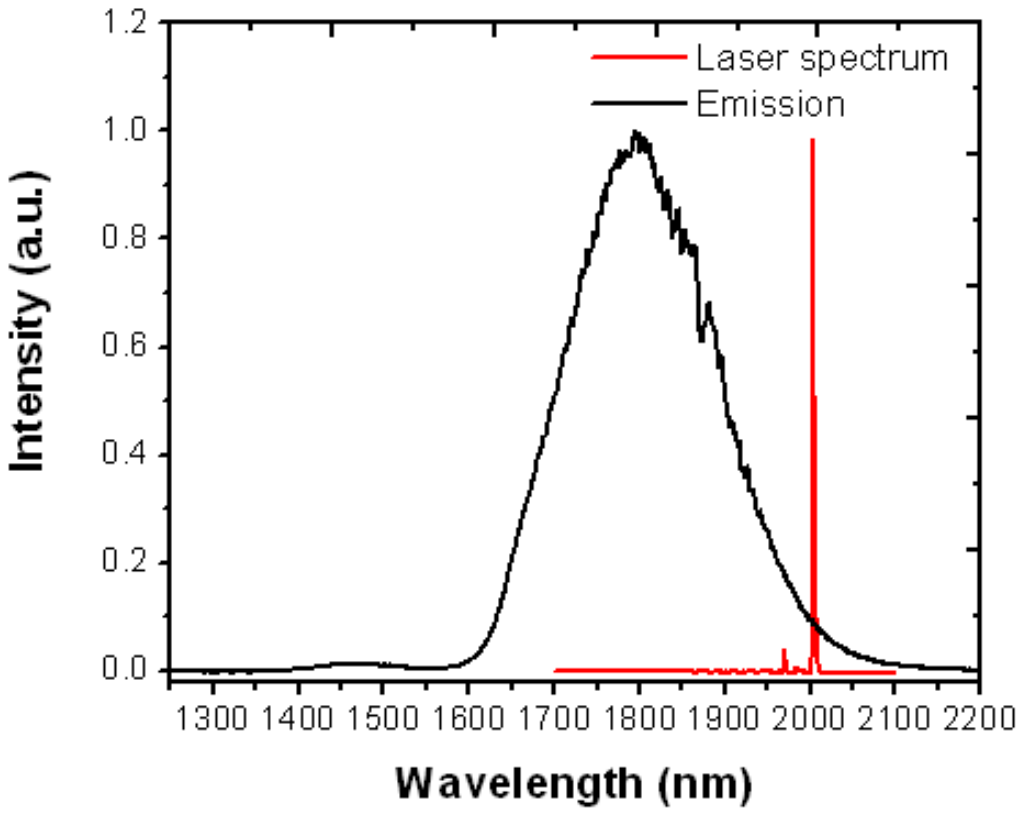

Fig. 3.5 Laser spectrum of 5 wt% Tm-doped tellurite microsphere

The re-absorption in the Tm^{3+}- doped microsphere laser results from two factors. First one is that the pumping wavelength is not exactly at the resonant wavelength of whispering-gallery mode of the microsphere. It means that the coupling of pump laser between tapered fiber and microsphere is not efficient. Hence pumping efficiency does not reach its maximum. The low pumping efficiency results in some Tm^{3+} ions to remain unpumped. Increasing the pumping power and carefully selecting the pump wavelength that is resonant in the microsphere will help increasing the pumping efficiency. The second factor, which we consider to be the major one, is that the mode distribution of the

793 nm pump light and 2 ㎜ signal light do not match exactly. Part of the signal laser mode that propagates in the unpumped region due to the mode-mismatch leads to re-absorption which is responsible for the red shift of the laser wavelength.

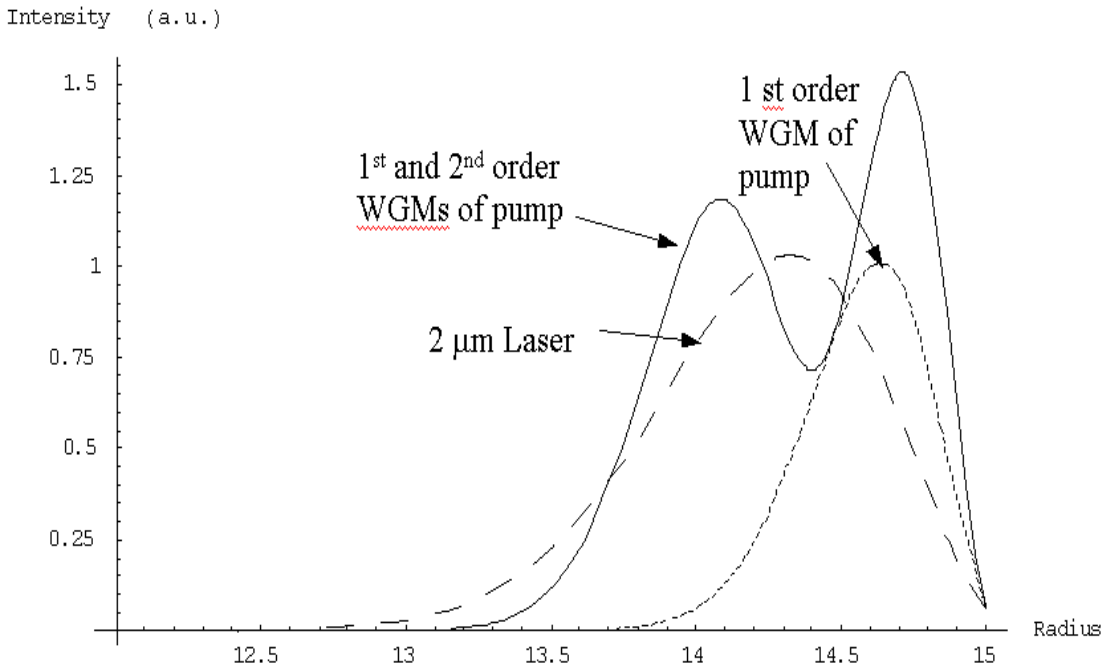

Fig. 3.6 The radial distribution of the Whispering-gallery modes of different wavelengths.The radius of the microsphere is 15 μm, (Dash line: 2 μm laser; Dot line: first order WGM of pump laser; Solid line: fist and second order WGMs of pump laser) .

To check this hypothesis, we performed a calculation of the mode distribution of the pump and signal light in the microsphere laser. As is known, the radial distribution of the whispering-gallery modes can be described by spherical Bessel function. To simplify the

calculation, we chose the TE mode of the fundamental Whispering-Gallery mode (n=1) for analysis. The radial distribution of the electrical field of inner microsphere is described as,

$$E(r) = j_l(n(\lambda)k_0 r), \tag{3.7}$$

where j_l is the spherical Bessel function, n is the refractive index, k_0 is the vacuum wave number of the light, r is the radius of the microsphere. Fig. 3.6 shows the calculated radial distribution of the low order Whispering-Gallery modes for both pump and the signal laser. It is obvious that the first order WGMs of pump and signal light do not overlap in the radial direction inside the microsphere. Signal light covers more mode volume than the pumping laser does. If the dispersion of material is considered, the difference in mode volume will be even larger. Therefore, the signal laser propagating around microsphere always has its tail in the area where the Tm^{3+} ions are not excited by pumping laser. That radial modes mismatch between the pump and signal laser is the main reason accounting for the red shift of laser wavelength. The red shift of microsphere laser was also observed in other similar experiments [3.12, 3.16]. In Yang's experiment [3.17] whose active material was a layer of coating around the passive glass microsphere, the laser wavelength was at emission peak. This is due to the fact that the active layer is so thin that rare-earth ions only stay in the area where both pumping and signal laser can cover. Fig. 3.6 also shows that the sum of first and second order Whispering-gallery modes of the pumping laser overlaps well with the first order mode of signal laser, which means the problem of the red-shift of signal laser can be solved if both the first and second radial modes of the WGMs of the pumping laser are excited in

the microsphere. In order to achieve that, the tapered fiber should possess the capability of carrying high order modes of the pump laser. The red shift caused by re-absorption also indicates the possibility of potential microsphere sensing by using the evanescent wave tail that stays outside of the microsphere. One feature of microsphere sensor is its extreme high sensitivity due to the high Q value that trap light inside of the microsphere and keep the light interacting with sensing material. Other advantages of microsphere sensor come from its tiny size and low cost for fabrication.

3.6 S-band microsphere Laser

The requirement of carrying higher bit-rate through one commercial silica fiber which has a broad low-loss band (1450-1650 nm < 0.25 dB/Km) has drawn great attention of researches to thulium oxide doped material whose $^3H_4$->$^3F_4$ transition of Tm^{3+} at 1.5 μm covers the S-band of optical communication. However, such transition is a self-terminating transition whose lower level lifetime is significantly longer than its upper level lifetime. Under such situation, ions of active material will accumulate in the lower laser level due to its longer lifetime, which will stop the buildup of population inversion of laser transition. The difficulty of building up population inversion prevents the 1.5-mm transition from lasing.

To improve lasing or amplifier performance of self-terminating transition, one then has to find mechanisms to depopulate the lower laser level. Several special techniques

have been developed to depopulate the lower level of the transition at 1.5μm. Some trivalent rare-earth ions, such as Ho^{3+}, Tb^{3+}, and Nd^{3+}, were co-doped with Tm^{3+} to reduce the population of the long-lived $^3F_4$ state [3.18-20] through resonant energy transfer process. Some studies, in order to achieve population inversion, used dual-wavelength pump to empty the $^3F_4$ state by exciting ions at $^3F_4$ state to a high energy level [3.21]. We successfully demonstrated the 1.5μm laser on the self-terminating transition in a microsphere resonator through a cooperative lasing process.

Tellurite glass is an attractive host for thulium ions due to its low phonon energy that helps Tm^{3+} stay at the upper level ($^3H_4$) of the $^3H_4$->$^3F_4$ transition by reducing the multi-phonon decay rate from $^3H_4$ to $^3H_5$. Tellurite glass samples of different concentrations were fabricated and characterized to choose the optimum concentration for the 1.5 μm microsphere laser. As we discuused in Charpter 2, when concentration is larger than 0.5wt%, the lifetime of $^3H_4$ state drop from 180 μs to 122 μs or less, due to cross relaxation energy transfer. The emission spectrum also shows that when the doping concentration is higher than 0.5 wt%, the intensity ratio between 1.8 μm transition and 1.5 μm transition increases nonlinearly [3.22]. Therefore thulium doping concentration of 0.5 wt% is chosen in the experiment in order to eliminate the cross-relaxation energy transfer between thulium ions and to achieve efficient pump absorption.

3.6.1 Lasing condition for self-terminating transition

The condition for CW lasing on a self-terminating transition (level 3 -> level 1) was described by [3.23],

$$A_1 > A_{31}^*, \tag{3.8}$$

where in the case of thulium, level 1, 2, and 3 represent $^3F_4$, $^3H_5$, and$^3H_4$ states. A_1 is the sum of spontaneous emission rate and nonradiative decay rate of the state $^3F_4$, lower level of laser transition, and A_{31}^* is the total decay rate from state $^3H_4$ to state $^3F_4$. The criterion derived under the condition that no stimulated emission and stimulated absorption were considered in the steady state rate equations. It states that in order to get population inversion, the requirement for CW lasing, the total decay rate of the lower level of laser transition should be greater than the total relaxation rate from the upper level to the lower level.

In the case of Tm^{3+} doped in tellurite glass , the calculated spontaneous emission rates are A_{10}=540 s^{-1}, A_{32}=98 s^{-1}, A_{31}=260.5 s^{-1}, A_{30}=2863 s^{-1}, where the subscript number i represents the corresponding energy level shown in Fig. 1.2. All ions reaching the $^3H_5$ state will decay to the $^3F_4$ state immediately through multiphonon relaxation, because $^3H_5$ and $^3F_4$ states are so close in energy that only 2 or 3 phonons needs to be generated to accomplish the multi-phonon decay. Therefore, to simplify the analysis, a 3-level model in which the population of $^3H_5$ is zero is adopted. The total decay rate from $^3H_4$ state to $^3F_4$ state (A_{31}^*) can be written as,

$$A_{31}^* = A_{31} + A_{32} + A_{31nr} + A_{32nr}\,, \tag{3.9}$$

where A_{ijnr} and A_{ij} are the nonradiative and radiative decay rate from level i to level j respectively.

For Tm^{3+} doped in the material with low phonon energy, the inequality (3.8) is satisfied. For example, 1.5 μm cascade laser of thulium ions has been demonstrated in fluoride glass [3.24, 3.25]. In that case, the threshold of 1.5 μm laser is lower than that of the 1.9 μm laser, because the upper lasing level ($^3H_4$) of the 1.5μm laser transition was directly excited by the pump laser, while the upper lasing level ($^3F_4$) of the 1.9 μm laser transition was populated by the ions relaxed from $^3H_4$. According to the above spontaneous emission rates of different transitions, only 11% of the population excited to $^3H_4$ state, upper level of 1.5-mm transition, reaches the $^3F_4$ state, the upper level of the 1.9 μm transition. Due to the low pump efficiency, the 1.9 μm transition starts to lase after 1.5 μm transition does.

In our experiment, the phonon energy of the tellurite glass was measured as 929cm^{-1} which is higher than that of the fluoride glass. The nonradiative decay rate A_{32nr} is 2302 s^{-1} calculated by $A_{32nr}=1/\tau_{meas}-(A_{31}+A_{32}+A_{30})$. Therefore, the inequality (3.8) is not satisfied. However, we found the population inversion of the upper transition can be reached by making the lower transition lase first, which will depopulate the lower level of the upper transition. Under such situation, the steady state rate equations then can be written as,

$$0 = W_{03}N_0 - A_{31}^{*}N_3 - A_{30}N_3 \tag{3.10}$$

$$0 = A_{31}^{*}N_3 - W_{10}N_1 + W_{01}N_0 \tag{3.11}$$

$$N_0 + N_1 + N_3 = N \tag{3.12}$$

where N_i is the population density of ions in level i, W_{10} and W_{01} are the stimulated emission rate and the stimulated absorption rate respectively. W_{03} is the pumping rate. Stimulated emission of 1.5-μm transition is not considered here, as we just need to find the condition for population inversion of the upper transition. Rate equations are solved for the population inversion ratio N_3/N_1. To simplify the result, only terms with the highest order of W_{03}, W_{01} or W_{10} is considered in both denominator and numerator, because usually the pumping rate, stimulated emission rate and stimulated absorption rate are much larger than the spontaneous emission rate. Therefore, the moderated condition for population inversion is,

$$\frac{N_3}{N_1} = \frac{W_{03} \times W_{10}}{(A_{30} + A_{31}^*) \times W_{01} + A_{31}^* \times W_{03}} > 1 \tag{3.13}$$

Inequality (3.9) states that if the pumping rate W_{03} and stimulated emission rate W_{10} are large enough, the population inversion of the upper transition will be built up. Furthermore, if the lower laser transition is a 4-level system, in which $W_{10} >> W_{01}$, the criterion can be simplified as $W_{10} > A_{31}^*$. It's quite similar to the inequality (3.8), except that A_{10} is replaced by W_{10}.

3.6.2 S-band microsphere laser performance

The microsphere laser setup is similar to the setup discussed in section 3.5. The power curves of both 1.5μm and 1.9μm laser are presented in Fig. 3.7. It's worth noted that the threshold of 1.9 μm laser is lower than that of the 1.5μm laser, which is the

opposite of the phenomenon observed in fluoride glass [3.24, 3.25]. The lower threshold of 1.9 mm laser clearly confirms the fact of cooperative lasing.

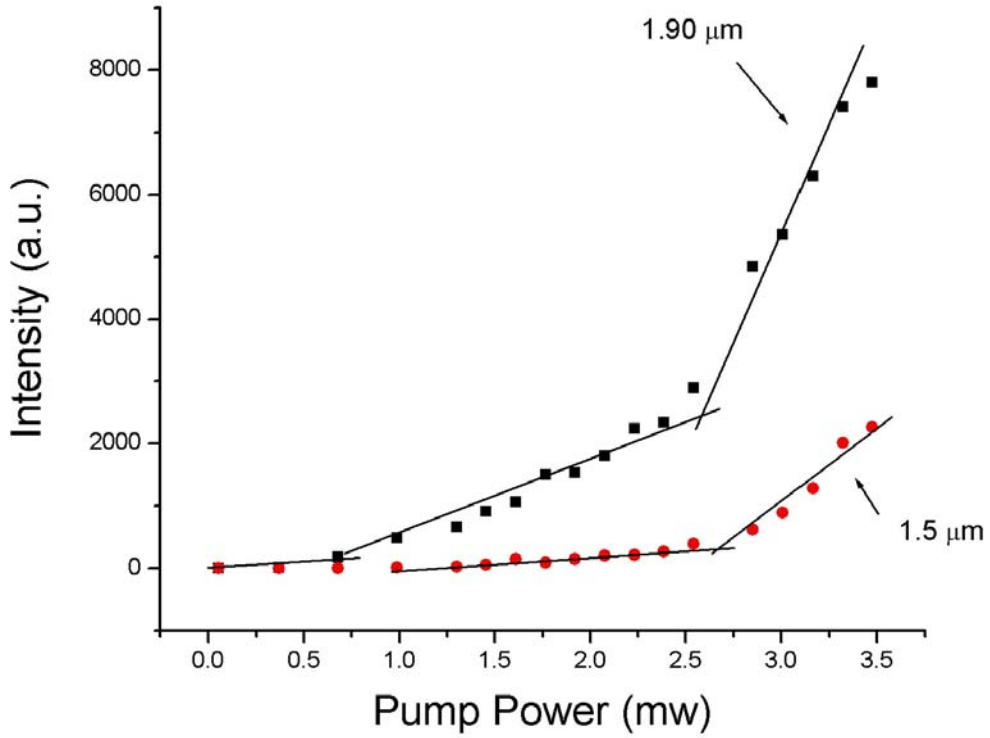

Fig.3.7 The slopes of both the 1.9 (black square) and 1.5 (red circle) μm lasers versus the pump power.

The stimulated emission rate is proportional to the laser photon flux. When the lower transition ($^3F_4 \rightarrow {}^3H_6$) starts to lase, its photon flux is not big enough to make the stimulated emission rate satisfy the inequality (3.9) of the upper transition laser ($^3H_4 \rightarrow {}^3F_4$). With the increase of pump and signal laser, the stimulated emission of 1.9-mm laser transition becomes large enough to dump the ions staying at $^3F_4$ state and to make the

inequality (3.9) satisfied. Hence the upper transition of 1.5-mm starts to lase. Careful inspection of Fig. 3.7 also shows that as soon as 1.5-μm transition start to lase, the slope of the l.9-μm laser is increased. The enhancement of 1.9-mm laser efficiency benefits from the high pumping efficiency that is caused by the large stimulated emission rate of upper laser transition. Under such condition, both quantum efficiencies of 1.5-mm and 1.9-mm laser transitions will be close to 1. In the experiment we also found that the intensity ratio between the upper transition laser and lower transition laser increased, when the lower transition laser operated at shorter wavelength at which the lower transition had bigger emission cross-section.

Fig. 3.8 shows the laser spectrum of microsphere. The emission spectrum of the glass sample with the same doping concentration is also illustrated in the inset of Fig. 3.8. The laser wavelengths are around 1.9 μm and 1.5 μm. Both are red shift from the emission peak of the respective transition bands. For 1.9 μm laser which is a 3-level system, the red shift of the laser wavelength results from the mode mismatch between pump and signal laser. The radial distribution of the whispering-gallery modes of pump and signal laser did not overlap well. Part of the 1.9 μm laser WG mode area is not covered by the pump laser. Therefore, the reabsorption from those unpumped thulium ions make the lower transition laser operate at long wavelength.

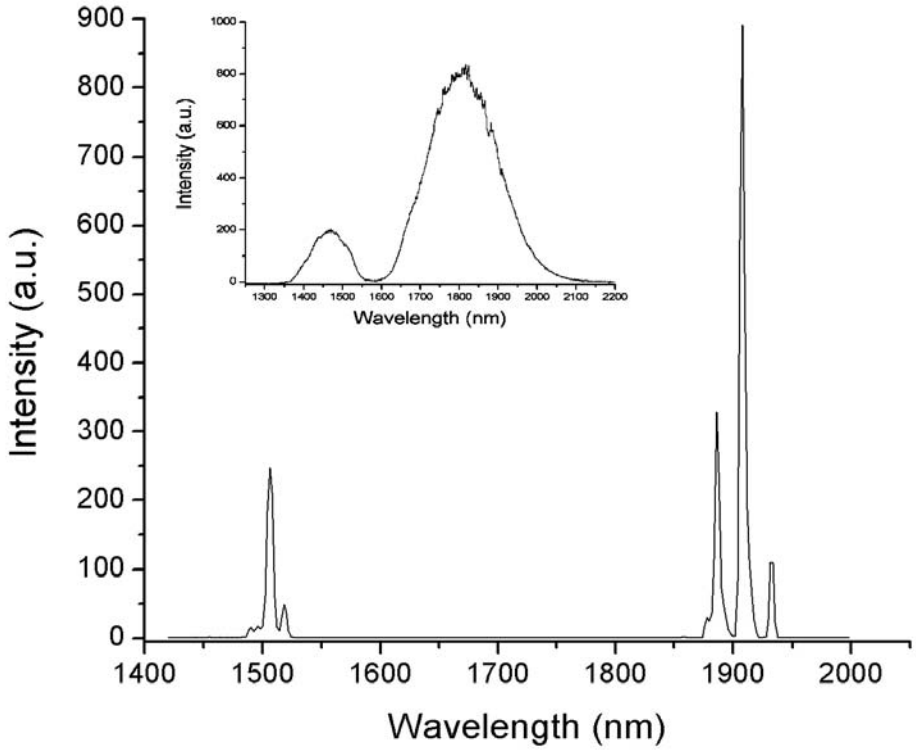

Fig. 3.8 The microsphere laser spectrum of the 1.9 and 1.5 μm. The emission spectrum of the 0.5 wt% thulium doped tellurite glass sample

For 1.5μm laser, the red shift is caused by the reabsorption from the thulium ions at the lower laser level ($^3F_4$). When the 1.9 μm laser is operating in steady state, there are certain thulium ions at the upper level ($^3F_4$) which is also the lower level of the 1.5 μm laser transition. The absorption from those ions at $^3F_4$ states will push the upper transition laser toward long wavelength.

3.7 Summary:

Single mode microsphere laser at 2 μm is demonstrated from highly thulium doped tellurite glass microsphere. Glass samples with various doping concentrations are fabricated and characterized to choose the material with highest pump efficiency. A taperd fiber is fabricated and utilized to couple the pump laser into the microsphere. Laser wavelength is red shifted from the emission peak of thulium ions at 1800 nm due to the different mode distribution inside the microsphere. Continuous-wave 1.5-μm-band laser originating from $^3H_4$->$^3F_4$ transition in thulium doped tellurite glass microsphere is demonstrated using 793-nm single wavelength pumping. 1.9-μm laser from the lower transition ($^3F_4$->$^3H_6$) of Tm^{3+} is generated to depopulate the lower level ($^3F_4$) of 1.5μm transition ($^3H_4$->$^3F_4$) in order to achieve the population inversion. Laser wavelength of $^3H_4$->$^3F_4$ transition is shifted by 30 nm from the emission peak. Slope efficiency of 1.9 μm laser is improved after the1.5 μm laser start to lase. Laser condition of a self-terminating transition has been studied.

CHAPTER 4 THULIUM DOPED GERMANATE FIBER LASER

4.1 Introduction

The boom of telecom has long gone, but some of the technological advances of that time bring the solid-state laser into a new stage: fiber laser. Fiber lasers are usually meant to be lasers with optical fibers as gain media, although some lasers with a semiconductor gain medium and a fiber cavity have also been called fiber lasers. In most cases, the gain medium is a fiber doped with rare-earth ions such as erbium, neodymium, ytterbium, or thulium, and one or several laser diodes are used for pumping. Both CW and pulse operations have been demonstrated in fiber lasers. Current Fiber laser development appears to fall into three camps: high-power continuous-wave (CW), pulsed, and narrow linewidth single frequency sources.

The very large surface-to-volume ratio of fiber simplifies thermal management or heat removal, and this also enables a compact and robust packaging. Single mode fiber lasers have the diffraction limit output beam quality and high brightness because of the built-in waveguide confinement that is immune to the disturbing thermal effect. The good confinement of pump light in the fiber laser also make it possible to lase at some very weak transitions due to the high intensity pumping. With fiber Bragg gratings (FBGs), fiber lasers can operate at single frequency with a linewidth of 1 KHz [4.1]. The invention of double cladding pumped fiber laser has open the opportunity for fiber lasers to compete directly with high power solid-state lasers. Essentially, fiber lasers allow efficient brightness conversion from the broad area pump laser diodes into a

singlemode diffraction limited beam. The large core double cladding fiber lasers have reached the output power over 2 KW at 1075 nm from Yb-doped single mode fiber laser with a M^2 of 1.1 [4.2].

Although the highest power record of fiber laser is held by Ytterbium-doped lasers at 1 μm region, fiber lasers doped with various rare earths offering other wavelengths from 0.5 μm to 3.4 μm have draw considerable attentions as well. Among them, Erbium and thulium doped fiber lasers have shown their unique attractions because their lasing wavelengths (1.5 and 2 mm) are both in the region so-called "eye-safe". Usually in an erbium doped fiber laser, ytterbium is co-doped with erbium to increase the pump absorption and laser efficiency. Pump photons are initially absorbed by Yb ions because of their stronger and broader absorption band. Then, the energy is transferred nonradiatively from excited Yb-ions to Er-ions, resulting in de-excitation of the Yb ions and excitation of the Er-ions. Such an energy transfer process results in a relatively small slope efficiency of Er-Yb codoped fiber laser. Now the highest power of Er-Yb-codoped fiber laser emit up to around 150 W in the 1.5 μm range. But its efficiency was limited to 33%.

Desire for high power efficient laser source working in eye safe region accelerates the competition in research of thulium-doped fiber lasers that can emit more than 100 W at 1.8 to 2.2 μm with a slope efficiency that can reach 60%. Such a high slope efficiency, which is even higher than the Stokes efficiency, benefits from the cross relaxation energy transfer ($^3H_6$, $^3H_4$ -> $^3F_4$, $^3F_4$) discussed in detail in Chapter 2. In addition to the high quantum efficiency, thulium has also caught considerable attentions recently because of

its wide applications in different fields such as LIght Detection And Ranging (LIDAR), remote sensing, military and medical equipments. The strong and broad absorption of Tm^{3+} at 800 nm that overlaps with the emission band of the commercially available high power AlGaAs laser diode, high quantum efficiency, and broad emission band make Tm^{3+} ion a favorable active source for laser working at 2 μm region.

As we discussed in Chapter 2, high doping concentration leads to large quantum efficiency. Therefore the doping concentration is an essential character that defines the efficiency of thulium doped fiber laser at 2 μm region. In the development of thulium fiber laser, we keep our research focus on efficient laser system with high doping concentrations.

4.2 Thulium doped germanate glass and fiber

There are two IR transmitting glass fiber systems that are relatively similar to conventional silica-containing glass fibers. One is the HMFG (heavy metal fluoride glass) and the other is heavy metal germanate glass fibers based on GeO_2.

HMFG fiber is discovered by Poulain and Lucas in 1975 at the University of Rennes [4.3]. The glass shows a good transparency in the infrared region (up to 8 mm) and has a chemical durability that is comparable with a sodium silicate glass. Its theoretical optical loss was reported to be about 10^{-3} dB/Km at 3 μm which is two order of magnitude lower than the theoretical loss of silicate glass [4.4]. The drawback of HMFG is its low viscosity which will often precipitates crystal during the re-heating of the glass for secondary processing such as fiber drawing.

Although the glass-forming property of germanium dioxide has been known for a long time, the systematic study of germanate glasses and the glassy properties of germanium oxides has only recently begun. The germanate glass consists of a random three-dimensional network of Ge-O-Ge bonds which is similar to silicate glass. Heavy metal oxides are used in glass matrix to shift the IR absorption edge to longer wavelengths [4.5]. The advantage of germanate fibers over HMFG fibers is that germanate glass has a higher glass transition temperature and, therefore, higher laser-damage threshold. The oxide-only germanate glasses possess high glass transition temperatures, excellent durability, and a relatively high refractive index.

In this dissertation, germinate glass is chosen as host material for thulium doped fiber laser. Its phonon energy is lower than that of silicate, which helps to lower the nonradiative decay rate and increase the quantum efficiency; while its high solubility of thulium oxide helps to enhance cross relaxation energy transfer. In addition, the chemical durability and mechanical stability of germanate glass fiber make it a desirable host material in fiber laser area.

4.3 Spectroscopic study of bulk glass

The Tm-doped germanate glass and fiber are made in NP photonics Incorporation. The fabrication of heavy metal germanate glass fiber is similar to any glass-fiber drawing technology. The preforms are made by using mechanical method rather than by a vapor deposition process common with silica fibers. Specifically, cladding tube is fabricated by

ultrasonic drilling on a bulk glass made by melt-casting method. The rod is made by polishing a Tm-doped germanate glass. The preform is made by typical rod-in-tube technique.

The fiber used for fiber laser experiment is drawn in house without polymer jacket on it. The diameter of core and cladding are 7 μm and 125 μm respectively. The N.A. of the fiber core is 0.19.

Absorption spectra of thulium doped germanate glass samples with different doping concentrations are measured under room temperature. The absorption cross section of Tm^{3+} is calculated from absorption spectrum of 4wt% Tm-doped bulk glass sample and presented in Fig. 4.1.

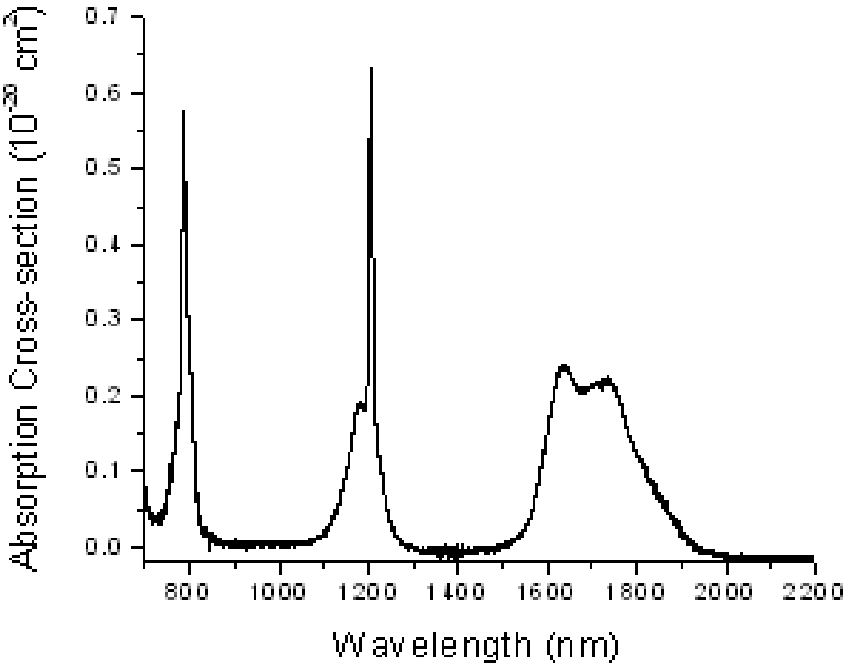

Fig. 4.1 Absorption cross section of Tm^{3+} doped in germinate glass

A multimode AlGaAs laser diode at 800 nm is used to excite ground state Tm^{3+} ions to $^3H_4$ state for the luminance measurement. The fluorescence measurement is similar to the setup described in Fig. 2.6. The fluorescence is collected at 90 degree to the pumping laser to avoid the stimulated emission and re-absorption from ground state of Tm^{3+} ions. The emission fluorescence of transitions $^3H_4 \rightarrow {}^3F_4$ (1.5 μm) and $^3F_4 \rightarrow {}^3H_6$ (1.8 μm) are dispersed by a 1/4m monochrometer (oriel MS 257), detected by a cooled InAs detector, and amplified by a lock-in amplifier.

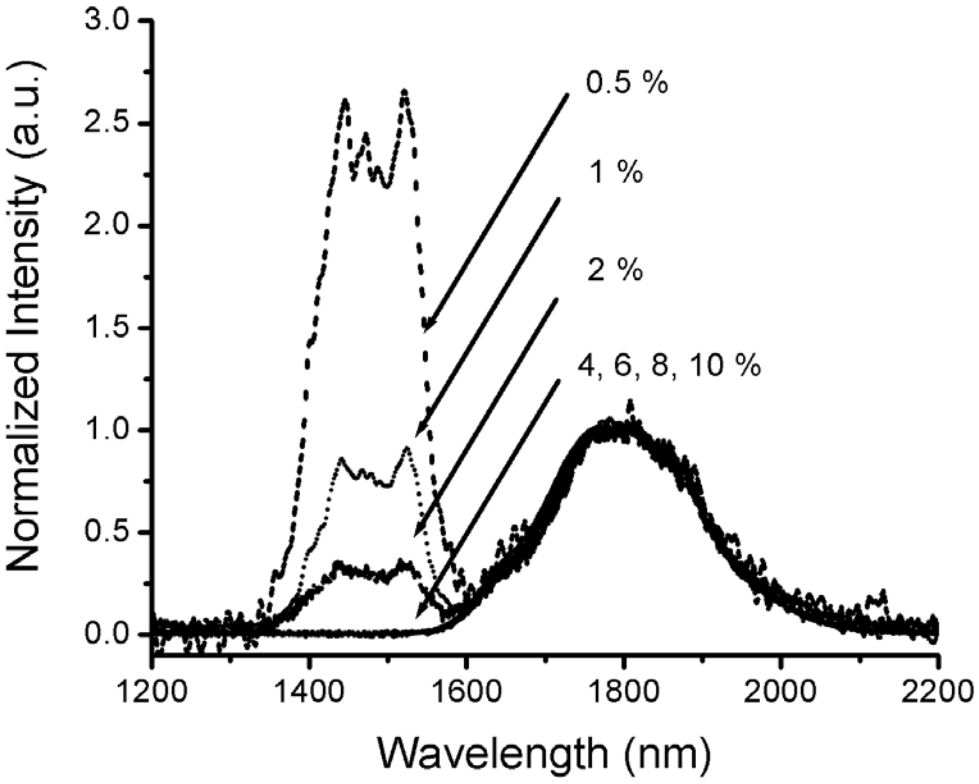

Fig. 4.2 Emission spectra of Tm-dopde tellurite glass samples

Fig. 4.2 shows the emission spectra of germanate glass samples with different thulium doping concentrations. The spectra are normalized at 1.8 μm in order to illustrate the effect of cross relaxation energy transfer on emission spectrum of Tm^{3+} ions. One thing worth noticed is that unlike the spectrum of Tm^{3+} doped in tellurite glass, the spectrum of germinate glass has strong emission spectrum near 1.5 micron when the doping concentration is low. The reason is that the germanate glass we used has higher phonon energy than the tellurite-WO_3 glass has. Therefore the multi-phonon relaxation rate is higher in germanate glass. Considering that the total radiative rate of $^3H_4$ state is an order of magnitude larger than that of $^3F_4$ state, multiphonon decay will have more impacts on the transition of $^3F_4 \rightarrow {}^3H_6$. As a result, in the germanate glass with low thulium doping concentration, the emission intensity of 1.5 mm transition is stronger than the emission intensity of 1.8 mm transition.

Fig. 4.2 also shows that the increase of Tm^{3+} ions doping concentration enhances the fluorescence intensity ratio between 1.8 μm band and 1.5 μm band. That enhancement of ratio results from the cross relaxation energy transfer. According to the theory of multi-polar interaction, the closer Tm^{3+} ions are, the higher transfer rate they get. Therefore, when the doping concentration increases, the cross relaxation energy transfer rate becomes so large that most Tm^{3+} ions at $^3H_4$ state would nonradiatively decay to $^3F_4$ state through cross relaxation energy transfer rather than radiatively decay to $^3H_4$ state by emitting 1.5 μm photons. Fig. 4.2 also indicates that the intensity ratio increases rapidly when the doping concentration changes from 0.5 wt% to 4 wt%. Afterward the ratio doesn't change as rapidly as it does in small doping concentration range.

A modulated AlGaAs laser diode at 800 nm is utilized to excite the glass samples for lifetime measurement of the upper lasing level, $^3F_4$ state. The setup is shown in Fig. 2.11. Lifetime is defined as the time when intensity drops to 1/e of the peak value. In order to avoid the delay of the lifetime due to reabsorption from unexcited thulium ioins, the fluorescence of 1.8 μm is collected at 90 degree from the incident pumping laser, detected by an InAs detector and recorded by a digital oscilloscope.

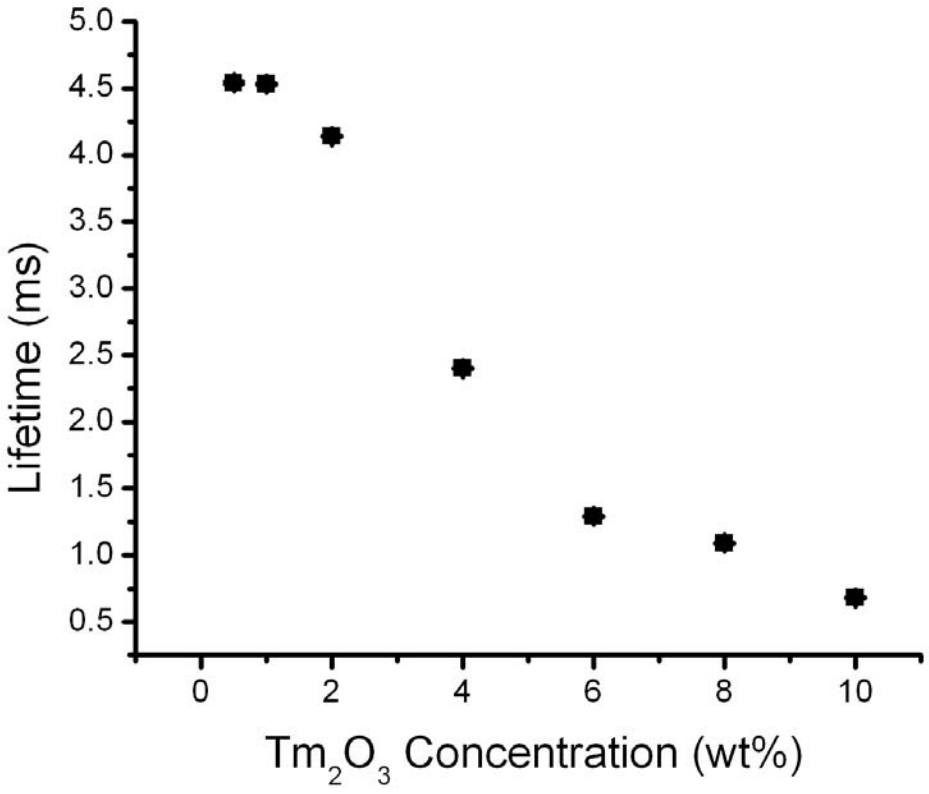

Fig. 4.3 Lifetime of 3F4 state of Tm3+ doped in germanate glass with different doping concentrations

Fig. 4.3 shows the lifetimes of $^3F_4$ state of glass samples with different doping concentrations. The reduction of lifetime versus concentration is observed. The increase of doping concentration enhances the probability of one excited Tm^{3+} ion meeting a quenching center, such as OH radical, through a nonradiative energy migration process between Tm^{3+} ions. In Tm-doped germinate glass, concentration of $^-$OH radical has great impacts on the lifetime of $^3F_4$ state because of the overlap between absorption band of $^-$OH radical and emission band of transition of $^3F_4$ -> $^3H_6$. Thulium doped germanate glass samples with same doping level but different percentage of OH radical, which leads to low transmission at 3.3 μm, are fabricated. The lifetime measurements of those samples show that the lifetimes of glass samples with high percentage OH radical drop dramatically. For examples, the lifetime of 3 wt% sample declines from 3.2 ms to 1.4 ms, when the transmission of bulk glass sample at 3.3 μm changes from 81% to 59%. Concentration quenching leads to a significant heat load. And it is a serious problem in the high power laser application because the most quenched energy gets converted into heat eventually.

All the temporary fluorescence decays of glass samples with different doping concentrations are found to be described by a single exponential decay. Since the reverse cross relaxation energy transfer ($^3F_4$, $^3F_4$-> $^3H_6$, $^3H_4$) proportional to the square of population of $^3F_4$ state, the above results implies that there is no significant reverse energy transfer in glass samples with doping concentration up to 10wt%.

4.4 Fiber laser performance

A cut back technique, which measure the loss of bare fiber by measuring the optical power transmitted through a long length then cutting back to the source and measuring the initial coupled power, is used to measure the propagation loss of 1310 nm laser in the fiber core, and result is presented in Fig. 4.4.

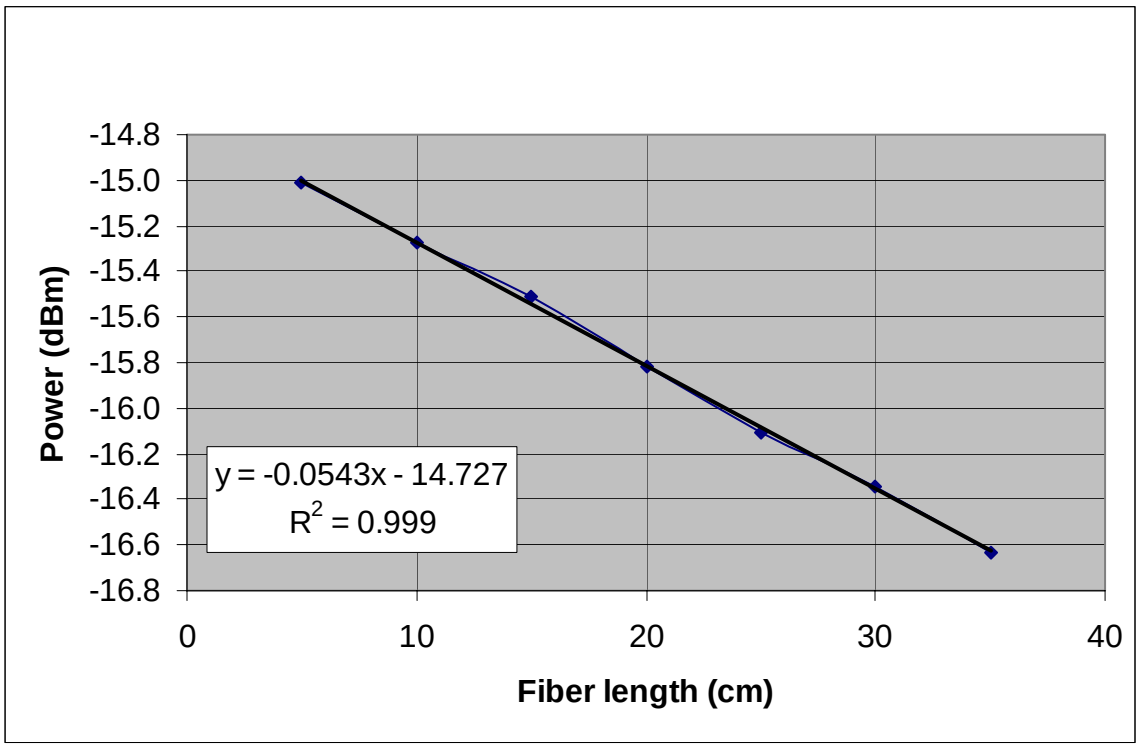

Fig. 4.4 Cutback measurement of Tm-doped germanate fiber

The propagation loss of signal laser in the fiber core is 0.05 dB/cm. Such a loss is quite low, considering that the fiber is made by rod-in-tube technique that creates inherent problems such as the formation of bubbles, core-clad interface irregularities.

The same technique is used in pump absorption measurement under non-lasing condition, as well. A single mode AlGaAs laser diode at 808 nm is used instead of 1310 nm laser. The pump absorption is measured 2.2 dB/cm. It's very close to the simulation results from the glass absorption coefficient. Because 800 nm excitation ($^3H_6 \rightarrow {}^3H_4$) is not an in-band pump process for lasing transition of $^3F_4 \rightarrow {}^3H_6$ at 1.9 mm, the absorption of fiber under lasing condition does not have much big difference from the absorption we measured from cut back measurement.

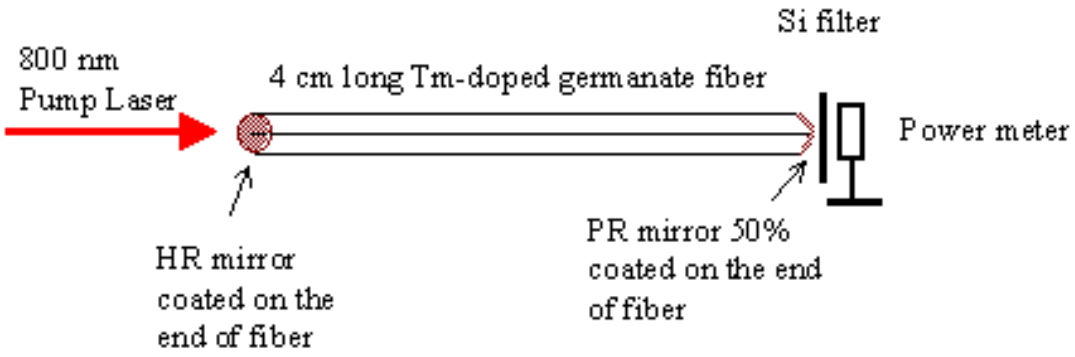

Fig. 4.5 Tm-doped germanate fiber laser set-up

Laser action at 1.9 μm is obtained from 4 wt% Tm_2O_3 doped germanate fibers with different fiber lengths (2cm, 3 cm, and 4 cm). The laser demonstration setup is shown in Fig. 4.5. Both ends of the thulium doped germanate fibers are perpendicularly cleaved and coated with dielectric mirrors to build Fabry-Perot laser resonators. Such a cavity structure can improve the mechanic and thermal stability of the cavity especially in the high power condition. The pumping end of fiber laser is coated with dichroic mirror of

high reflectivity at 1.9 μm and high transitivity at 800nm. The other end of fiber laser is coated as an output coupler with reflectivity of 50% at 1.9 μm. A wedged-shape lensed fiber is used to convert highly elliptical beam shape from a single-mode 808nm laser diode into round shape modes supported by SMF-28 fiber. Butt coupling between the SMF-28 fiber and the germanate fiber laser is used to inject the pumping laser into the germanate fiber laser. The coupling loss is estimated by measure the coupling loss of 1310 nm laser that is 0.8 dB. Laser output power is measured by a thermal power meter placed at the output end of fiber lasers. A silicon filter is placed in front of the power meter to block the residual pump laser. The spectrum of 4 cm long fiber laser is illustrated in Fig. 4.6.

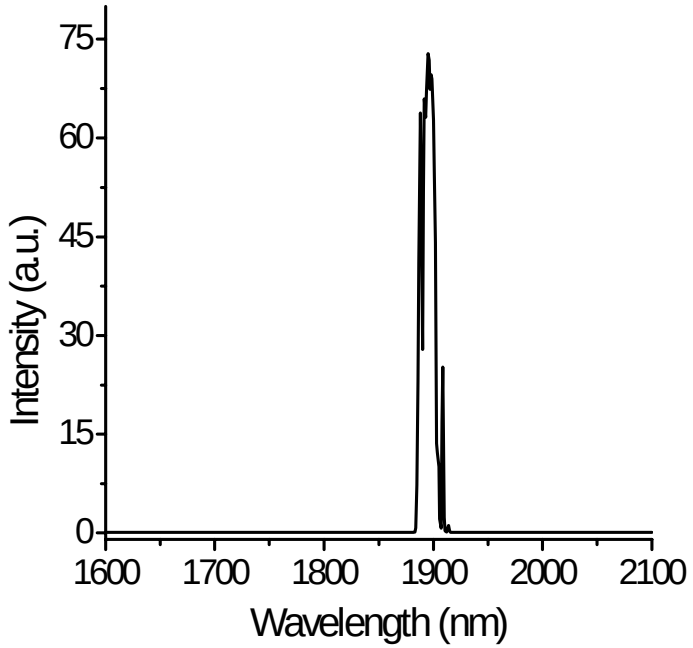

Fig. 4.6 Laser spectrum of 4 cm long Tm-doped germanate fiber laser

It shows the lasing wavelength is at 1.9 mm, which is 100 nm away from the emission peak. Given that the emission band of Tm^{3+} ($^3F_4 \rightarrow {}^3H_6$) starts from 1600 nm, the energy difference between the lowest level of ground state and lower lasing level of 1.9 mm is about 980 cm^{-1}. According to the Boltzmann distribution, it is reasonable to claim that this laser system is a quasi-three-level system, in which lower laser level is the sublevel of ground state.

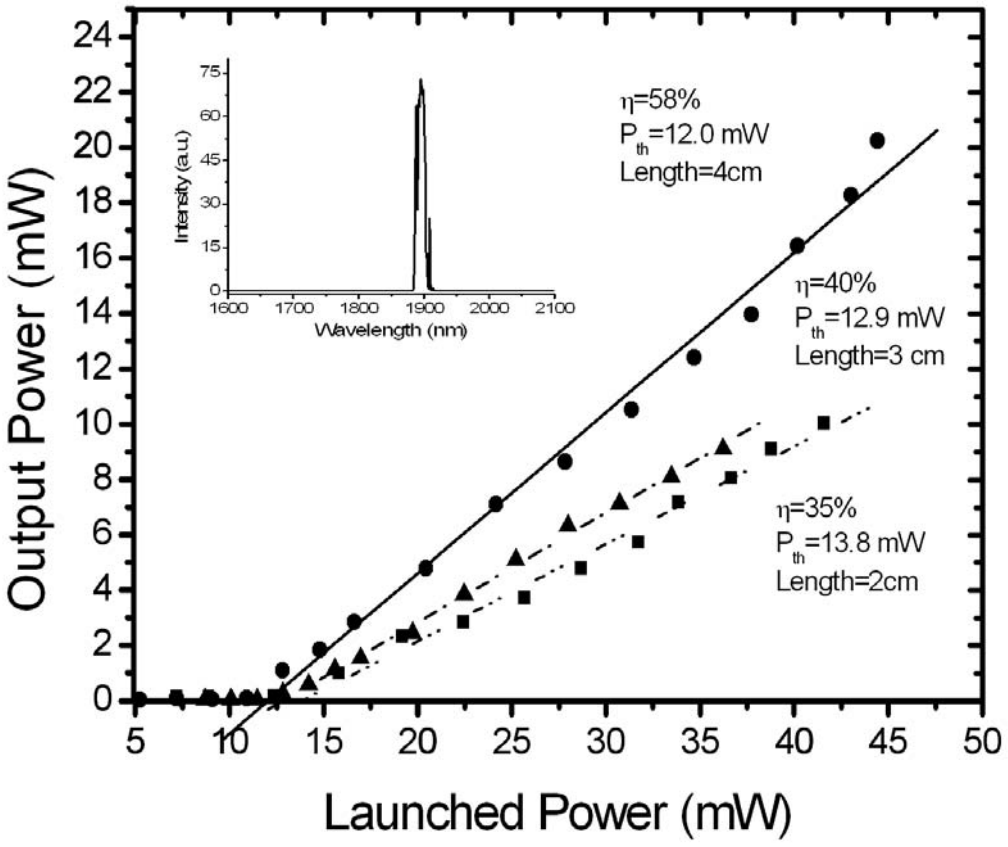

Fig. 4.7 Power curves of fiber lasers with different lengths

The output power of the fiber laser with different lengths versus launched pumping power is plotted in Fig. 4.7. The linear extrapolations of the output power data to zero yield the launched pump thresholds of fiber lasers with different lengths. They are 13.8 mW, 12.9 mW, and 12 mW for 2 cm, 3 cm, and 4 cm long fibers respectively. Such low thresholds benefit from: (1) the laser transition is a quasi-three-level system which has a higher efficiency compared with a traditional three-level system due to small amount of reabsorption from ground state ions; (2) the cross relaxation energy transfer greatly improves the pumping efficiency by increasing the quantum efficiency; (3) tight confinement of pump laser in the small core of fiber laser. Digonnet derived an equation for calculation of pump threshold for fiber lasers [4.6],

$$P_{th} = \frac{\alpha + \delta_0 / 2}{\kappa}, \tag{4.1}$$

$$\alpha = \sigma_a N_0 \eta_s L, \tag{4.2}$$

$$\kappa = (1 + \gamma_s) \frac{\sigma_e \tau_f}{h \upsilon_p} \frac{F}{A \eta_p}, \tag{4.3}$$

$$\gamma_s = \sigma_a / \sigma_e \tag{4.4}$$

where $\sigma_{\alpha e}$ is the absorption/emission cross-section at lasing wavelength; N_0 is doping concentration, $\eta_{s/p}$ is the overlap between signal laser/pump and dopant profile; L is the length of fiber laser; τ_f is the lifetime of upper laser level; υ_p is the pump frequency; A is the area of fiber core; F is the overlap between pump and signal mode profiles and dopant profile.

Given the N.A. and core size of the germanate fiber laser, the thulium doped germanate fiber supports a single mode propagation of signal laser at 1.9 μm and multi-mode propagation of pumping laser at 808 nm. According the waveguide theory, the multimode distribution can be obtained by solving the characteristic quations,

$$\frac{\beta^2 v^2}{a^2}[\frac{1}{\gamma^2}+\frac{1}{\kappa^2}]^2=[\frac{J_\nu^{'}(\kappa a)}{\kappa J_\nu(\kappa a)}+\frac{K_\nu^{'}(\gamma a)}{\gamma K_\nu(\gamma a)}]\times[\frac{k_0^2 n_{core}^2 J_\nu^{'}(\kappa a)}{\kappa J_\nu(\kappa a)}+\frac{k_0^2 n_{clad}^2 K_\nu^{'}(\gamma a)}{\gamma K_\nu(\gamma a)}] \tag{4.5}$$

$$\gamma^2=\beta^2-k_0^2 n_{clad}^2 \tag{4.6}$$

$$\kappa^2=k_0^2 n_{core}^2-\beta^2 \tag{4.7}$$

where β is the propagation constant calculated by boundary conditions using weak guided fiber assumption., $\boldsymbol{u}$ is the mode number, a is the radius of the fiber core, k_0 is the vacuum wave number, $J_{\mathbf{u}}$ is Bessel function of the first kind of order u which is used to describe the radial standing wave in a cylindrical structure. $K_{\mathbf{u}}$ is $K_\lambda(x)$ is the Bessel function of the second kind of order υ that is used to describe the evanescent fields. Solutions of above equations shows that there are four modes (LP01, LP11, LP21, and LP02) of pump laser propagating in the fiber laser.

The overlap coefficients $\eta_{s/p}$ are calculated by [4.7],

$$\eta_{s/p}=\frac{P_{core}}{P_{tot}}=1-\frac{u^2}{V^2}(1-\frac{K_l^2(w)}{K_{l-1}(w)K_{l+1}(w)}) \tag{4.8}$$

$$u=a(k^2 n_{core}^2-\beta^2)^{1/2} \tag{4.9}$$

$$w=a(\beta^2-k^2 n_{clad}^2)^{1/2} \tag{4.10}$$

$$V^2=u^2+w^2 \tag{4.11}$$

where $n_{core/clad}$ are the refractive indices of core and cladding glass. V is the normalized frequency of fiber. Substituting fiber parameters into Eq. [4.8] provides η_s=0.80 and η_p=0.90 respectively. It indicates that the pumping laser is well confined in the core of the fiber laser. From Eq. [4.1], we can find the absorbed pump thresholds for 2 cm, 3 cm, and 4 cm fiber lasers are 7 mW, 9mW, and 12 mW. The calculation shows that shorter fiber has lower pump threshold, which does not agree with our experimental results. The reason is that the thresholds we got from extrapolation of experiment data are the launched pump thresholds instead of the absorbed pump thresholds given by Eq [4.1]. The smallest difference between absorbed pump threshold and launched pump threshold of 4 cm long fiber laser indicates that 4 cm long fiber laser has the best absorption of launched pump laser among others.

The slopes of linear fits of laser output data are used to determine the slope efficiencies of the fiber lasers with different lengths. For 2 cm, 3 cm, and 4 cm long fiber lasers, they are 35%, 40%, and 58% with respect to the launched pumping power. The 58% slope efficiency of the 4 cm long fiber laser is significantly larger than Stockes efficiency of 42%. R.A. Hayward [4.8], has reported a 2.2 wt% thulium doped silicate fiber laser with a slope efficiency of 46%. To the best of our knowledge, this 58%, is the highest reported slope efficiency of Tm-doped fiber laser according to the launched pump power. Such high slope efficiency of laser output benefits from the high doping concentration that is allowed in germanate glass. The quantum efficiency of Tm^{3+} can be calculated by below equation [4.6],

$$\eta_q = \eta_{laser} / (\frac{T_1}{\delta_0} \frac{h\nu_s}{h\nu_p} \eta_p), \quad (4.12)$$

where T_1 is the transmission coefficient of the output coupler. $\upsilon_s$is the frequency of signal laser, and η_{laser} is the slope efficiency according to absorbed power. Above discussion shows that the launched power of 4 cm fiber laser is quite close to the actual absorbed pump power.

Therefore, η_{laser} in Eq. [4.12] is replaced by experiment slope efficiency of 4 cm long fiber laser to calculate the quantum efficiency of Tm^{3+} 4 cm long fiber laser. The calculated quantum efficiency equates to 1.79. Such high quantum efficiency of fiber laser represents a large cross-relaxation energy transfer rate due to the high doping concentration of Tm^{3+} in the germanate fiber. Higher slope efficiency can be achieved by using the optimal output coupler, fiber laser length and reducing the cavity loss.

4.5 Pump efficiency of pump wavelength

Although thulium doped germanate glass fiber laser is a quasi-three-level laser system, small amount of reabsorption of signal laser from Tm^{3+} at lower lasing level will decrease the efficiency of the laser. Under such condition, pump laser inside of the fiber laser needs to be uniformly distributed along the fiber length. In order to pump through the entire fiber, the wavelength of pumping laser needs to be tuned to the wing of absorption band instead of the absorption peak. So that part of pumping laser can get through the beginning part of fiber and make the rest fiber under pump due to the small

absorption of thulium. Such a pump scheme is also good in terms of thermal management of fiber laser. One draw back of end-pumping fiber laser is that lots of pump power is absorbed at the beginning part of fiber laser and converted into heat due to the multiphonon decay. Wing pump allows the thermal power generated in the fiber core to be distributed over a long length instead of just the beginning tip of the fiber laser. Therefore, thermal management of fiber laser becomes practical especially at high average power operation.

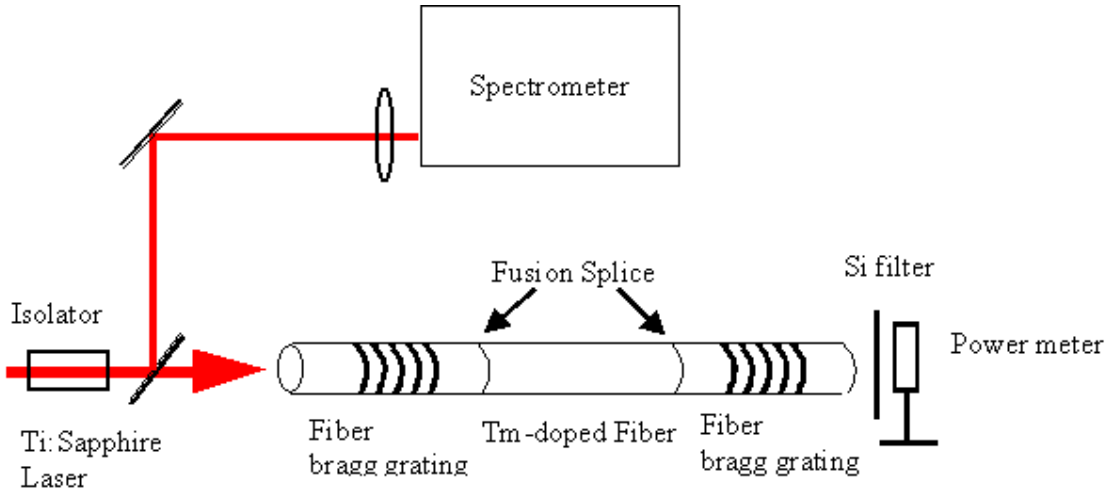

Fig. 4.8 Setup for fiber bragg grating fiber laser

A piece of 4 cm long thulium doped germanate fiber is used to examine the efficiency of different pump wavelengths. The experiment setup is shown in Fig. 4.8. To make sure the experiment is conducted under the same situation for different pumping wavelengths, a pair of fiber Bragg gratings (FBGs) are spliced to the fiber as HR mirror and output coupler with a total loss of 1.28 dB. With this fiber laser configuration, the

cavity loss of fiber laser is steady; pump coupling efficiency is stable; lasing wavelength of fiber laser is fixed. A Ti:Sapphire tsunami laser is used as tunable pumping source, because its linewidth is much narrower than the one of semiconductor laser diode. Therefore the efficiency of pumping wavelength can be examined without overlapping effects. A free space isolator is placed at the output of Tsunami to block any possible feed back from coupling setup. The pump wavelength is monitored during the measurement. There is no pumping wavelength shift caused by feedback is observed.

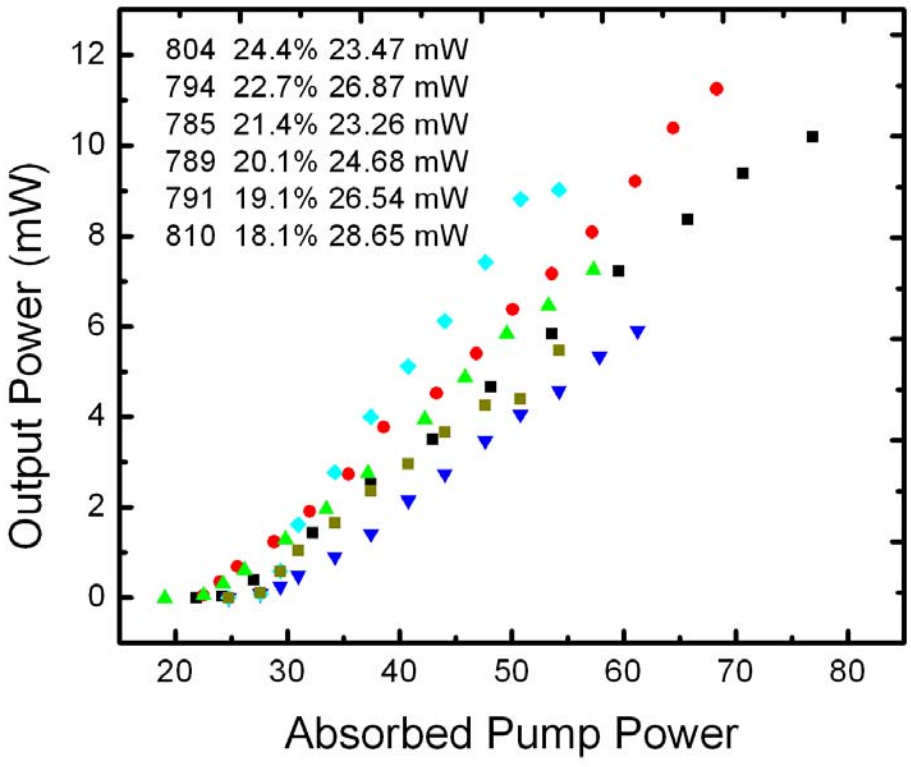

Fig. 4.9 Power curves of 4 cm long fiber laser pumped with different wavelengths

Fig. 4.9 shows the power curves of fiber laser pumped by laser at different wavelengths. The output power is plotted versus the absorbed power. The absorption cross section of pumping band is also shown in Fig. 4.9. Fig. 4.9 shows that the highest slope efficiency of fiber laser is achieved when pumping wavelength is at 804 nm instead of at the absorption peak of Tm^{3+}. The result confirms that the distribution of pumping power in the active fiber will affect the fiber laser performance.

Fiber Bragg gratings are short lengths of optical fiber that reflect at a particular wavelength. A fiber Bragg grating is a periodic perturbation of the effective refractive index in the core of an optical fiber. The perturbation is approximately periodic over a certain length of e.g. a few millimeters or centimeters, with a period in the order of hundreds of nanometers. Only the light that satisfies the Bragg grating condition gets reflected. The Bragg grating condition means that the wavenumber of the grating matches the difference of the wavenumbers of the incident and reflected waves. The typical linewidth of reflection is from 1 to 0.02 nm. The magnitude of reflection depends on the length of the grating and the refractive change of the core.

It is well known that FBGs are sensitive to strain and temperature effects [4.9], and in fact they have been used successfully in many applications from communications to sensors. The wavelength tuning can be achieved through either mechanical strain or thermal methods. In this dissertation a thermal tuning method is developed to measure the reflection and bandwidth of the gratings for the lack of 2 μm ASE source. As we know the refractive index of glass changes with the temperature. Therefore the periodical refractive index distribution in the fiber bragg grating also changes with the temperature

of the fiber. Thermal tuning effect of fiber Bragg grating can be expressed by the following equations:

$$\lambda_B = 2\Lambda n_{eff} \tag{4.11}$$

$$\Delta\lambda_B = 2[\Lambda \frac{\partial n_{eff}}{\partial T} + n_{eff} \frac{\partial \Lambda}{\partial T}]\Delta T \approx 2\Lambda n_{eff} \times (\frac{1}{n_{eff}} \times \frac{dn_{eff}}{dT})\Delta T = \lambda_B \times \alpha_n \times \Delta T, \tag{4.12}$$

$$\alpha_n = \frac{1}{n_{eff}} \times \frac{dn_{eff}}{dT} = 8.6 \times 10^{-6} \tag{4.13}$$

where λ_B is the wavelength of peak reflection. Λ is the grating period and n_{eff} is the effective refractive index of core. **D***T* is the temperature difference of the fiber. Our grating is written on SMF-28 fiber whose thermal-optic coefficient ($\frac{1}{n_{eff}} \times \frac{dn_{eff}}{dT}$) is much larger then the thermal expansion coefficient ($\frac{1}{\Lambda}\frac{\partial \Lambda}{\partial T}$). Therefore only thermal optics effects are considered in the calculation.

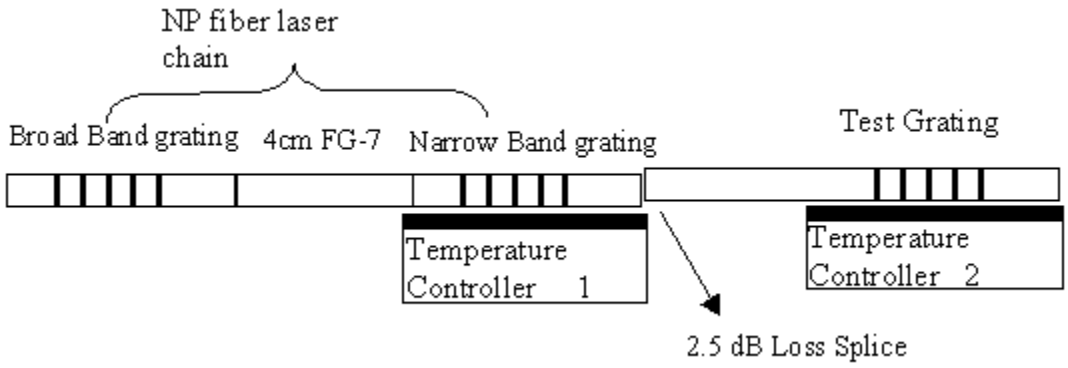

Fig. 4.10 Setup for fiber bragg gratings measurement

The fiber grating at 1.9 μm used in experiment is obtained from O-Eland. Fig. 4.10 shows the set-up of measurement. A 4 cm long fiber DBR laser serves as a light source. A narrow band grating is used as output coupler to prevent the laser mode hoping, which helps to get a narrow linewidth laser during the measurement of gratings. Such a stable narrow linewidth laser helps to improve the resolution of measurement. Test grating is spliced to the output of fiber laser with a loss of 2.5 dB by misalignment during the splice. Such a loss between output laser and test grating is employed to block the possible feedback from test grating, which might disturb the fiber DBR laser. Temperature controller 1 is used to tune the output laser wavelength to make it in the wavelength range of test fiber grating. Temperature controller 2 is used to tune the wavelength of test grating, so that the fiber laser can sweep the whole range of gratings. The power of laser transmitting through the test grating is recorded while the temperature of test grating is tuned by temperature controller 2. Such curve can be considered as the transmission spectrum of grating.

Fig. 4.11 (a) and (b) are the results of broadband grating and narrow band grating. They clearly show that the broad band grating needs more temperature tuning range to cover the whole transmission spectrum. According to Eq. (4.12), the reflection wavelength of our grating change at a rate of 0.016 nm/*K*. Therefore that the bandwidth of broadband grating and narrow band grating are 0.8 and 0.3 nm. Because the measured output laser power can be considered as a linear function of the grating transmission, the reflection of the grating can be calculated by $(1 - P_{\min} / P_{\max})$. They are 81% and 93% for broadband and narrow band grating respectively.

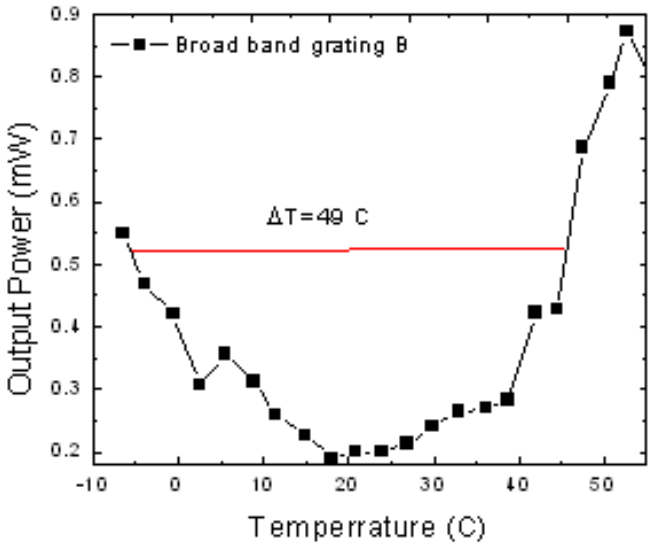

Fig. 4.11 (a)

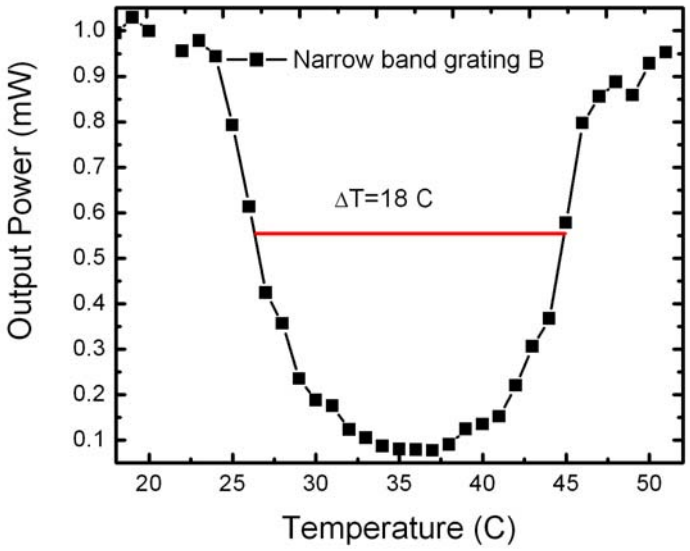

Fig. 4.11 (b)

4.6 Single frequency fiber laser

Narrow linewidth single frequency laser is another topic that has attracted intense research activities in fiber laser field. The long coherence length benefiting from the narrow linewidth has found wide applications in sensing, lidar, and fundamental research. Single-frequency operation is usually obtained when the bandwidth of the gain is smaller than the frequency spacing of the cavity modes caused by spatial hole burning. As a result, single frequency operation requires a short resonant cavity to make the free space range (FSR) larger than bandwidth of grating. The free space range is described by,

$$\Delta\nu = \frac{c}{2nL}$$

$$\text{or } \Delta\lambda = \frac{\lambda^2}{2nL} \tag{4.14}$$

where L is the laser cavity length, n is the refractive index and λ is the lasing wavelength. The gain per unit length of the active fiber in such a short cavity needs to be large enough to compensate the cavity loss in order to reach the laser threshold. Because the high transverse propagation modes also generate laser actions at slightly different frequencies, gain of the single frequency fiber laser cannot be improved by simply increasing the core size of the fiber. Instead, high doping concentration glass is utilized in fiber laser to increase the gain of fiber for single frequency operation. Germanate glass with thulium doping concentration of 5 wt% is used to fabricate the core of fiber (FG-7) for single frequency operation. The propagation loss of FG-7 is measured by cutback measurement and shown in Fig. 4.12. The propagation loss is 0.05 dB/cm.

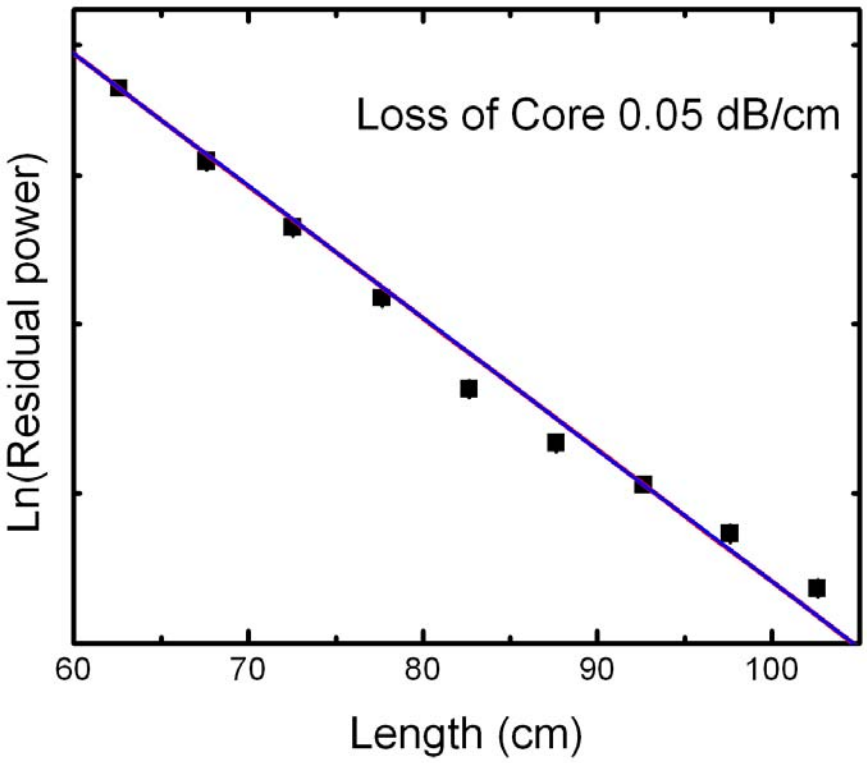

Fig. 4.12 Cutback measurement of FG-7 germanate fiber

Single frequency laser demonstration has been achieved in a 2 cm long FG-7 fiber spliced with the fiber bragg gratings at 1893 nm. Both of the broad and narrow gratings are measured as discussed in section 4.6. The loss of the short fiber laser chain is 1.23 dB at 1310 nm. The broadband grating is used as output coupler since it has a lower reflection at lasing wavelength. A He-Ne laser is launched into the fiber grating to locate and measure the length of the gratings by observing the diffracted red light. The lengths of broadband grating and narrow band grating are 2 and 12 mm respectively. Therefore, the total length of fiber laser cavity is about 3cm long. According to the Eq. (4.14) , the

FSR of the fiber laser cavity is 3.3 GHz. In order to avoid the mechanic vibration that would change the cavity length and disturb the laser wavelength, the Fiber laser chain is placed in the V-groove by epoxy. Two sets of temperature controllers are used to tune and stabilize the gratings wavelength separately. Temperature of narrow grating is tuned to reach the most powerful laser output due to the wavelength match of two gratings. The fiber laser power curve is shown in Fig. 4.13. The pump threshold is 22 mW.

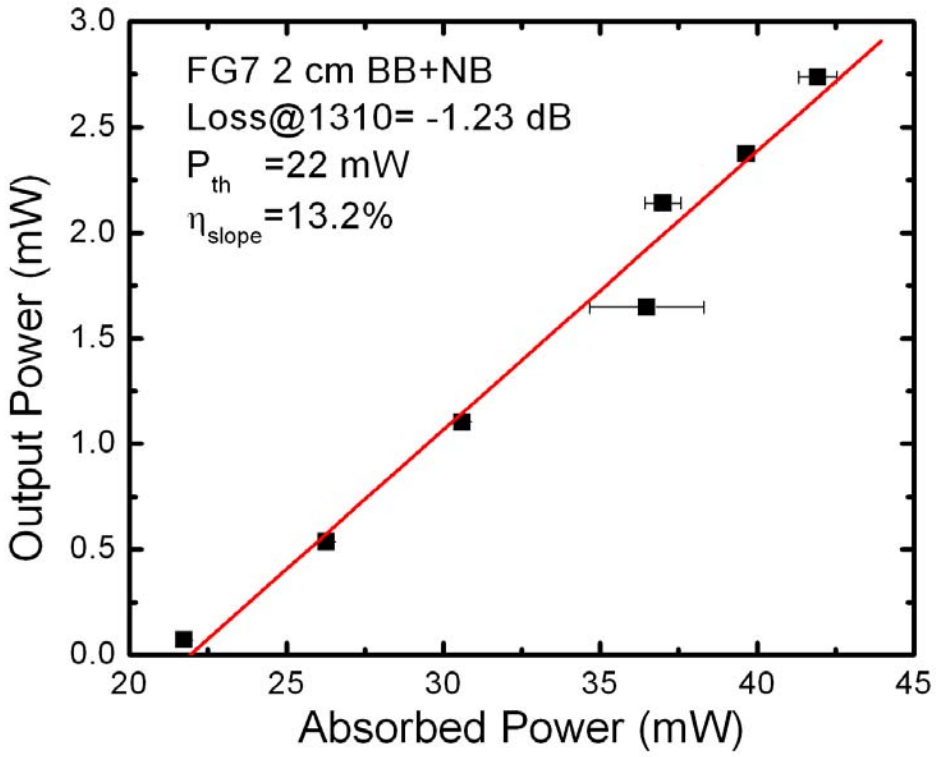

Fig. 4.13 Fiber laser output power Vs absorbed pump power

A Fabry-Perot interferometer scanner is designed and fabricated to measure the single frequency laser. A Fabry-Perot interferometer uses the optical transmission characteristics of a Fabry-Perot (F-P) resonator as a filter to scan across the optical spectrum of the laser. Any F-P resonator is a linear resonator that consists of two highly reflecting mirrors. It will have a transmission behavior that has peaks and valleys based on wavelength. The peaks will be located where the distance between mirrors is an integer multiple of one half the laser wavelength. As the reflectivity of the mirrors approaches 100 percent, the peaks become increasingly narrow and the valleys increasingly flat and close to zero transmission. The resonance frequencies can often be tuned by changing the cavity length with a piezo actuator. If one periodically varies the voltage applied to the PZT, and monitors the transmitted power versus time with a photodetector and an oscilloscope, one can directly get the optical spectrum of the incident light displayed on the scope, provided that the spectral width is smaller than the free spectral range.

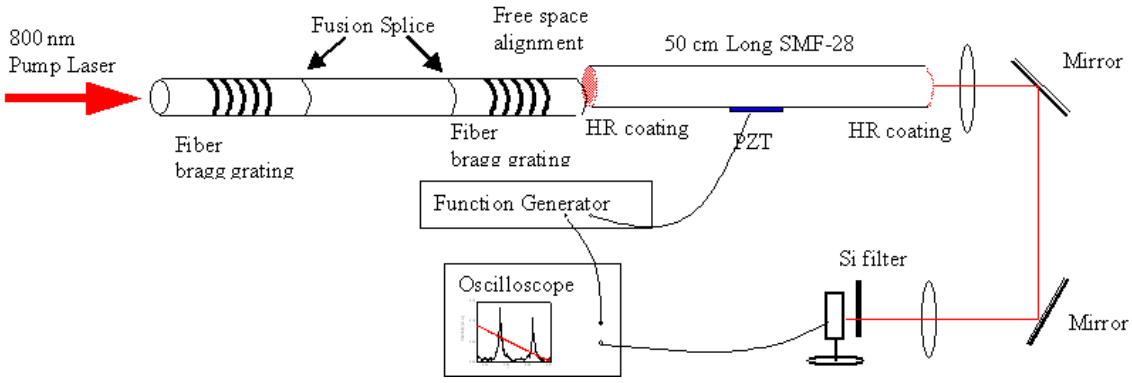

Fig. 4.14 Single frequency fiber laser

The setup is shown in Fig. 4.14. Both ends of a 50 cm long SMF-28 fiber are coated with high reflection (R~92%) dialectical mirrors at 1.9 μm to form a F-P cavity. The resonance frequencies are tuned via cavity length changes achieved with a PZT attached to a piece of fiber inside the F-P cavity. Free space coupling is used to launch the laser into F-P scanner. Some misalignments between fiber laser and Fabry-Perot interferometer are introduced to prevent the possible feedback from HR mirror of the Fabry-Perot interferometer into the fiber laser cavity. A saw-tooth-like voltage (P-P ~ 50 V) is applied to the PZT to tune the length of F-P cavity. Fig. 4.15 shows the mode spectrum of the 2-cm FG-7 fiber laser monitored by scanning F-P interferometer. The triangular waveform represents the voltage applied. A scan over one FSR shown in Fig. 3 confirms a single frequency operation in 2-cm-long FG-7 fiber laser. The finesse of cavity is measured 36. The finesse of the scanning F-P cavity can be further improved by using coating with higher reflection. The intensity difference of two peaks results from

the variation of laser power, which is the result of fluctuation of pump laser diode both in spectrum and amplitude.

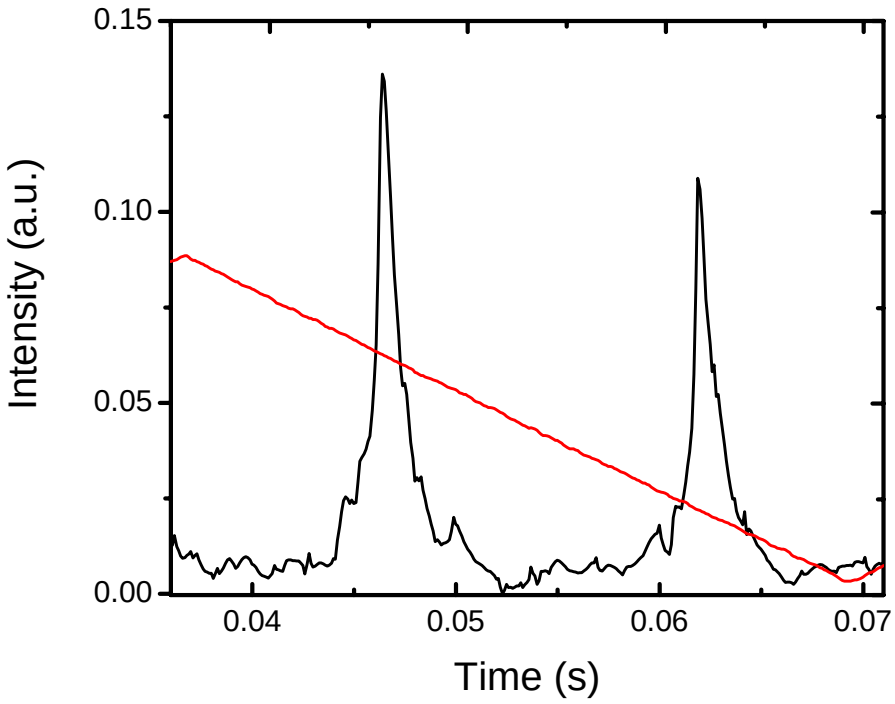

Fig. 4.15 Mode spectrum of the 2-cm FG-7 fiber laser

4.7 Tm-doped high power fiber laser

High power laser has found its unique position in both scientific research and industrial application, and is keeping exploiting new markets. The most common high power laser in the commercial market is CO2 laser and Nd:YAG laser. These lasers are used in all kinds of industrial applications including: metal cutting, welding, silicon cutting, ceramic scribing, spot welding, bending, powder deposition, surface modification

and marking. Recently development of fiber laser makes it an alternative source of high power solid-state laser. Compared with traditional solid-state laser, fiber lasers offer efficient operation, high-beam quality and maintenance-free running. It has been replacing solid-state laser in lots of industrial area.

For industrial application of high power laser, the top issue is cost. The possibility of mass production of fiber laser enhances its competitive edge. Another crucial aspect is the low power consumption that is a cost over the lifetime of the product. In term of efficient power consumption, one promising candidate of high power fiber laser is thulium doped fiber laser due to its high slope efficiency. In this dissertation we start to study thulium doped germanate fiber laser as a potential high power laser source.

Pump absorption is a very critical issue, especially for short length fiber. When the slope efficiency of the fiber laser is fixed, how much output power is determined by how much pump power fiber can absorb. Most high power laser diodes used as pump sources are multimode laser diodes that have a larger emitting area and are impossible to be confined in the single mode core of fiber. Double cladding helps the fiber to increase the launching area and to confine the multimode pump laser inside the fiber. While pump laser propagates inside the cladding in a zig-zag way, it will keep passing through the core are of fiber. As soon as the pump laser enters into the fiber core, it will be absorbed by thulium doped inside and converted into signal laser. In such a configuration the pump power can be launched into the inner cladding without affecting the single mode laser action in the core.

Fg-9 fiber is specially designed in NP photonics for high power applications. It is a double cladding fiber. 4 wt% thulium doped germanate glass is used to fabricate the core of fiber with a radius of 6 micron. The N.A of the core is 0.1. The V number of fiber is 1.89 that is smaller than the single mode condition of step index fiber. It can provide a diffraction-limited laser output. The diameter of inner cladding is 100 ㎜. The outside cladding is 140 ㎜ in diameter.

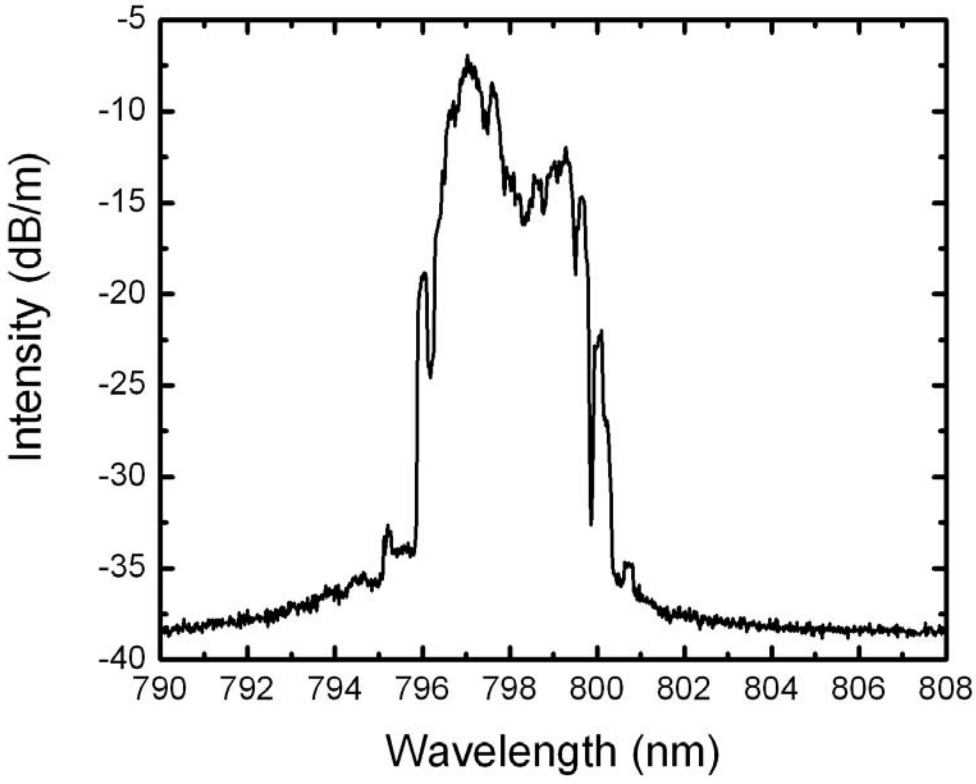

Fig. 4.16 Spectrum of pump laser used in cutback experiment

Cutback measurement is used to measure the pump laser absorption of double cladding fiber. Pump source is a fiber coupled laser diode whose spectrum is shown in Fig. 4.16. The result of cutback experiment in a piece of 95-cm-long FG-9 fiber is shown in Fig. 4.17. The pump fiber is delivered by a 100/140 multi-mode fiber with a N.A. of 0.22. Fig. 4.17 shows that the absorption coefficient is not linear, which is not consistent with the Beer's law.

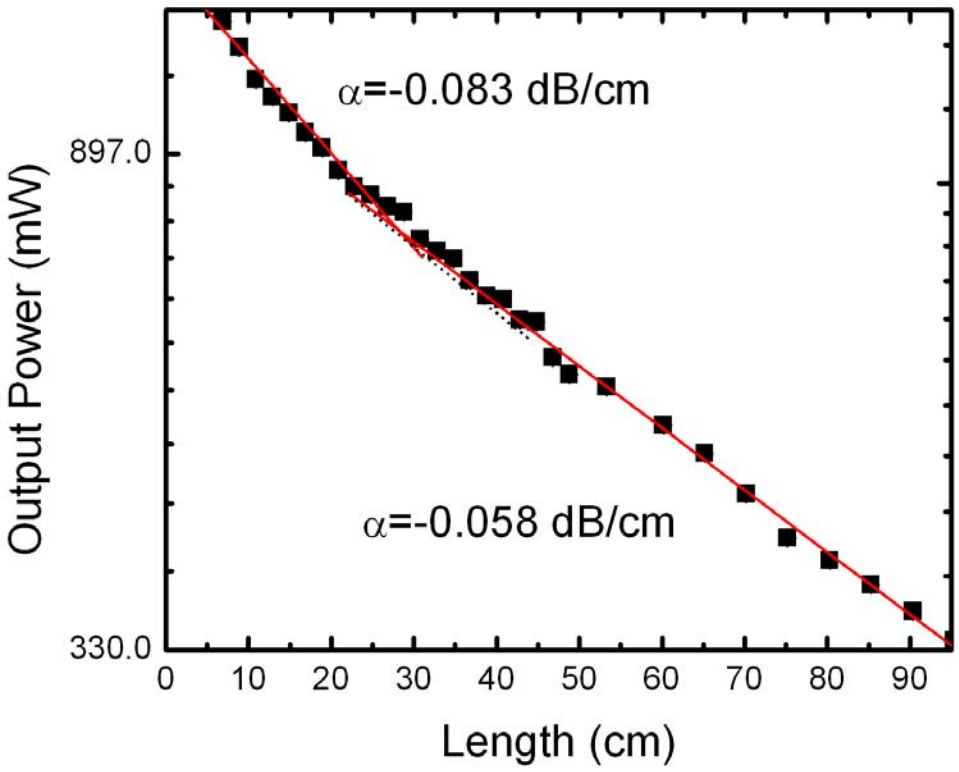

Fig. 4.17 Cutback of pump absorption of Tm-dopde double cladding fiber

The absorption coefficient of beginning part of the fiber is much larger than the lateral part. Such a nonlinear behavior of absorption coefficient of double cladding fiber

originates from the changes of overlap between high order pump modes and doped core area. Absorption can only occur if there is an overlap of the pump modes distribution in the double-clad fiber with the doped inner core. According to the theory of multi-modes propagation, only a small fraction of the pump laser propagates in the core of the fiber and is absorbed by the doped inner core. Therefore a high fraction of the ensemble of non-absorbing modes does not contribute to absorption. Thus the absorption coefficient decreases because the ratio of the ensembles is shifted towards the fraction of non-absorbing modes after propagating along the fiber for a certain distance.

Since most of the unperturbed modes almost do not overlap the absorbing core in a perfect circular step index fiber, the mode mixing can significantly increase the pump absorption. Several techniques have been developed to increase the pump inner-cladding mode mixing in double cladding fiber laser, such as using an irregular shape cladding and irregular distribution of refractive index. In our experiment, double cladding fiber is bended to increase the chaos of the high order pump modes in the cladding. Such modes mixing mechanism significantly helps to increase the fraction of absorbing modes and improve the absorption efficiency in a circular double cladding fiber.

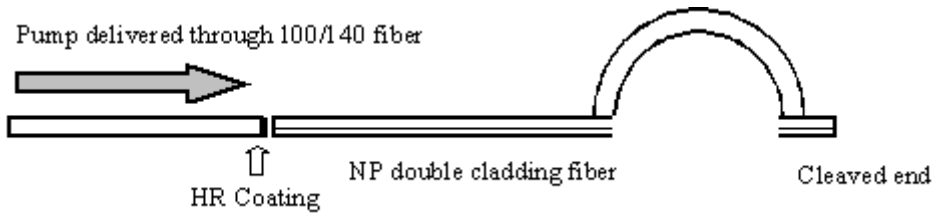

Fig. 4.18 setup of high power fiber laser

A 4 W Tm-doped germanate fiber laser is achieved from a 40-cm long FG-9 fiber. The laser set-up is illustrated in Fig. 4.18. The fiber is placed on a copper plate and bended with a radius of 4 cm. A commercial 100/140 silica fiber with a HR coating at 1900 nm and HT coating at 800 nm is used to launch the pumping laser into the Tm-doped germanate fiber laser. The other end of fiber laser is perpendicular cleaved and used as an output coupler. The reflection of output coupler is 5%. There is no active cooling system is used to cool the fiber laser. The output power versus absorbed power is presented in Fig. 4.19. The slope efficiency of the laser is 35.6%. The absorption of pump has been increased from 41% to 68% after fiber is bended.

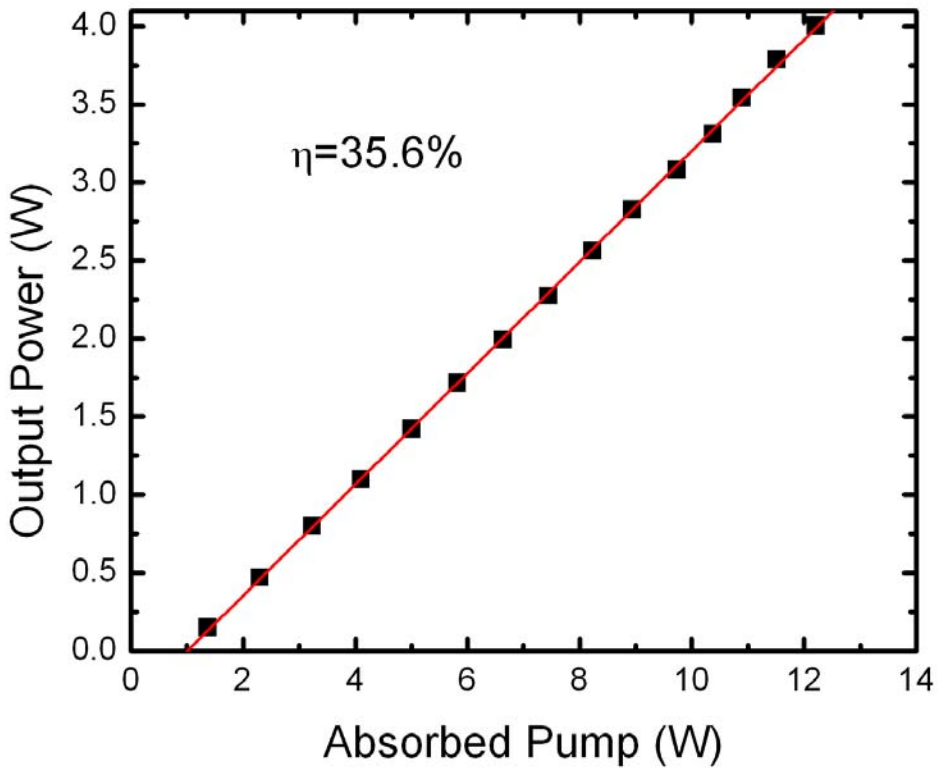

Fig. 4.19 Laser output performance of 40 cm long TM-doped double cladding fiber laser

4.8 Summary:

We report an efficient fiber laser operating near 2 μm. The glass for the fiber is germanate that is highly doped with thulium. The effect of cross relaxation energy transfer between thulium ions are observed from emission spectrum of the glass samples. The fiber laser possesses a very high slope efficiency of 58% with respect to launched power. This corresponds to a quantum efficiency of 1.79, indicating that each pump photon leads to near 1.8 excited Tm^{3+} ions. A thermal tuning method is developed to characterize fiber bragg gratings. Tm-doped germanate fiber with a doping concentration of 5 wt% is fabricated for highly gain short single frequency fiber laser. Single frequency fiber laser has been achieved from a 2 cm long Tm-doped germanate fiber laser. A 4 W laser output is demonstrated from a 40-cm long Tm-doped germenate double cladding fiber laser with a slope efficiency of 35.6%

CHAPTER 5 CONCLUSIONS

This dissertation research work has investigated highly trivalent thulium doped heavy metal oxide glasses system. Both 1.5 μm and 2 μm microsphere lasers are demonstrated in thulium doped tellurite glass microsphere. Higly efficient and single frequency fiber laser are achieved in thulium oxide doped germanate fiber.

Thulium doped tellurite glasses ($0.6TeO_2$-$0.25WO_3$-$0.075K_2O$-$0.075Li_2O$) with different doping concentrations are fabricated. The transition temperature of glass is measured 330 °C by thermo-gravimetric analysis. The refractive index of glass at 1550 nm is 1.978. Fourier Transform Infrared Spectroscopy (FTIR) is utilized to evaluate the maximum phonon energy of Tm-doped tellurite glass. Absorption spectra of thulium are measured under room temperature. Absorption cross-section for ground state transitions of Tm^{3+} in the near infrared and visible region is obtained from absorption spectrum of 5 wt% Tm-doped glass sample. Judd-Ofelt theory is applied to the absorption cross-section spectrum. The Judd-Ofelt intensity parameters are determined through least linear fitting. Compared with other glass samples, Tm-doped tellurite glass possesses a large value of Ω_2, which leads to a big stark split. The radiative decay rates and branch ratios of different transitions have been calculated based on J-O theory. Emission spectra of glass samples in near infrared region (from 1.3 μm to 2.2 μm) have been measured under an excitation of Ti:sapphire laser at 793 nm. The reduction of emission intensity of 1.5-μm transition is observed when the doping concentration is increased. The emission cross-section of the transition ($^3F_4 \rightarrow {}^3H_6$) is evaluated based on Fuchtbauer-ladenburg theory.

The Lifetimes of both $^3H_4$ and $^3F_4$ states of Tm^{3+} are determined by fluorescence decay measurement. The lifetime of $^3H_4$ state drops from 181 μs to 9 μs when the doping concentration is increased from 0.2 wt% to 5 wt%. Non-radiative decay rates of different states are obtained by comparing the radiative and non-radiative lifetimes of them.

A self-calibrating fluorescence spectroscopy technique is used to study the cross-relaxation energy transfer and energy migration between the Tm^{3+} ions doped in the tellurite glass. Ab-initio calculation is used to evaluate the energy transfer process. Fluorescence decay measurement, Judd-Oflet theory, Kushida model, phonon assisted energy transfer model and hopping model are employed to determine the micro and macro-parameters of the energy transfer and energy migration. Steady rate equation analysis is used to simulate intensity ratio of two dominant emission bands. The simulation result of dipole-quadrupole models fits experiment results well. We find that the combination of dipole-quadrupole and dipole-dipole interaction is the dominant mechanism in the energy transfer of thulium ions.

Thulium doped tellurite glass microspheres ranging from 10 μm to 100 μm are fabricated by spin casting technique. A SMF-28 fiber is tapered down to a few micrometers using the typical heat-and-stretch method. The tapered fiber is used to couple the pump light into and signal laser out of the microsphere. Whispering-gallery-modes of microsphere at 2 μm region are observed. Single mode 2-μm laser is demonstrated from tellurite microsphere with 5 wt% doping concentration. Laser wavelength is red shifted from the emission peak of thulium ions at 1800 nm due to the mismatch of pump and laser distributions inside the microsphere.

General laser condition for self-terminating transition is discussed and concluded. 0.5 wt% doping concentration is used to fabricate Tm-doped tellurite glass microsphere for S-band laser. Continuous-wave 1.5-mm microsphere laser from a self-terminating transition (3H4 → 3F4) of thulium is achieved using 793-nm laser pumping through a cooperative lasing process. Cooperative 1.9-μm laser from the lower transition ($^3F_4$->$^3H_6$) of Tm^{3+} is generated to depopulate the lower level ($^3F_4$) of 1.5-μm transition ($^3H_4$->$^3F_4$) in order to achieve the population inversion. Laser wavelength of $^3H_4$->$^3F_4$ transition is shifted by 30 nm from the emission peak. Slope efficiency of 1.9 μm laser is improved after the 1.5 μm transition start to lase. Laser condition of a self-terminating transition has been studied.

Spectroscopic characterizations of thulium doped germanate glass have been examined. The effect of cross relaxation energy transfer between thulium ions is observed from emission spectrum of the glass samples. Continues wave 1.9-mm fiber lasers have been realized in a 4 cm long 4 wt% thulium oxide doped germanate fiber. The slope efficiency of the fiber laser according to launched power is 58% that is higher than the Stokes efficiency. Such high slope efficiency corresponds to a quantum efficiency of 1.79, indicating that each pump photon leads to near 1.79 excited Tm^{3+} ions. Thermal tuning method is developed to characterize fiber bragg gratings, such as linewidth and reflectivity. Single frequency laser operation at 1.9 micron has been successfully accomplished. A fiber based Fabry-Perot interferometer is fabricated and utilized as a scanning filter to examine the single frequency operation. 4 W laser output has been achieved from a 40 cm long Tm-doped germanate double cladding fiber laser.

The research work in this dissertation has shown some exciting results and drawn several important conclusions on thulium oxide doped heavy metal oxide glass. It also reveals several challenges. A more comprehensive theoretical model needs to be developed to include the influences of up conversion and reverse cross relaxation energy transfer. The concentration quenching of $^3F_4$ states needs to be investigated and avoided in the fabrication process. In addition, most of application of 2 μm laser is in the high power region, working under either CW or pulsed condition. Research focuses needs to be shifted onto fabrication of efficient high power Tm-doped fiber laser.

REFERENCES

1.1 Merrian Webster Dictionary

1.2 Heodore H. Maiman " Stimulated optical radiation in ruby " Nature Vol 187 p. 493 (Aug. 6 , 1960)

1.3 L. ESTEROWITZ, "Diode-pumped holmium, thulium, and erbium lasers between 2 and 3 mm operating at room temperature,"OPTICAL ENGINEERING **29**, 676-680 (1990).

1.4 R. C. Stoeman and L. Esterowitz, "Efficient, broadly tunable, laser-pumped Tm:YAG and Tm:YSGG CW lasers,", Optics Letters **15**, 486-488 (1980).

1.5 S.W. Henderson, P.J.M. Suni, C.P. Hale, S.M. Hannon, J.R. Magee, D.L. Bruns, and E.H. Yuen, “Coherent laser radar at 2 μm using solid-state lasers”, IEEE transactions on geoscience and remote sensing **31**, 4-15 (1993).

1.6 K. Miazato, D F De sousa, A Delben, J.R. Delben, S.L de Oliveira, and L.A Nunes, “Upconversion mechanisms in Tm3+ doped lead fluoroindogallate glasses”, Journal of non-crystalline solids **273**, 246-251 (2000).

1.7 R.A. Hayward, W.A. Clarkson, P.W. Turner, J. Nilsson, A.B. Grudinin, D.C. Hanna, “Effiient cladding-pumped Tm-doped silica fibre laser with high power singlemode output at 2 μm”, Electronics Letters, **36** (8),711-712 (2000)

1.8 Johnson LF, Boyd GD, Nassau K, Soden RR “Continous Operation of $CaWO_4$ - Nd+3 Optical Maser” Proceedings of the institute of radio engineers 50 (2): 213& 1962

1.9 Poulain, M., Chanthanasinh, M., and Lucas, J., "New fluoride glasses," Mat. Res. Bull., vol. 12, pp. 151-156, 1977.

1.10 Kassab LRP, Courrol LC, Cacho V.D, TATUMI, S. H. "GeO2-PbO-Bi2O3 glasses doped with Yb3+ for **laser** applications" JOURNAL OF NON-CRYSTALLINE SOLIDS 348: 103-107 NOV 15 2004.

1.11 A.E. Siegman, "Unstable optical resonators fro laser applications" Proc. IEEE 53, 277 (March 1965)

1.12 M. L. Gorodetsky, A. A. Savchenkov, V. S. Ilchenko, Optics Letters, **21**, 453 (1996)

1.13 Hanna, D.C.; Jauncey, I.M.; Percival, R.M.; Perry, I.R.; Smart, R.G.; Suni, P.J.; Townsend, J.E.; Tropper, A.C. "Continuous-wave oscillation of a monomode thulium-doped fibre laser**"** Electronics Letters 24, 19, 1222 – 1223 (1988)

1.14 Percival, R.M.; Szebesta, D.; Davey, S.T.; "Highly efficient and tunable operation of two colour Tm-doped fluoride fibre laser" ELECTRONICS LETTERS 28 (7): 671-673 MAR 26 1992.

1.15 Lincoln, J.R.; Mackechnie, C.J.; Wang, J.; Brocklesby, W.S.; Deol, R.S.; Pearson, A.; Hanna, D.C.; Payne, D.N.; "New class of fibre laser based on lead-germanate glass" ELECTRONICS LETTERS 28 (11): 1021-1022 MAY 21 1992.

1.16 Shubochkin, R.L.; Kozlov, V.A.; Carter, A.L.G.; Morse, T.F.; "Tunable thulium-doped all-fiber laser"; IEEE PHOTONICS TECHNOLOGY LETTERS 10 (7): 944-945 JUL 1998.

1.17 Yamamoto T., Miyajima Y, Komukai T; "1.9-mm Tm-doped silica fiber laser-pumped at 1.57-mm" Eelctronics Letters 30 (3): 220-221 FEB 3 1994.

1.18 PERCIVAL RM, SZEBESTA D, SELTZER CP,; "1.6 MU-M Semiconductor diode-pumped thulium-doped fluoride fiber laser and amplifier of very high-efficiency";ELECTRONICS LETTERS 29 (24): 2110-2112 NOV 25 1993.

1.19 Yamamoto, T. Miyajima, Y. Komukai, T. Sugawa, T.; "1.9-MU-M TM-DOPED FLUORIDE FIBER AMPLIFIER AND LASER-PUMPED AT 1.58-MU-M" ELECTRONICS LETTERS 29 (11): 986-987 MAY 27 1993.

2.0 D.L. Sidebottom, M.A. Hruschka, B.G.B. Potter and R.K. Brow; "Structure and optical properties of rare earth-doped zinc oxyhalide tellurite glasses" *J. Non-Cryst. Solids* **222** (1997), p. 282

2.1 H. Burger, W. Vogel and V. Kozhukharov. "IR transmission and properties of glasses in the TeO_2–R_nO_m, R_nX_m, $R_n(SO_4)_m$, $R_n(PO_3)_m$ *and* B_2O_3] systems"; *Infrared Phys.* **25** (1985), p. 395

2.2 Robert Adair, L. L. Chase, and Stephen A. Payne; "Nonlinear refractive index of optical crystals"; PHYSICAL REVIEW B 39 (5): 3337-3350 FEB 15 1989

2.3 G. Özen, J.-P. Denis, M. Genotelle and F. Pellé. "Tm-Yb-Tm energy transfers and effect of temperature on the fluorescence intensities in oxyfluoride tellurite compounds"; *J. Phys.: Condens. Matter.* **7** (1995), p. 4325.

2.4 M.J. Weber, J.D. Myers and D.H. Bluckburn. "Optical properties of Nd^{3+} in tellurite and phosphotellurite glasses"; *J. Appl. Phys.* **52** 4 (1981), p. 2944.

2.5 J.E. Stanworth. *Nature* **169** (1952), p. 581.

2.6 Jacobs, R.; Weber, M.; "Dependence of the^{4}F3/2→^{4}I11/2induced-emission cross section for Nd^{3+}on glass composition**";** IEEE Journal of Quantum Electronics, 1976,12(2) :102-111.

2.7 JuddB R. "Optical absorption intensities of rare-earth ions," Phys. Rev. 127:750-61 (1962).

2.8 GS Ofelt, ''Intensities of crystal spectra of rare-earth ions,'' J. Chem. Phys. 37, 511 1962 .

2.9 D.C. Yeh, W.A. Sibley and M.J. Suscavage. *J. Appl. Phys.* **63** (1988), p. 4644

2.10 G.Poirier, F.C.Cassanjes, C.B.de Araujo, V.A.Jerez, S.J.L.Ribero, Y.Messaddeq and M.Poulain. *J. Appl. Phys.* **93** (2003), p. 3259.

2.11 G.Poirier, V.A. Jerez, C.B. de Araujo, Y. Messaddeq, S.J.L. Ribeiro and M. Poulain. *J. Appl. Phys.* **93** (2003), p. 1493.

2.12 C.B. Layne, W.H. Lowdermilk, and M.J. Weber, "Multiphonon relaxation of rare-earth ions in oxide glasses", Physical Review B **16**, 10-20 (1977).

2.13 D.L. Dexter, "A Theory of Sensitized Luminescence in Solids", Journal of chemical physics **21**, 836-850 (1953).

2.14 Forster T. "Zwischenmolckulare energiewanderung und fluoreszenz (Intermolccular energytransfer and fluorescence)". *Annalen der Physik* 2:55-77, 1948.

2.15 A.M. Tkachuk, I.K. Razumova, M.F. Joubert, R. Moncorge, D.I. Mironov, and A.A. Nikitichev, "Self-quenching of luminescence in YLF : Tm3+ crystals: I. Microscopic parameters and rates of energy transfer", Solid-state spectroscopy **85**, 885-892 (1998).

2.16 D.F. de Sousa, R. Lebullenger, A.C. Hernandes, and L.A.O. Nunes, "Evidence of higher-order mechanisms than dipole-dipole interaction in $Tm^{3+} \rightarrow Tm^{3+}$ energy transfer in fluoroindogallate glasses", Physical Review B **65**, 094204 (2002).

2.17 L. Gomes, L.C. Courrol, L.V.G. Tarelho, and I.M. Ranieri, "Cross-relaxation process between +3 rare-earth ions in $LiYF_4$ crystals", Physical review B **54**, 3825-3829 (1996).

2.18 I.R. Martin, V.D. Rodriguez, U.R. Rodriguez-Mendoza, V. Lavin, E. Montoya, and D. Jaque, "Energy transfer with migration. Generalization of the Yokota - Tanimoto model for any kind of multipole interaction", Journal of Chemical Physics **111**, 1191-1194 (1999).

2.19 T. Kushida, "Energy Transfer and Cooperative Optical Transitions in Rare-Earth Doped Inorganic Materials. I. Transition Probability Calculation", Journal of the physical society of Japan **34**, 1318-1326 (1973).

2.20 Mario Yokota and Osamu Tanimoto, "Effects of Diffusion on Energy Transfer by Resonance", Journal of the physical society of Japan **22**, 779-784 (1967).

2.21 A.I. Burshtein, Soviet physics, "A hopping mechanism of energy transfer", JETP **35**, 882-886 (1972).

2.22 Toru Miyakawa and D.L. Dexter, “Phonon Sidebands, Multiphonon Relaxation of Excited States, and Phonon-Assisted Energy Transfer between Ions in Solids”, Physical Review B **1**, 2961-2969 (1970).

3.1 F.Vollmer, D.Braun, A.Libchaber, M.Khoshima, I.Teraoka, and S.Arnold, Applied Physics Letter **80,** 4057 (2002)

3.2 H.J.Kimble PHYSICA SCRIPTA **T76**: 127-137 1998

3.3 X.Peng, F.Song, S.Jiang, N.Peyghambarian, M.Kuwata-Gonokami, and L.Xu, Applied Physics Letter **82**, 1497 (2003)

3.4 S.-X. Qian and R.K.Chang, Physical Review Letters **56**, 926 (1986).

3.5 J. Campillo, J. D. Eversole, and H. B. Lin, "Cavity Quantum Electrodynamic Enhancement of Stimulated-Emission in Microdroplets," Phys. Rev. Lett. 67 (4), 437-440 (1991).

3.6 Y.Z. Wang, B.L. Lu, **Y.Q. Li**, and Y.S. Liu, "Observation of cavity quantum-electrodynamic effects in a Nd:glass microsphere", *Optics Letters*, 20, 770-772 (1995).

3.7 A.F.J.Levi,R. E. Slusher, S. L. McCall, T. Tanbun-Ek, D. L. Coblentz and S. J. Pearton, “Room temperature operation of microdisc lasers with submilliamp threshold current”; Electron. Lett. 28, 1010-1012 (1992).

3.8 S. V. Frolov, M. Shkunov, and Z. V. Vardeny, K. Yoshino, “Ring microlasers from conducting polymers”; Phys. Rev. B 56, R4363–R4366 (1997).

3.9 A. W. Poon, F. Courvoisier and R. K. Chang, "Multimode resonances in square-shaped optical microcavities," Opt. Lett. **26**, 632-634 (2001).

3.10 M.L. Gorodetsky, A. A. Savchenkov, V. S. Ilchenko, Optics Letters, **21**, 453 (1996).

3.11 V.B.Braginsky, M.L.Gorodetsky and V.S.Ilchenko, Physics letters A **137**, 393 (1989).

3.12 M.Cai and K.Vahala, Optics Letters, **25**, 260 (2000).

3.13 N.Dubreuil, J.C.Knight, D.Leventhal, V.Sandoghdar, J.Hare, and V.Lefevre, Optics Letters **20**, 813 (1995).

3.14 H.M. Nussenzveig, *Diffraction effects in semi-classical scattering*, Cambridge University Press, 1992.

3.15 A.Yariv, IEEE Journal of quantum electronics 9 (1973) 919.

3.16 F.Lissillour, D.Messager, G.Stephan, and P.Feron, Optics Letters, **26**, 1051 (2001).

3.17 L.Yang and K.J.Vahala Optics Letters, **28**, 592 (2003).

3.18 R.C. Stoneman and L. Esterowitz, Optics Letters, **16**, 232 (1991)

3.19 G.H. Rosenblatt, R.C. Stoneman , and L. Esterowitz, Advanced Solid state Lasers, 1990 Tech. Dig. Ser. Wash., DC: OSA, 1990

3.20 S. Tanabe, X. Feng, and T. Hanada, Optics Letters **25**, 817 (2000).

3.21 T. Kasamatsu, Y. Yano, and T. Ono, IEEE Photon. Technol. Lett. **13**, 31 (2001).

3.22 Jianfeng Wu, Shibin Jiang, Tiequn Qiu, and Nasser Peyghambarian, “Cross relaxation energy transfer in thulium doped tellurite glass,” Submitted to JOSA B

3.23 R.S. Quimby and W.J. Miniscalso, Applied Optics, **28**, 14, (1989).

3.24 R. Allen, L. Esterowitz, and I. Aggarwal, IEEE journal of quantum electronics, **29**, 303, (1993)

3.25 R.M. Percival, D. Szebesta, and S.T. Davey, Electronics Letters **28**, 1866 (1992).

4.1 Jihong Geng, Christine Spiegelberg, and Shibin Jiang; “Narrow Linewidth Fiber Laser for 100-km Optical Frequency Domain Reflectometry”; IEEE PHOTONICS TECHNOLOGY LETTERS, VOL. 17, NO. 9, SEPTEMBER 2005.

4.2 Jeff Hecht; “PHOTONIC FRONTIERS: HIGH-POWER FIBER LASERS: Pumping up the power”; *Laser Focus World* August, 2005

4.3 Poulain, M., Chanthanasinh, M., and Lucas, J., "New fluoride glasses," Mat. Res. Bull.,vol. 12, pp. 151-156, 1977.

4.4 S. Shibata, M. Horiguchi, K. Jinguji, S. Mitachi and T. Manabe: Electron. Lett. **17** (1981) 775.

4.5 Kobayashi, S., Shibata, N., Shibata, S., and Izawa, T., "Characteristics of optical fibers in infrared wavelength region," Rev. Electrical Comm. Lab, vol. 26, pp. 453-467, 1978.

4.6 M.J.F.Digonnet, “Rare-Earth-Doped Fiber Lasers and Amplifiers”, P: 118-120

4.7 D. Gloge, “Weakly guiding fibers”, Applied Optics **10** (1971), 2252

4.8 R.A. Hayward, W.A. Clarkson, P.W. Turner, J. Nilsson, A.B., Grudinin, D.C. Hanna, “Effiient cladding-pumped Tm-doped silicafibre laser with high power singlemode output at 2μm”, Electronics Letters, **36** (8),711-712 (2000).

4.9 Andreas Othonos, Kyriacos Kalli , " Fiber Bragggg Gratings - Fundamentals and Applications in Telecommunications and Sensing " , 2001.